National Library of Canada
Acquisitions and Bibliographic Services Branch
395 Wellington Street
Ottawa, Ontario
K1A 0N4

Bibliothèque nationale du Canada
Direction des acquisitions et des services bibliographiques
395, rue Wellington
Ottawa (Ontario)
K1A 0N4

Your file Votre référence

Our file Notre référence

NOTICE

The quality of this microform is heavily dependent upon the quality of the original thesis submitted for microfilming. Every effort has been made to ensure the highest quality of reproduction possible.

If pages are missing, contact the university which granted the degree.

Some pages may have indistinct print especially if the original pages were typed with a poor typewriter ribbon or if the university sent us an inferior photocopy.

Reproduction in full or in part of this microform is governed by the Canadian Copyright Act, R.S.C. 1970, c. C-30, and subsequent amendments.

AVIS

La qualité de cette microforme dépend grandement de la qualité de la thèse soumise au microfilmage. Nous avons tout fait pour assurer une qualité supérieure de reproduction.

S'il manque des pages, veuillez communiquer avec l'université qui a conféré le grade.

La qualité d'impression de certaines pages peut laisser à désirer, surtout si les pages originales ont été dactylographiées à l'aide d'un ruban usé ou si l'université nous a fait parvenir une photocopie de qualité inférieure.

La reproduction, même partielle, de cette microforme est soumise à la Loi canadienne sur le droit d'auteur, SRC 1970, c. C-30, et ses amendements subséquents.

Canada

COMPUTER MODELING OF INTERGRANULAR FRACTURE IN TEXTURED MATERIALS

BY

Jian Lu

A thesis submitted to the Faculty of Graduate Studies and Research
in partial fulfilment of the requirements for the degree of
Doctor of Philosophy

Department of Mining and Metallurgical Engineering
McGill University, Montreal
December 1995

© Jian Lu

National Library
of Canada

Acquisitions and
Bibliographic Services Branch

395 Wellington Street
Ottawa, Ontario
K1A 0N4

Bibliothèque nationale
du Canada

Direction des acquisitions et
des services bibliographiques

395, rue Wellington
Ottawa (Ontario)
K1A 0N4

Your file Votre référence

Our file Notre référence

The author has granted an irrevocable non-exclusive licence allowing the National Library of Canada to reproduce, loan, distribute or sell copies of his/her thesis by any means and in any form or format, making this thesis available to interested persons.

L'auteur a accordé une licence irrévocable et non exclusive permettant à la Bibliothèque nationale du Canada de reproduire, prêter, distribuer ou vendre des copies de sa thèse de quelque manière et sous quelque forme que ce soit pour mettre des exemplaires de cette thèse à la disposition des personnes intéressées.

The author retains ownership of the copyright in his/her thesis. Neither the thesis nor substantial extracts from it may be printed or otherwise reproduced without his/her permission.

L'auteur conserve la propriété du droit d'auteur qui protège sa thèse. Ni la thèse ni des extraits substantiels de celle-ci ne doivent être imprimés ou autrement reproduits sans son autorisation.

ISBN 0-612-12421-5

Canada

ABSTRACT

An integrated computer simulation employing the Embedded-atom method (EAM), Molecular dynamics (MD), and Markov Chain Fracture models has been constructed and applied to study the intergranular fracture of brittle polycrystalline materials at both the atomistic and microscopic levels. At the atomistic level, the computer model is capable of treating bicrystals under the influence of external load and temperature with dynamic periodic boundary conditions along the grain boundary plane and a dynamic boundary condition perpendicular to the grain boundary plane. At the microscopic level, the computer model is capable of treating the sample with microstructure defined by the grain boundary character distribution under the influence of an external load to predict the intergranular fracture propagation under stress.

The fracture behavior of many Σ grain boundaries has been investigated at the atomistic level for Cu, Ni, and Ni_3Al, and the fracture resistance of the grain boundary was predicted. It has been found that grain boundary energy and fracture resistance greatly depend on the grain boundary structure. Symmetrical Σ3 twin boundaries and low angle Σ1 boundaries are particularly strong in resisting intergranular fracture, while some other low Σ boundaries are also strong, but grain boundaries with high energies are not at all fracture resistant. The calculated correlation between fracture resistance and misorientation of grain boundaries is in accordance with the experimental data. The calculated fracture resistances of the grain boundaries for Ni_3Al alloy are not significantly different from those for pure Ni. This suggests that the tendency to intergranular fracture is not due merely to the poor fracture resistance of grain boundaries. One must also consider the overall grain boundary character distribution.

In order to find the role of grain boundary character distribution on the intergranular fracture in brittle polycrystalline materials, the crack path, crack arrest distance, and fracture toughness have been investigated at the microscopic level with the different fraction of low-energy grain boundaries, grain boundary fracture resistance, orientation distribution of grain boundary planes, and grain shape factor. The simulations have indicated that with an increase in the fraction of low energy grain boundaries, the fracture toughness increases while the crack arrest distance decreases. With an increase in the number of low energy grain boundaries which are aligned parallel to the stress axis, one observes an increase in the fracture toughness and a decrease in the crack arrest distance. By increasing the grain shape factor, the fracture toughness decreases while the crack arrest distance increases.

If five grain diameter is defined as the critical length, and more than 25% of grain boundaries are of low-energy with the highest fracture resistance, such as $\Sigma 3$ twin grain boundaries, the intergranular crack formed initially cannot propagate further due to the presence of fewer random boundaries, and the polycrystalline materials will show high ductility. The improvement in fracture toughness of Ni_3Al brittle polycrystal is due to the introduction of a high frequency of low energy grain boundaries (up to 70% by experimental treatments). Grain boundary design and control achieved by manipulating the grain boundary character distribution (GBCD) are important to fracture toughness improvement of the brittle polycrystal materials.

RÉSUMÉ

Une modélisation par ordinateur utilisant la méthode des atomes entourés (Embedded-atom method EAM), et les modèles de dynamiques des molécules (MD) et de rupture des chaines de Markov a été élaborée. Ce modèle a été appliqué à l'étude de la rupture intergranulaire des matériaux fragiles polycristallins tant au niveau atomique que microscopique. Au niveau atomique, le modèle permet d'étudier les bicristaux soumis à une charge externe et à la température avec des limites dynamiques périodiques le long du plan du joint de grains et une limite dynamique perpendiculairement au plan du joint de grains. Au niveau microscopique, le modèle peut traiter le cas d'un échantillon, dont la microstructure est définie par la distribution de structure des joints de grains, soumis à un chargement externe. Ceci permet de prévoir la propagation de la rupture intergranulaire sous contrainte.

Le comportement à la rupture de nombreux joints de grains Σ a été étudié au niveau atomique pour le Cu, Ni, et Ni_3Al. La résistance à la rupture des joints de grains a alors été prédite. Il a été montré que l'énergie des joint de grains ainsi que la résistance à la rupture dépendent fortement de la structure des joints de grains. Les joints de maclage symétriques Σ3 et les joints de faibles désorientations Σ1 résistent particulièrement bien à la rupture. Certains autres joints-Σ de faibles désorientations sont aussi solides. Mais les joints de grains de haute énergie ne sont pas du tout résistants. Les corrélations calculées entre la résisatnce à la rupture et la désorientation des joints de grains sont en accord avec les résultats expérimentaux. Les résistances à la rupture calculées pour l'alliage Ni_3Al ne sont pas significativement différentes de celles du Ni pur. Cela suggère que la tendance à la rupture intergranulaire n'est pas due

principalement à la mauvaise résistance à la rupture des joints de grains. Il faut aussi prendre en compte la distribution globale de la structure des joints de grains.

Afin d'en déterminer le rôle sur la rupture intergranulaire des matériaux polycristallins, le chemin de fissure, sa distance d'arrêt, et la ténacité ont été étudiés au niveau microscopique en fonction de différentes fractions de joints de grains de faible énergie, de la résistance à la rupture des joints de grains, de la distribution des orientations du plan des joints de grains, et du facteur de forme des grains. La modélisation indique qu'une augmentation de la fraction de joints de grains de faible énergie entraine une augmentation de la ténacité alors que la distance d'arrêt de la fissure diminue. D'autre part, une augmentation du nombre de joints de grains de faible énergie alignés parallèlement à l'axe des contraintes entraine aussi une augmentation de la ténacité et une diminution de la distance d'arrêt de la fissure. En revanche, l'augmentation du facteur de forme du grain entraine une diminution de la ténacité et une augmentation de la distance d'arrêt de la fissure.

Si 5 fois le diamètre du grain est défini comme longueur critique, et si plus de 25 % des joints de grains sont de faible énergie avec la plus haute résistance à la rupture, tels que des joints de maclages $\Sigma 3$, les fissures intergranulaires formées initialement ne peuvent se propager du fait de la présence de quelques joints de grains distribués aléatoirement.. Le polycristal a alors une ductilité plus élevée. L'amélioration de la ténacité du polycristal fragile Ni_3Al est due à l'introduction d'une fraction élevée de joints de grains de faible énergie (jusqu'à 70% par traitements expérimentaux). L'architecture des joints de grains ainsi que son controle obtenu en modifiant la distribution de la structure des joints de grain sont importants pour améliorer la ténacité des matériaux polycristallins fragiles.

ACKNOWLEDGEMENTS

The author wishes to express his sincere gratitude to professor J.A. Szpunar for his detailed supervision, academic guidance and instruction for the entire duration of the thesis research work, and also for his constant encouragement, support and friendship.

The author is grateful to Mr. P. Blandford, Mr. D. Hinz, Mr. D.Y. Li, Mr. S. Poplawski, Mr. K. Lee, H. Park, and Dr. F. Czerwinski for their technical support, scientific discussion, and help.

The author would like to acknowledge CRAY Research Inc., Dr. N. Chepurinity and Dr. M. Head who helped us in accessing and using CRAY supercomputers.

The author also wishes to express his thanks to the Hydro-Quebec, and the Natural Science and Engineering Research Council of Canada for financial support.

TABLE OF CONTENTS

LIST OF FIGURES

LIST OF TABLES

CHAPTER 1:
INTRODUCTION

Modern materials science and engineering based on structure-property-performance relationship has developed a number of high performance materials. However, there has been a long-standing problem that as material becomes stronger it becomes more brittle due to the occurrence of intergranular fracture [Watanabe 1989, Puge 1991]. This has been the main weakness of many advanced, high performance structural materials, such as engineering ceramics and intermetallic compounds, as well as structural metals and alloys embrittled by impurities and by the presence of a corrosive environment [Seah, 1980, Koch et al. 1984, Briant 1985, Stoloff et al. 1986]. It is well known that material fracture can greatly affect the function of human society in a beneficial or detrimental way, depending on whether the fracture occurs in controlled or uncontrolled circumstances. When fracture occurs in uncontrolled circumstances often unexpectedly, it brings about serious damage, even catastrophe, to human society. Here for examples in aircraft accidents caused by metal fatigue and nuclear power station accidents caused by stress corrosion cracking. Therefore, the control of fracture is clearly the ultimate goal of fracture research. Based on that premise and other important factors, Watanabe [1984] introduced the concept of "grain boundary design and control" about ten years ago. This is the main potential for the control of structure-dependent intergranular fracture and related brittleness of the polycrystalline materials on the basis of the grain boundary design, through the control of grain boundary character distribution (GBCD) [Watanabe 1988].

Grain boundaries are known to be important microstructural components which strongly affect the properties of polycrystalline materials. An early theory of Hargreaves and Hills [1929] was that different structures may exist for different boundaries in metal. Later, Aust and

Chalmers [1952] showed that these structural differences can lead to different grain boundary properties, such as their energies. Kronberg and Wilson [1949] introduced an important concept - coincident site lattice (CSL). Experimental studies have shown that "special" grain boundaries, described in the CSL model as being close to low Σ orientation relationships, display improved physical, chemical and mechanical properties relative to general or high Σ grain boundaries [Schvindlerman and Straumal 1985, Palumbo and Aust 1992]. These improved properties include, among others, lower energy in pure metals, lower intrinsic electrical resistivity, and greater resistance to intergranular fracture. Since many of these low Σ grain boundaries have beneficial properties, the objective of the "grain boundary design and control" was to improve the bulk properties of polycrystalline materials by increasing the number of low Σ grain boundaries through the control of GBCD [Watanabe 1984, Aust 1993]. One of the earliest studies to indicate that the fraction of low Σ grain boundaries could be controlled was conducted by Aust and Rutter [1959]. It was found that specific solute additions could increase the frequency of Σ boundaries in zone refined lead. Since then, numerous structural and processing parameters, such as twin boundaries, grain size, crystallographic texture, precipitates, prestrain and annealing, have been shown to influence the fraction of low Σ boundaries in polycrystalline materials [Watanabe 1985, 1986, Aust 1993, Aust and Palumbo 1991, Lin and Pope 1993].

Since the grain boundaries are the important sites where fracture in polycrystals is observed, intrinsic or extrinsic brittleness of polycrystalline materials are mainly due to intergranular fracture. There is a general tendency that an increase in the strength renders a polycrystal less ductile by invoking intergranular fracture. When the stress concentration generated at the grain boundary exceeds the grain boundary cohesion, the intergranular fracture occurs. The grain boundary cohesion depends on the type and structure of the grain boundary and it can be characterized by grain boundary energy. Experimental work [Kurishita and Yoshinaga 1989] on the effect of grain boundary type and misorientation on intergranular fracture stress has been performed in molybdenum bicrystals with symmetric <110> tilt and <110> twist boundaries. The results showed that the fracture stress for high purity molybdenum bicrystals is high at the misorientation angle smaller than 10° and that corresponds to $\Sigma 3$ coincidence orientation, which is much lower than that for low purity bicrystals at a misorientation angle between 20° to 50°. The twist bicrystals showed a more significant misorientation effect on the fracture stress, but little effect on material purity was observed. It is easy to see that the fracture stress of bicrystal strongly depends on the type and structure of the grain boundary, and that it can also be affected by material purity through the effect of grain boundary segregation. This could be one of the sources of the extrinsic intergranular fracture often observed. Another important conclusion is that low energy boundaries such as low angle and low Σ grain boundaries are not good sites for segregation and therefore they are insensitive to material purity irrespective of the type of grain boundary [Watanabe 1993A]. These experimental data are vital to the "grain boundary control and design." Unfortunately, there are very few experimental data available, and these kinds of bicrystal experiments are very difficult to be done for most metals and alloys.

Intergranular brittleness is the primary problem in developing ordered intermetallic alloys. Ni_3Al is a typical and extensively studied ordered alloy [Stoloff 1989]. However, the problem of intergranular brittleness persists [Watanabe 1993A]. Quite recently, Hirano has brought about a breakthrough in this difficult area [Hirano 1990, 1991, Hirano and Mawari 1992, 1993]. He has found that unidirectional solidification by zone-melting can drastically improve the ductility of polycrystalline Ni_3Al without boron, obtaining more than 50% elongation at room temperature. It is surprising that so-called inherently brittle materials Ni_3Al could be made ductile without the addition of boron or another element. It has been found that the observed improvement in ductility of undoped Ni_3Al polycrystal is due to the introduction of a high frequency of low angle boundaries and low Σ (3, 9) grain boundaries [Watanabe 1993A]. In addition, it has been found that material processes, such as annealing and/or strain annealing, can also improve the fracture toughness of polycrystalline Ni_3Al without boron [Lin and Pope 1993, Chiba et al. 1994]. The distribution of grain boundary types along intergranular cracks in the Ni_3Al alloy was measured by Lin and Pope [1993]. It was found that more than 89% of cracked grain boundaries along crack paths are high Σ, high angle grain boundaries compared to 58.6% in the general population, and only less than 2% and 3% of cracked grain boundaries are low angle $\Sigma 1$ and symmetrical $\Sigma 3$ (twin) boundaries compared to 7.5% and 28.2% in the general population, respectively. The results indicated that the low angle ($\Sigma 1$) and symmetrical $\Sigma 3$ (twin) boundaries are particularly strong; the low Σ, high angle boundaries, as a group, are not so strong; and that the high Σ, high angle boundaries are very weak. Chiba et al. [1994] have found that the percentages of CSL boundaries in cast, recrystallized and strain annealed Ni_3Al alloys are 26.8, 43.1 and 58.4%, respectively, of the total number of boundaries examined. The strain annealed Ni_3Al alloy exhibits elongation of approximately 50%, indicating that the fracture toughness of Ni_3Al can be improved by enhancing the frequency of occurrence of CSL boundaries, especially low angle $\Sigma 1$ and/or $\Sigma 3$ twin boundaries. Therefore, the Ni_3Al alloy prone to intergranular cracking could be toughened by increasing the abundance of those "special grain boundaries."

The fracture processes and characteristics of polycrystalline materials may be studied at three different levels of length scale [Watanabe 1993A]: macroscopic, microscopic and atomistic in both experimental and theoretical investigations. At the macroscopic level, the fracture processes can be easily conducted by both experimental tests and computer simulations (for example, the finite element method). At the microscopic level, the fracture processes are not very easily carried out by experimental tests. Recent experimental advance, the Orientation Image Microscopy introduced by Adams, Wright and Kunze [1993], made it possible to determine the crystallographic characteristics of a larger number of grain boundaries in a short time. It also made it possible to study the intergranular fracture in experimental tests. However, there is still no very good microscopic model to understand the intergranular fracture due to the lack of characteristic data for most grain boundaries. At the atomistic level, as we discussed earlier, experimental difficulties have resulted in very few bicrystal experiments to study the intergranular fracture. These formidable difficulties in the experimental study of structure-property correlations, simply because of the complexity of the phenomenon and the large number of parameters and variables involved. Such problems are possible at every stage of an experiment, from sample preparation where one needs to control the interfacial structure, to sample characterization, and to the measurement of details of the fracture process. These experimental difficulties, in contrast, also serve to emphasize the considerable opportunities one has with the approach of atomistic modeling and simulations. It is precisely the inherent nature of atomistic calculations that makes it possible to specify the interatomic structure and forces, to determine the atomic configuration at any stage of the system relaxation and temporal evolution, and to follow the molecular details of dynamical processes. Therefore, the intergranular fracture of the bicrystal could be easily approached by molecular dynamics (MD) simulation [Yip and Wolf 1989]. It is evident that grain boundaries can bridge these three levels' aspects of fracture processes in polycrystalline materials.

In this investigation, the techniques of molecular dynamics (MD), along with the embedded atom method (EAM) developed by Daw and Baskes [1983, 1984], are used to study the fundamental mechanisms of intergranular fracture for many special grain boundaries in Cu, Ni and Ni_3Al systems. The atomistic results are then applied to our microscopic model to study crack path, crack arrest distance and fracture toughness influence by the fraction of low energy grain boundaries, grain boundary fracture resistance, orientation distribution of grain boundary planes, and grain shape factor. Specific attention is focussed on an integrated approach to the intergranular fracture at both the atomistic and microscopic levels. The goal of this work is to develop an integrated model for intergranular fracture at both the atomistic and microscopic levels which can be used to analyze a role of grain boundary character distribution (GBCD), texture, and microstructure in fracture resistance of polycrystalline materials in order to improve the fracture toughness of brittle polycrystalline materials through optimization and control of the grain boundary structure.

This thesis is organized into the following chapters. Chapter II presents information on a background of grain boundary and intergranular fracture, and a review of the interatomic potentials, boundary conditions, and simulation methods, microscopic models which have been applied to study related problems. Chapter III describes the EAM potential, the atomistic grain boundary model used in molecular dynamics simulation, the microscopic model used in Markov chain intergranular fracture simulation, and presents an the integrated approach of intergranular fracture in polycrystalline materials. Chapter IV shows the verification of embedded-atom method and grain boundary model. Two examples are presented and compared with experimental data: one is the liquid, glass formation and crystallization of glass for transition metal Ni, while the other is the melting of a twist $\Sigma 5$ grain boundary in Al. Chapter V presents the applications of computer simulation methods to the intergranular fracture. The results and discussion of this investigation include grain boundary structure and energy, MD simulation of grain boundary fracture, comparison of predictions with bicrystal experiments, crack path, crack arrest distance and fracture toughness of the polycrystalline materials, and integrated approach to intergranular fracture. Chapter VI presents conclusions and recommendations for future research. Finally, an appendix contains a detailed derivation of the embedded atom method (EAM).

CHAPTER 2:
REVIEW

The goal of this project is to investigate intergranular fracture at both the atomistic and microscopic levels. Specific attention is focussed on the role of the special Σ grain boundary character distribution on the intergranular fracture in Ni_3Al alloy. The primary methods employed in the investigation are molecular dynamics simulation using the embedded atom method for the interatomic potentials at the atomistic level, and Markov chain statistical model with Monte Carlo simulation for the microstructure generation at the microscopic level. The purpose of this chapter is to provide background information on the problems about grain boundary and intergranular fracture and to review the various simulation methodologies that have been applied to similar problems.

2.1. Grain Boundary and Fracture

2.1.1. Intergranular Fracture

On the macroscopic scale, the main kinds of fracture in polycrystalline materials are due to either elastic, microvoid coalescence, environmental, fatigue, or creep [Puge 1991]. All these fractures can follow grain boundary paths - intergranular fracture.

On the microscopic scale, the fracture processes in polycrystalline materials are the result of either transgranular or intergranular fractures, or a combination of these processes [Watanabe 1989]. The mode of fracture can be strongly affected by materials composition, microstructure and environment. When the fracture mode is predominantly intergranular, a polycrystal shows brittle fracture behavior.

On the atomistic scale, crack growth occurs by either (i) tensile separation of atom ('decohension'), (ii) shear movement of atoms (dislocation egress of injection), (iii) removal of atoms by dissolution or diffusion, or (iv) combinations of these processes, at crack tips [Lynch 1989]. All of these processes can occur preferentially at grain boundaries, thereby producing intergranular fracture. The preferential occurrence of these processes at grain boundaries is associated with a variety of phenomena, such as (i) segregation of 'embrittling' elements to grain boundaries, (ii) more rapid nucleation and growth of precipitates at grain boundaries than in grain interiors, and (iv) greater adsorption of environmental species at grain boundary/surface intersections than at other surface sites. These phenomena occur, of course, because atoms at grain boundaries have a slightly lower packing density than atoms at grain interiors.

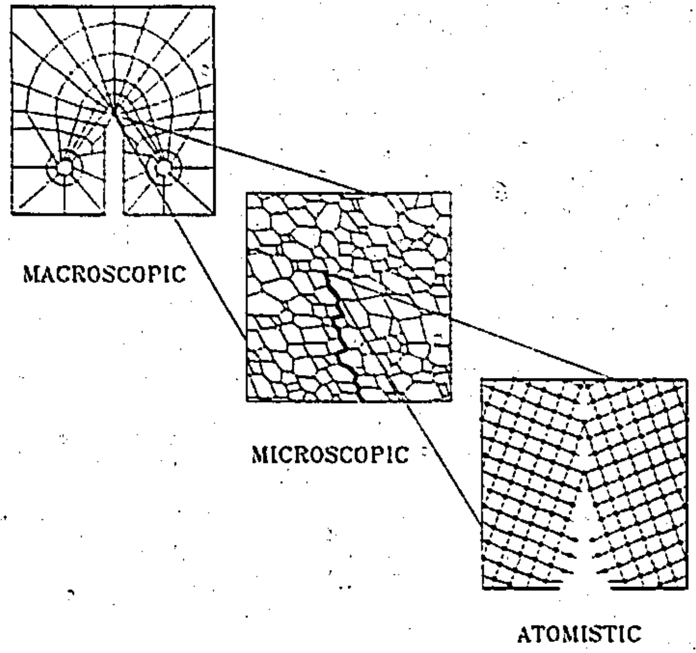

Figure 2.1 Three different scales in studies of fracture in a polycrystal at the macroscopic, microscopic, and atomistic levels.

Accordingly, it may be shown that the fracture of polycrystalline materials can be studied at three different levels of length scale [Watanabe 1993A]: macroscopic, microscopic and atomistic, as indicated schematically in Figure 2.1. It is evident that grain boundaries can bridge these three aspects of the fracture process. From the view of materials science and engineering, the last two aspects are very important to us. Therefore, specific attention is focussed here on the microscopic and atomistic scales of the intergranular fracture.

2.1.2. Grain Boundary Character and Structure

The grain boundaries in real polycrystalline materials are not of the same type or structure. Strictly speaking, each grain boundary has its own character and structure. However, in the interest of simplicity, the grain boundaries can be classified into several groups depending on the grain boundary misorientation. Normally they can be classified into three groups [Watanabe 1989]: (i) low-angle boundaries with a misorientation angle smaller than 15°, (ii) high-angle coincidence boundaries which are defined by Σ values associated with a special misorientation angle about specific rotation axis, and (iii) high-angle general so-called random boundaries, which have no boundary misorientation close to any low Σ coincidence orientation. Furthermore, the first two groups are regarded as low-energy boundaries, and the third as high-energy boundaries.

Figure 2.2 presents the coincidence site lattice (CSL) geometry for a $\Sigma 5$ twist boundary formed by a 36.87° [100] misorientation of two adjoining lattices [Aust 1993]. The CSL is considered the smallest common sublattice of the adjoining grains [Grimmer et al. 1974]. The volume ratio of the unit cell of the CSL to that of the crystal is described by the parameter Σ, which can also be considered the reciprocal density of coincident sites [Kronberg and Wilson 1949]. All grain boundaries can be represented by an appropriate CSL description if Σ is allowed to approach infinite values [Warrington 1979].

With low angle boundaries ($\Sigma=1$), the CSL is coincident with the adjoining crystal lattices, and the grain boundaries can be described through lattice or primary dislocations which accommodate the deviations from ideal crystal coincidence, i.e., the single crystal [Read and Shockley 1950].

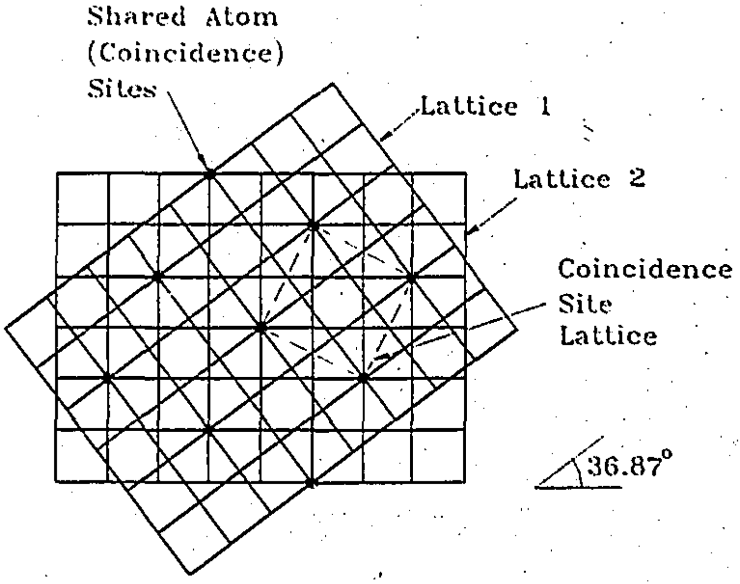

Figure 2.2 Schematic representation of the coincidence site lattice geometry for a Σ5 twist boundary formed by a 36.87° [100] misorientation of two adjoining lattices.

Until recently, there was no standard experimental technique for the determination of grain boundary types and their distribution in real polycrystalline materials. The modern scanning electron microscopy-electron channeling pattern (SEM-ECP) technique has enabled us to do the characterization of a larger number of grain boundaries in polycrystal, which in the past was laborious and time-consuming. Recently Adams et al. [1993] introduced a new method of Orientation Imaging Microscopy (OIM) that makes use of rapid, direct measurements of local lattice orientation on a grid of points to form micrographs of the polycrystalline microstructure. OIM also enables the measurement and characterization of grain boundary texture and grain boundary distributions.

Experimental studies over the past 40 years have shown that "special" grain boundaries, described in the CSL model as being close to low Σ orientation relationships, display improved physical, chemical and mechanical properties relative to general or high Σ boundaries [Aust and Palumbo 1991]. The applicability of the Σ criterion to grain boundary properties is largely due to the importance of Σ and $\Delta\theta$ in defining interfacial dislocation structures through the relaxation associated with the CSL model. The boundary plane is generally found to be significant when the grain boundary is already in a low CSL orientation. Low Σ grain boundaries, i.e., $\Sigma \leq 29$ and $\Delta\theta = 15^\circ \Sigma^{-5/6}$, have the following properties as compared to high Σ and random boundaries [Aust and Palumbo 1991, Aust 1993]:

- lower energy in pure metals;
- less susceptible to impurity or solute segregation;
- greater mobility with specific type and concentration of solutes;
- smaller diffusivity;
- lower intrinsic electrical resistivity;
- greater resistance to grain boundary sliding; and,
- greater resistance to intergranular degradation phenomena such as fracture, cavitation and localized corrosion.

Since many of these "special" or low Σ grain boundaries have beneficial properties, the concept of "grain boundary design and control" was introduced by Watanabe [1984]. The objective was to improve the bulk properties of polycrystalline metals by increasing the number of "special" grain boundaries in the grain boundary character distribution.

2.1.3. Grain Boundary Design and Control

There are several possible ways by which grain boundaries can be designed and controlled to confer desirable properties to a polycrystalline material. Possible microstructural parameters for grain boundary engineering are as follows [Watanabe 1993B]: (i) geometrical parameters: grain size, grain shape, boundary junctions, etc; (ii) morphological parameters: boundary inclination, boundary phase, and boundary width; (iii) structural parameters: boundary type, boundary character, and boundary structure; (iv) composition parameters: boundary segregation and boundary precipitation; and (v) energetic parameters: boundary energy, boundary electronic charge, and boundary magnetic state.

Table 2.1 Grain boundary control applicable to grain boundary design [Watanabe 1993B].

Type of Boundary	**Controlling Parameter**	**Application**
Grain boundary density	grain size, boundary volume	increase in strength and ductility, new properties
grain boundary geometry	boundary inclination, dihedral angle	increase in creep ductility and superconductivity
grain boundary morphology	precipitate, size and density	increase in corrosion resistance, ductility
grain boundary chemistry	segregation level, PFZ width	suppression of embrittlement, high corrosion resistance
grain boundary character and structure	boundary type, GBCD	increase in strength and ductility.

It is evident that there is a great variety of ways of designing and controlling the grain boundaries, when we take into account the importance of boundary type and structure in addition to geometrical or topological configurations. The combination of structural effects and geometrical effects tremendously increases the variety and flexibility of designing grain boundaries in polycrystalline materials. Unfortunately, until recently, this was almost ignored in materials design and development. Table 2.1 give various types of boundary control, controlling parameters, and applications for the improvement or enhancement of materials performance. We can now see that grain boundary design and control could increase the strength, ductility, and corrosion resistance of materials. However, little has been studied in the past on improving fracture arrest and fracture toughness by changing the grain boundary character distribution. In particular, little quantitative work has been done on the fracture behavior influenced by the structural change of grain boundaries at both experimental testing and computer modeling [Watanabe 1993B].

2.1.4. Material Process for Grain Boundary Design and Control

Grain boundary can be controlled through material processes, such as annealing, rolling, recrystallization, and strain annealing. Intergranular brittleness is the primary problem in developing ordered intermetallic alloys as future high performance materials [Watanabe 1993A]. Ni_3Al is a typical and extensively studied ordered alloy. Unfortunately, the problem of intergranular brittleness has not yet been solved. Indeed, the ductility improvement by the addition of boron appears to have been well accepted as a solution to the problem in polycrystalline Ni_3Al. There are various studies on boron-doped Ni_3Al alloy [Liu et al. 1985, Takeyama and Liu 1988, George et al. 1989]. However, the problem of intergranular fracture in boron-doped Ni_3Al has not yet been solved and remains an important issue in the development of this material [Chuang et al. 1991]. Further, it is unclear whether the element which is beneficial for ductility improvement at room temperature is so at high temperature. Moreover, the boron addition for ductility improvement is beneficial only for hypostoichiometric Ni_3Al alloy

[Watanabe 1993A].

Quite recently, Hirano [1990, 1991] brought about a breakthrough in this area. He found that unidirectional solidification by zone-melting can drastically improve the ductility of polycrystalline Ni_3Al without boron. It is surprising that so-called inherently brittle Ni_3Al could be made ductile without the addition of boron or another third element. The alloy grown by unidirectional solidification has the columnar-grained structure of Ni_3Al and shows about 60% large tensile elongation at room temperature along the columnar structure. Of particular interest is that it also shows tensile elongation (about 15%) in the structure's transverse direction. Cold rolling at room temperature was additionally found to be possible without the addition of ductility enhancing elements. It has been found that the observed improvement in the ductility of undoped Ni_3Al polycrystal is due to the introduction of a high frequency (>70%) of low angle boundaries and low Σ (3, 9) coincidence boundaries [Watanabe 1993A].

Lin and Pope [1993] measured the distribution of grain boundary types along intergranular cracks in annealed Ni_3Al alloy with Σ value, and compared it to the distribution in the bulk, using statistically significant sample sizes. It was found that low angle $\Sigma 1$ boundaries and symmetrical $\Sigma 3$ twin boundaries are particularly strong, while low Σ, high angle boundaries, as a group, are not so strong, and high Σ, high angle boundaries are weak. This means that the strength of a polycrystalline aggregate with weak grain boundaries can be increased by increasing the fraction of $\Sigma 1$, symmetrical $\Sigma 3$ twin and possible a few other special boundaries.

Chiba et al. [1994] also examined the grain boundary character distributions in cast, recrystallized and strain annealed Ni_3Al alloys. The frequencies in cast, recrystallized and strain annealed Ni_3Al alloys are 26.8, 43.1 and 58.4%, respectively, of the total number of boundaries examined. The strain annealed Ni_3Al alloy is found to exhibit elongation to fracture of more than 45%. This significant increase in elongation of the strain annealed Ni_3Al alloys is attributed to the presence of relative low energy $\Sigma 1$ and $\Sigma 3$ boundaries.

2.2. Computer Model of Intergranular Fracture at Microscopic Level

A simple geometric model was recently proposed by Palumbo et al. [1991] to evaluate the potential effects of grain boundary design and control on intergranular degradation phenomena, such as intergranular cracking (IGC) and intergranular stress corrosion cracking (IGSCC). This model can be considered to be generally applicable to all bulk polycrystalline properties which are dependent upon the presence of "active" intergranular paths, e.g., intergranular corrosion, creep, etc [Aust 1993]. The IGC and IGSCC susceptibility can be considered in terms of the probability of finding a continuous path of intrinsically susceptible grain boundary segments, which are each favorably oriented to the applied or residual tensile stress axis, extending to a critical length, L_{crit}, within the component. This critical length defines a limit beyond which crack propagation would continue to component failure, even in the absence of either active grain boundary paths or a corrosive environment. A susceptible grain boundary segment is defined as a crystal interface, which as a result of its structural and/or chemical characteristics, is prone to preferential fracture or sliding under the local operative stress conditions, and/or to enhanced corrosion (relative to the lattice) in the specific environment. Bulk IGC or IGSCC immunity can be achieved by increasing the fraction of non-susceptible grain boundaries in the boundary distribution to a level at which the probability of inter-crystalline crack extension to the critical length approaches zero. The advantages of this model are its simplicity and ability to predict the fracture arrest distance in terms of the fraction of grain boundaries in the distribution which are intrinsically resistant to cracking and unfavorably oriented to the effective stress (grain shape factor). The disadvantage is its failure to include the realistic microstructural factors and realistic grain boundary character distribution.

Another model was proposed by Lim and Watanabe [1989, 1990] to evaluate the effect of different types, frequencies, and configurations of grain boundaries, known as the grain boundary character distribution (GBCD), on the toughness of a polycrystal made up of hexagon-shaped grains for 2D and tetrakaidecahedron-shaped grains for 3D microstructure with the loading axis lying along one of the crystal grain axes. The results show that the toughness of a polycrystal increases monotonically with an increase in the overall fraction of fracture-resistant low energy boundaries in the material. A brittle-ductile transition, corresponding to a change of fracture mode from one that is predominantly intergranular with low toughness to one that is predominantly transgranular with high toughness, is observed when the overall fraction of low energy boundaries reaches a critical value. The advantages of this model are its simplicity and ability to predict the fracture behavior in terms of the fraction of low energy grain boundaries. The disadvantage also is its failure to include the realistic microstructural factors and realistic grain boundary character distribution.

A microstructural mechanics model was presented by Srolovitz et al. [1992] to understand the effect of microstructure on the fracture of polycrystalline, elastic materials, and in particular to examine the effects of grain size and grain boundary cohesion on the transition between intergranular and transgranular failure. The mechanics employed in the simulations are based upon the elastic properties of a network of springs. The model consists of a triangular array of lattice points which are connected by bonds. The polycrystalline microstructure used in the model is produced using Monte Carlo simulation procedure introduced by Srolovitz and co-workers [Srolovitz et al. 1983, Grest et al. 1988]. This procedure has been shown to produce microstructure with grain size and grain topology distributions in excellent accordance with the experiment. Chen et al. [1993] proposed a similar microstructural model to study the transformation toughening in brittle composites which used a "ball-and-spring" discrete micromechanical model to calculate the fracture properties of grain boundaries. The advantages of these models are their realistic simulations involving realistic microstructure of materials, and their predictions of the crack paths in terms of relative grain boundary cohesion. The disadvantage, again, is their failure to include the realistic grain boundary character distribution, and lack of real data for special grain boundaries during the simulations.

2.3. Fracture Stress of CSL Grain Boundary

The dependence of intergranular fracture on grain boundary structure has been studied by many engineers using bicrystals of normally brittle materials such as refractory metals and diamond cubic materials. Kobylanski and Goux [1971], Brosse et al. and Kurishita et al. [1983A, 1983B] measured the fracture stress of molybdenum bicrystals with <100>, <110> tilt and <110> twist boundaries, while Sato et al. [1989] studied silicon bicrystals containing a <111> twist boundary of different misorientations. Table 2.2 gives the fracture stress reported by the various investigators for several Σ coincidence boundaries and random boundaries [Lim and Watanabe 1990]. Several features can be seen in this table. First, the fracture stress or the crack extension force of coincidence boundaries (including Σ1/low angle boundaries) is always several times greater than that of random boundaries. Second, even though the reported fracture stresses are found to vary somewhat from one boundary type to the next, it is interesting to note that the ratio of the fracture stress of coincidence boundaries to that of random ones (σ_Σ/σ_R) increases with decreasing Σ value, irrespective of test conditions and materials. Third, the limited data given in Table 2.2 indicated a lower σ_Σ/σ_R for twist than for tilt boundaries. This, however, could be attributed to a much higher σ_R for twist boundaries, as indicated by the results of Kurishita et al. [1983A, 1983B].

Kurishta and Yoshinaga [1989] also have studied the effect of grain boundary type, misorientation and material purity on intergranular fracture stress in molybdenum bicrystals. The results showed that the fracture stress for high purity molybdenum bicrystals is high at a misorientation angle smaller than 10° and that corresponding to Σ3 coincidence orientation, while much lower than that for low purity bicrystals at a misorientation angle between 20° and 50°. The twist bicrystals showed a more significant misorientation effect on the fracture stress, but material purity was seen to have had little effect. It is easy to see that the fracture stresses of bicrystals strongly depend on the type and structure of the grain boundary and it can also be affected by material purity through the effect of grain boundary segregation. This could be one of the sources of the extrinsic intergranular fracture which is often observed. Another important conclusion is that low energy boundaries such as low angle and low Σ grain boundaries are not good sites for segregation, and therefore, they are insensitive to material purity irrespective of the type of grain boundary [Watanabe 1993A]. These experimental data are very useful and important in "grain boundary control and design."

Table 2.2 Fracture stress of coincidence boundaries [Lim and Watanabe 1990].

Materials	Type of boundary	Test condition	σ_Σ (MPa)	σ_R (MPa)	σ_Σ/σ_R
Mo	<100>Sym. tilt	R.T.[a]	1340 (5°Σ1) 1150 (8°Σ1)	75	17.8 15.3
Mo	<110>Sym. tilt	R.T.	800 (109°Σ3) 570 (50°Σ11)	88	9.1 6.5
Mo	<100>Sym. tilt	R.T.	533 (9.3°Σ1)	106-120	4.4-5.0
Mo	<110>Sym. tilt	R.T.	293 (10°Σ1) 400 (110°Σ3) 400 (50°Σ11)	67	4.4 6.0 6.0
Mo	<110>Sym. tilt	77K	1720 (70°Σ3)	280	6.1
Mo	<110> Twist	77K	1440 (73°Σ3)	623	2.3
Si	<111>Twist	R.T.	300 (25°Σ7)	140	2.1

[a]R.T. = room temperature.

Unfortunately there is very little experimental data available, and these kinds of bicrystal experiments are very difficult to be done for most of metals and alloys. Thus, very few bicrystal experiments have been carried out to study the intergranular fracture. The formidable difficulties of such experimental study results from the complexity of the phenomenon and the large number of parameters and variables involved. Difficult problems have to be solved at every stage of an experiment, from sample preparation where one needs to control the interfacial structure, to sample characterization, and to the measurement of details of the fracture process. These experimental difficulties, in contrast, serve to emphasize the considerable opportunities for atomistic modeling and simulations. It is precisely the inherent nature of atomistic calculations that makes it possible to specify the interatomic structure and forces, to determine the atomic configuration at any stage of the system relaxation and evolution, and to follow the molecular details of dynamic processes. Therefore the intergranular fracture of the bicrystal could be easily approached by molecular dynamics (MD) simulation [Yip and Wolf 1989].

2.4. Interatomic Potentials for Atomistic Model

The recent developments of interatomic potentials are part of a larger project of designing a mathematical model which can be used to perform computer simulation for various properties of materials which are ultimately controlled by interatomic interactions. There have been numerous reviews and conference proceedings [Allen and Tildesley 1991, Johnson 1988, Lee 1981] with regard to this field. The general requirements for a model are that it is both accurate enough to permit a broad range of experiments, with a reasonable expectation that the results will be physically meaningful, and simple enough to do within our existing computer capacity. For atomistic calculation, a mathematical model is simply an equation for the energy of the materials as a function of the positions of all atoms; given the atomic arrangement, the energy can be computed. In practice, it is normally only the difference in energy between two sets of atomic positions, or configurations, that are of interest, which leads to considerable simplification in the calculations.

Carlesson [1985] emphasized that the nature of the interatomic potential that can adequately handle a given situation depends on the type of problem under consideration and on the local atomic environment. Long-range interactions such as the semiempirical forms and pseudopotentials are most applicable to cases in which the overall volume of the materials is unchanged and there is little change in volume on a local scale, such as lattice vibrations, liquid structure factors, and bulk crystal structures. The short-range empirical potentials are applicable to situations involving "bond breaking" and significant volume change. However, a model based solely on two-body forces has its drawbacks. For example, unless the elastic constants in a cubic crystal satisfy the Cauchy relation $C_{11}=C_{44}$, which is seldom the case in real materials, an equilibrium pair-potential model cannot accurately reproduce them. It is customary to deal with this problem by adding to the pair-potential in the total energy a term which depends on the macroscopic volume of the materials [Finnis and Sinclair 1984, Daw and Baskes 1984], by analogy with simple-metal perturbation theory. The elastic constants can then be adjusted arbitrarily at equilibrium because the volume-dependent term supplies a fictitious external pressure to balance the so-called Cauchy pressure $\frac{1}{2}(C_{12}-C_{44})$. While this generalization is a gross simplification, it provides a starting point for discussing recent developments.

2.4.1. Central-Force (Pair) Potential (Long-Range, No Volume Dependence)

From a conceptual viewpoint, one can discuss the various potential models by expressing the $U(\mathbf{r}_N)$ of the system as [Allen and Tildesley 1991]:

$$U(\mathbf{r})=\sum_{i} V_1(\mathbf{r}_i)+\sum_{i}\sum_{i<j} V_2(\mathbf{r}_i,\mathbf{r}_j)+\sum_{i}\sum_{i<j}\sum_{i<j<k} V_3(\mathbf{r}_i,\mathbf{r}_j,\mathbf{r}_k)+\ldots, \qquad (2.1)$$

where $V_1(\mathbf{r}_i)$ is the one-body potential which depends on the position of atom i, $V_2(\mathbf{r}_i,\mathbf{r}_j)$ is the two-body potential, and so on. Since the simplest possible representation of many-body interactions is the sum of two-body interactions, a widely adopted approximation is to take only the second term in the equation (2.1).

Within the pair approximation, there exist empirical expressions in the form $V_2(|\mathbf{r}_i-\mathbf{r}_j|)$ which involves the additional assumption of centrally-symmetric forces. The well-known example is the

Lennard-Jones (6-12) potential [Lennard-Jones 1924, Barker 1976]:

$$V_2(r) = 4\epsilon [(\sigma / r)^{12} - (\sigma / r)^{6}] \tag{2.2}$$

with well-depth parameters ϵ and lengths σ fitted to experimental data which can be thermodynamic properties, defect energies, and/or elastic moduli. These potentials are reasonable descriptions of two-body forces to the extent that they account for repulsion due to the overlap of electron clouds at close interatomic separations and attractive forces at large distances due to dispersion effects.

However, as discussed above, owing to the intrinsic limitations of central-force potentials, the properties of certain materials cannot be reproduced regardless of the number of disposable parameters. This shortcoming of central-force potentials has been a major motivation in the development of a border conceptual framework for the description of interatomic interactions, particularly in metals and alloys.

2.4.2. Pseudo-Potential (Long-Range, Volume-Dependent)

Pseudopotentials pertain to the forces seen by electrons in the determination of their quantum-mechanical wave functions and are not directly related to the interatomic potentials required for lattice calculations [Wang and Lai 1980, Esterlin and Swaroop 1979, Dagens et al. 1975, Dagens 1986]. The electron energy bands of some metals are surprisingly similar to the predictions of a free, or nearly free, electron model. This has led to a formulation based on a perturbation expansion for the electron wave function, in which the effective interaction between the ion cores and the conduction electrons, called a pseudopotential, is assumed to be weak. The overall lattice pseudopotential is then written as a sum of pseudopotentials arising from individual ions. The pseudopotentials are actually operators, but the approximation is commonly made that they are simply functions of position, in which case they are called local pseudopotentials. The result of these steps is that, given the positions of the atoms, the energy of the system can be calculated. Furthermore, the energy can be factored into structure-independent (that is, volume-dependent) and structure-dependent components, with the majority of the cohesive energy accounted for by the volume-dependent term. Finally, the structure-dependent terms can be Fourier-transformed to yield an effective ion-ion potential. Thus, a model can be developed from first principles which involves two-body interatomic potentials and the overall volume dependence of the structure. With the absence of three- and higher-body interactions, the energy $U(\underline{r};\Omega)$ can be expressed as [Harrison 1966, Lu and Szpunar 1992]:

$$U(\underline{r};\Omega) = \frac{3}{2}k_B T + \frac{1}{2}\sum_{i\neq j} V(\underline{r}_{ij};\Omega) + V(\Omega) \tag{2.3}$$

where $\underline{r}$ and Ω are the position vectors and mean atomic volume, respectively, and the first term represents the kinetic energy of an ion in the classical limit [Leung et al. 1976], and $V(\Omega)$ and $V(\underline{r}_{ij};\Omega)$ represent, respectively, the one- and two-body interactions.

Figure 2.3 is a plot of the total effective pair potential for aluminum calculated by the non-local model pseudopotential (EINMP) theory [Wang and Lai 1980]. The volume dependence of the pair interaction is clearly apparent, and plays an important role in constant pressure (N-P-T)-MD simulation for a metal or an alloy system.

This approach is not without its difficulties, however, since the long range of potentials makes it awkward to use them in efficient relaxation calculations, and, due to the oscillations, the results are dependent on the cutoff distances if they are shortened. With the capacity of computers increasing, however, this problem can be easily solved. The nature of the potential near the first-neighbor separation distance is dependent on very fine aspects of the theory so that it can be completely altered by some minor variations. The theory is not readily applicable to transition metals with a significant d-band character contribution, but to simple metals in which there is little overlap of the ion cores, with aluminum as the prototype [Dagens et al. 1975] and to the alkali metals. A generalized pseudopotential theory applied to transition metals has been published by Moriarty [1985] in which three-body forces are included. The conclusion is that a contribution of three-body forces are significant and must be used for metals in the middle of a transition series, such as chromium and vanadium, but have little effect on nickel and copper.

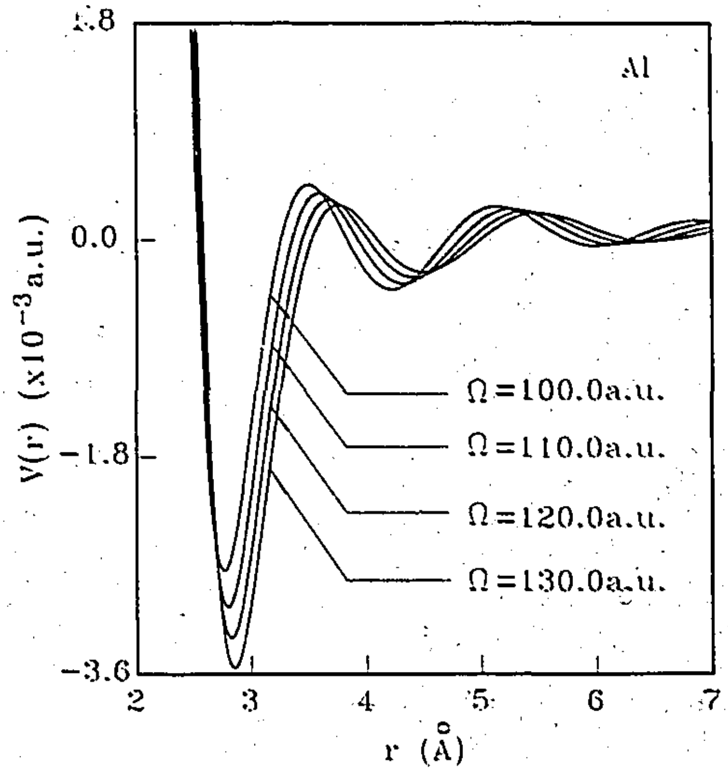

Figure 2.3 Total effective pair potential for aluminium calculated from the non-local model pseudopotential (EINMP) theory [Wang and Lai 1980].

2.4.3. EAM Potentials (Short-Range, Volume-Dependent)

Although central-force potentials provide a good description of the short-range repulsion between the atoms, the attraction between atoms at larger separations, required for the cohesion of all materials, is not conceptually well described by a central potential in the case of metallic bonding. The attraction between ions in a metal arises from the decrease in the energy of the electron gas when embedding the ion cores in the Fermi sea. This is the major development in models in this category with a more complex term which at first looks like another two-body potential [Finnis and Sinclair 1984, Daw and Baskes 1984]:

$$U(r) = \sum_i F_i(\rho_{h,i}) + \frac{1}{2}\sum_{i,j,j\neq i}\phi_{ij}(r_{ij}) \tag{2.4}$$

This new term, which is used both in the embedded atom method developed by Daw and Baskes [1984] and by Finnis and Sinclair [1984], can be interpreted in a variety of ways. The embedded atom derivation is based on the density functional theory, and the function $F_i(\rho_{h,i})$ is the energy to embed that particular atom in a uniform electron gas of density ρ_i and depends only on the element. Three basic assumptions are usually made [Daw and Baskes 1984, Foiles et al. 1986]:

(a) The electron densities are assumed to be centrally symmetric; the density $\rho_j(\underline{r})$ contributed by some atom j at $\underline{r}$ is assumed to depend only on the distance $|\underline{r}|$.

(b) By assuming atomic electron densities, all electron densities are assumed to be independent of the environment; self-consistent rearrangements in the electron gas are ignored. As a result, the total electron density ρ_i at a particular atom arising from all the other atoms can be taken as a linear superposition of atomic densities $\rho_j(r_{ij})$

$$\rho_{h,i} = \sum_{j\neq i}\rho_j(r_{ij}) \tag{2.5}$$

(c) The short-range repulsion is assumed to be of a central-force type.

Although not explicitly a volume contribution to the energy, this term is dependent on crowding in the lattice. From a purely empirical point of view, it can be considered to be a measure of local volume dependence. Since the model parameters are obtained by empirical fitting, results are independent of the physical interpretation. In practice, this new form would seem to be the natural successor to the empirical models. In addition, the scheme is adapted to treating surfaces, and since the embedding functions are independent of the source of the electron density, it is directly applicable to alloys. In a short time, quite extensive calculations have been carried out under the heading of the embedded atom method. Encouraging results have been obtained with respect to surfaces, impurities, lattice defects, alloy segregation at surfaces, impurity trapping at grain boundaries, liquid metals, hydrogen embrittlement, and fracture.

2.4.4. Summary of Interatomic Potentials

Whether interatomic potentials are derived with approximations from first principles or are purely empirical, their use in modeling is extended beyond their original region of applicability. Computer simulation may be seen to be theoretical or empirical process of matching one region of configuration space which is understood or for which there are experimental data to a different region which less is known. There is no uniqueness: some other scheme may be found which does just as well in the known region but which gives different results in the region under study. In principle, computer modeling of materials is seen to be very straightforward. A primary input for all models is a two-body central potential, a continuous function of distance which is independent of orientation, and is summed over all possible pairings in the materials. These potentials are taken as constant in most models, but calculations based on the pseudopotential theory are often carried out at a constant volume because the two-body interactions resulting from pseudopotential theory are functions of volume. The range of two-body potentials effectively varies from less than second-neighbor distance in the crystal lattice to thousands of atoms, and the shorter the range of the potential, the faster the computer calculations.

While models based on two-body Lennard-Jones do not require additional energy contributions, they do not provide a good simulation of the metals and alloys. The many-body factor used to overcome these difficulties has most commonly been taken as a function of overall material volume. Short-range empirical models with this volume dependence have provided a crude but workable model for "bond breaking" calculations. Traditional thinking has established that pseudopotential theory is applicable only to simple metals, and not to noble and transition metals, and its use for metals has generally been restricted to aluminum, for which numerous calculations have been performed. However, recent extensions to noble [Heine and Weaire 1970] and transition [Lam and Dagens 1988] metals have been proposed. Models based on local volume dependence have recently been developed and extensive calculations have been carried out with the embedded atom method [Daw and Baskes 1984], which has yielded meaningful results over a broad spectrum of topic. They have an advantage over pseudopotential models and are efficient in the use of computer resources. Both the uses of pseudopotentials for nonsimple metals and the development of the embedded atom method are sufficiently new that further investigation is required to understand their ramifications. Computer efficiency favors the embedded atom method, and there are no worrisome clouds on the horizon to indicate that its results might not be physically meaningful.

2.5. BORDER CONDITIONS

No computer simulation can be performed without the establishment of proper boundary conditions for the computational cell. There are four principal possibilities [Allen and Tildesley 1991, Beeler 1988]:

- Free-surface boundary;
- Rigid boundary;
- Flexible boundary;
- Periodic boundary.

Normally, the computational cell contains 500 to 10,000 atoms. As such, it represents a very small piece of materials, 600 atoms being a microfemtomole. The free-surface case pertains to a large, free molecule. Macroscopic materials are simulated through the use of either rigid, flexible, or periodic boundary conditions. In the rigid boundary case, a mantle of fixed-position atoms representing the materials structure is placed around the computational cell. The thickness of the mantle is made larger than the range of the interaction between atoms. The mantle represents the part of the macroscopic materials that can interact with atoms in the computational cell. The defect under study is contained in the computational cell. The flexible boundary approach is more realistic than the rigid boundary approach, in that the boundary region is capable of small atom displacements in response to forces exerted on it by atoms at the perimeter of the computational cell. It has been shown that a rigid boundary can be used in studying point defects. However, certain types of simulations for complicated defects require the use of flexible boundary conditions. One of these, for example, is a Peierls stress computation for dislocation movement. Periodic boundary conditions are often used to simulate large systems. Roughly speaking, periodic boundary conditions simply mean that atoms at the extreme right of the computational cell interact with those at the extreme left of the cell. Similarly, atoms at the top of the cell interact with those at the bottom, and atoms at the front interact with those at the back. When periodic boundary conditions are used, the cell diameter must exceed twice the interaction range between two individual atoms. Over the past several years, the capability of the periodic boundary conditions approach has been vastly enlarged. As described above, the periodic boundary condition mode restricts the simulation to a computational cell with a fixed volume and shape. Therefore, certain phase transformations cannot be simulated. Recent developments allow changes in both the volume and the shape of the computational cell as the simulation proceeds when periodic boundary conditions are used [Andersen 1980, Parrinello and Rahman 1981].

However, in practice the problems are not so simple. The border condition must be a multiplied boundary condition along the main axis of the computational cell, for example, for interfacial and surface problems. One is faced with the simultaneous requirements of a small simulation cell for economy of computations and a large cell so the interfacial and surface regions are not perturbed artificially by the action of the cell borders. In simulation studies of grain boundaries, the bicrystal model is used in which a planar interface, infinite in extent, is represented by a finite simulation cell with border conditions which are periodic in the two directions along the interface (x and y border) [Henderson and Van Swol 1984, Van Swol and Henderson 1984]. In the direction perpendicular to the interface, z borders are expected to simulate the bulk media on either side of the interface. If one imposes periodic conditions on these borders as well (thus imposing three-dimensional periodic border conditions on the system), then there will necessarily be two interfaces in the cell, a situation considered unsatisfactory since the two interfaces can influence each other and, in the case of grain boundaries, even annihilate each other at high temperatures. Also, because of the coupling through the z border, the two halves of the bicrystal are not free to translate relative to one another arbitrarily. In addition to the problem of avoiding two interfaces, it is also necessary for the z borders to be sufficiently flexible to accommodate any deformation or volume change that may occur in the (inhomogeneous) interfacial region during the simulation.

Lutsko et al. [1988] have recently developed a reasonable border condition for an interfacial system. For an isolated interface, one which is embedded in two semi-infinite bulk ideal crystals, two-dimensionally periodic border conditions in the two directions parallel to the interface are clearly appropriate. As long as the interface is planar and coherent, i.e., as long as it can be characterized by a periodic planar unit cell, two-dimensional periodic borders are appropriate in the interfacial plane. This embedding is accomplished by surrounding the interface region and two semi-infinite bulk ideal crystals. With the same two-dimensional periodic boundary conditions applied in directions x and y to both the interface region and bulk ideal crystals, the system has no free surfaces.

When thermal motions are considered in the calculation, the assumption of the two-dimensional periodic boundary condition for the interface region and two semi-infinite bulk ideal crystals is still appropriate. Under these conditions, however, the periodicity enforced by the border conditions gives rise to a limitation on the dynamical processes that can be studied. As is well known in Molecular Dynamics simulations, the system under investigation cannot propagate phonon with wavelengths greater than the dimension of the simulation system. A method for treating the z-borders at finite temperatures in a less-constraining manner has recently been proposed [Lutsko et al. 1988]. Unlike three-dimensional periodic boundary conditions, this approach provides a simulation cell containing a single interface, and in contrast to the condition of a fixed z-border [Balluffi et al. 1981], it accommodates dimensional changes normal to the interface as well as translational motions parallel to the interface plane. The new method also makes use of the configuration with the interface region and two semi-infinite bulk ideal crystals, where in the interface region the particles are treated explicitly, and two semi-infinite bulk ideal crystals consist of two semi-infinite rigid blocks of atoms held fixed at their ideal-crystal positions. The novel feature is that the rigid blocks are allowed to move by translations parallel to the interface plane, such motions being determined by the force exerted on the blocks across the interface and ideal crystal border. The blocks are also allowed translations in the z-direction; these movements are treated separately from the parallel translations and are governed by the pressure exerted on the blocks by the interface region [Lutsko et al. 1988]. Applications of this method to bicrystals at high temperatures have given satisfactory results [Lutsko et al. 1989].

Therefore, for practice problems, a proper border condition in certain directions should be chosen.

2.6. Atomistic Computer Simulation methods

Computer simulations play a valuable role in providing essentially exact results for problems in statistical mechanics which would otherwise only be solvable by approximate methods, or which might be quite intractable [Ronchetti and Jacucci 1991, Allen and Tildesley 1991, Yip and Wolf 1989]. In this sense, computer simulation is a test of theories and, historically, simulations have indeed discriminated between well-founded approaches and ideas that are plausible but, in the event, less successful. The results of computer simulations may also be compared with those of real experiments. In the first place, this is a test of the underlying model used in a computer simulation. Eventually, if the model is good one, the simulator hopes to offer insights to the experimentalist, and assist in the interpretation of new results. The dual roles of simulation, as a bridge between models and theoretical predictions on one hand, and between models and experimental results on the other, are illustrated in Figure 2.4. Because of this connecting role, and the way in which simulations are conducted and analyzed, these techniques are often termed 'computer experiments'. Computer simulation provides a direct route from the microscopic details of a system (the masses of atoms, the interactions between them, molecular geometry, etc.) to macroscopic properties of experimental interest (the equation of state, transport coefficients, structural order parameters, and so on). This type of information is not only of academic interest, it is also technologically useful. It may be difficult or impossible to carry out experiments under extremes of temperature and pressure, while a computer simulation of the materials would be perfectly feasible. Subtle details of molecular motion and structure are difficult to probe experimentally, but can readily be extracted from a computer simulation. Finally, because of the speed of molecular events and experimental difficulty, it presents no hindrance to the simulator. A wide range of physical and mechanical phenomena, from the microscopic to the macroscopic scale, may be studied using various form of computer simulation.

In this section, we will review the atomistic computer simulation methods which make possible an approach to the investigation of most problems in material science and engineering. These methods are all concerned with a common model system, in which a collection of N interacting atoms arranged in a given initial configuration has already been defined. The total energy of the system is prescribed and a set of border conditions has been specified.

Of the various computational methods which can be applied to this atomistic model, we will consider only two techniques: lattice statics (LS) [Yip and Wolf 1989] and molecular dynamics (MD) [Allen and Tildesley 1993]. While each method is well established in its own area of application, their combined use in the study of materials constitutes a new approach which we believe is capable of providing invaluable insights. In what follows we will briefly examine the physical basis of each method, indicate their complementarity, and review the relative advantages and limitations of each.

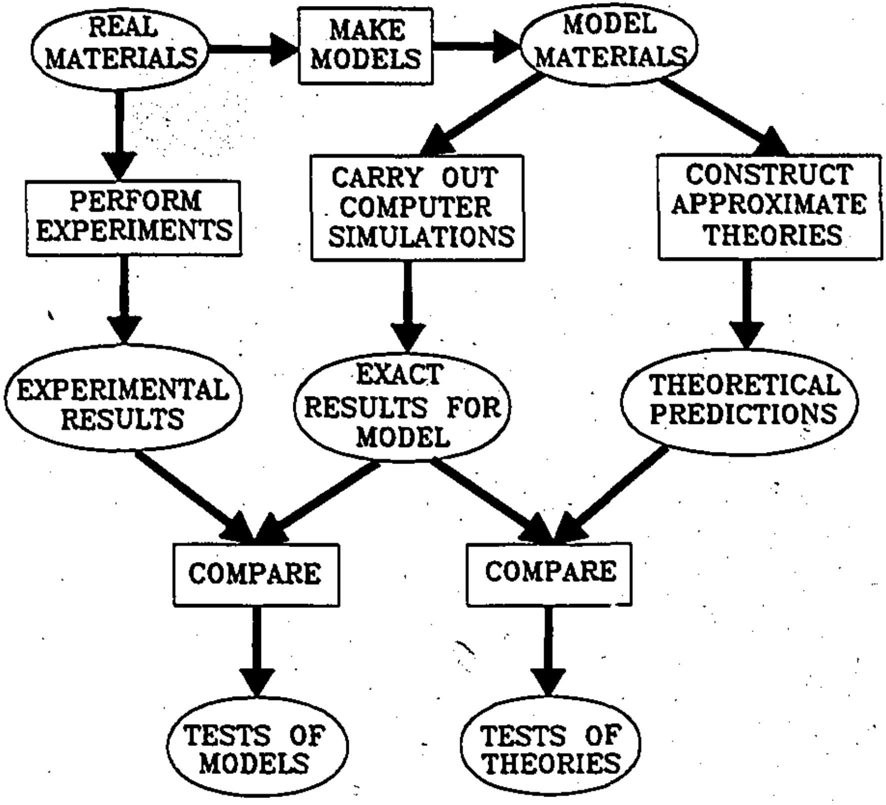

Figure 2.4 Connections between experiment, theory, and computer simulation.

2.6.1. Lattice Statics (LS)

This is a method which enables one to determine the zero-temperature, relaxed, non-vibration structure of the simulation system by minimization of energy. It has been widely used in problems dealing with low-temperature structure, high-temperature non-vibration structure and energetic of defects in liquid, amorphous and crystalline state. The basis of the method is that: if it is desired that the configuration of system be an equilibrium configuration, then by definition the force on any atom i must vanish in this configuration:

$$E_i = -\frac{\partial V}{\partial r_i} = -\sum_{j\neq i} \frac{\partial V_j(r_{ij})}{\partial r_{ij}} \tag{2.6}$$

In lattice-statics calculations, energy minimization is carried out by moving each atom in the direction of the force acting on it by a certain amount. This amount can be governed by the volume of the force acting on the atoms or, in simpler schemes, can be chosen more or less arbitrarily. The process is repeated until all forces are reduced essentially to zero, i.e., below some numerically small value. The system is then considered "relaxed". The configuration and energy thus obtained are the structure and energy of the system at T=0, since at zero temperature the higher-order terms of energy vanish and the system is in an equilibrium configuration.

Using steepest descent, conjugate gradient, or other minimization procedures, lattice relaxation can be carried out efficiently to systematically study structures and energy over a wide range of geometric parameters. However, when the system contains an interface, it is not sufficient to relax only the atoms. The border conditions may also need to be adjusted in response to the atomic relaxations at the interface according to the internal stress and the pressure of the system.

2.6.2. Molecular Dynamics (MD)

This method, in its most straightforward realization, is a very simple technique. Given the interaction potential and an initial configuration of N particles at time t, the resulting forces acting on each atom are calculated [Allen and Tildesely 1993]. Newton equations of motion are then numerically solved for a small time interval Δt under the assumption of constant force, resulting the system configuration at time t+Δt. In the limit Δt→0 the solution is exact. The procedure can be iterated ad infinitum and the evolution of the system can therefore be followed. In its simplest and most often used form, MD is based on the equations of motion derived by the classical Lagrangian:

$$\mathcal{L} = \frac{1}{2}\sum_{i}^{N} m_i \frac{d^2 r_i(t)}{dt^2} - \sum_{i>j}^{N} V(r_{ij}) \tag{2.7}$$

where m_i and $\mathbf{r}_i$ are mass and position of the i-th particle, and V(**r**) is the interaction potential. Given the initial configuration of the atoms and the border conditions, these equations are integrated numerically to give the future positions of the atoms at discrete time steps. The basic output of MD consists of the particle trajectories which constitute the complete solution to the model system as formulated in classical mechanics. Through the knowledge of how the system evolves in time, one can determine all of the equilibrium and dynamical properties of interest [Allen and Tildesley 1991, Ciccotti et al. 1987].

In MD all particles are displaced from one time step to the next in accordance with equation (2.7). Each particle, therefore, has an instantaneous velocity and kinetic energy. For the system, one can define the instantaneous temperature as proportional to the total kinetic energy, a quantity which fluctuates in time as the particles move through regions of different potential interaction. It is through these fluctuations that entropic effects enter into the simulation. Because of this property, MD is valid for classical systems at any temperature. In practice, the validity of the MD approach is limited to temperatures near or above the Debye temperature of the materials. To the extent that the interatomic potential is specified for all interparticle distances, the simulation is also valid for arbitrary deformation of the system. It is worth noting that in a classical system not only can the simulation be carried out at any temperature desired, but the system response to a temperature change can also be studied.

MD can be used to calculate time averages of physical quantities of interest, or as a powerful microscope to examine in detail local configurations and typical atomic trajectories. By adding a dissipative term to the equations of motion, the method can also be used to find local minimum in the potential energy. MD can also serve as a tool for studying non-equilibrium phenomena. Relative to lattice statics, MD can be regarded as a method for determining how a model system which is relaxed at T=0 behaves at finite temperature and external stress. The effects of external stress can be treated either through the border conditions or modification of equation (2.7) by introducing an appropriate Lagrangian [Andersen 1980, Parrinello and Rahman 1981]. By "behavior" we mean here both the equilibrium properties such as thermal expansion and mechanical responses such as elastic constants. In the last several years, much work has been devoted to generalizing the method to different statistical ensembles. Such generalizations are obtained by writing an ad hoc Lagrangian, and then showing that the equation of motion obtained from it generates the trajectories of the desired statistical ensemble. For example, the extension led to constant pressure MD [Andersen 1980]. For such a system the Lagrangian is as follows:

$$\mathfrak{L} = \frac{1}{2}\sum_{i}^{N} m_i \frac{d^2 r_i(t)}{dt^2} - \sum_{i>j}^{N} V(r_{ij}) + \frac{1}{2} W \left(\frac{d\Omega}{dt}\right)^2 - P\Omega \tag{2.8}$$

where W is a coupling parameter which can be thought of as the mass of a piston, and the volume Ω becomes an additional dynamical variable. Today it is possible to study systems at constant temperature, strain, volume or pressure.

2.7. Problems in the Atomistic Model

However, in spite of all the possible advances in computer models and methods, and computer speed, it seems that computer simulation in its atomistic form will not be able to tackle a vast class of phenomena [Ronchetti and Jacucci 1991, Allen and Tildesley 1991]: those connected with materials science and engineering. There are fields which, due to their spatial or statistic complications, need computer modeling: the range between 1μ and 100μ is inaccessible to atomistic simulation. The physics of this range, which cannot be described on a microscopic basis, and cannot be represented by statistical mechanics is now known as mesoscopic physics. Its complications are intrinsic, and the continuum representation breaks down. The phenomena are similar to catalysis, corrosion and the formation and migration of dislocations, grain boundaries, microfractures in that require modeling and testing. Computer simulation, in a new form, is exactly what can help to solve the problems. We have learned in fact by now that simulation, in its double function of testing theories and testing models, can give an invaluable support to the advance in understanding the world. We expect, therefore, that in the near future new techniques will be developed to bridge the gap between the microscopic and macroscopic, and will promote a computer simulation of materials at the mesoscopic level, as opposed to macroscopic and microscopic levels.

Such techniques will be different from both macroscopic and microscopic approaches. Comparing the methodology of numerical modeling of continuous bodies (as a field in applied mathematics and engineering) and that of atomistic modeling of condensed matter (as a field in solid state physics and statistical mechanics), differences in empirical input and founding equations are apparent.

In finite element treatments of deformations of continuous bodies, the constitutive properties of materials (e.g., stress vs. strain plots) are inputted into continuity and conservation equations. Mechanical properties (elastic and plastic behavior, fluid flow), thermal properties (heat flow) and their coupling can thus be computed. Complications can be introduced into the models by geometrical and surface effects as well as by the presence of regions characterized by different constitutive properties.

In the atomistic modeling of materials, alternatively, atomic interactions derived either from the fitting of experimental behavior or from ab_initio calculations are used in the classical equations of the motion of particle assemblies. The resulting equation of state yields mechanical and thermodynamic properties of the material under study. Transport coefficients can also be computed by this method. Some complications such as interfaces and board, can be introduced at the atomistic level.

Atomic modeling of materials at the micron scale is not practical, however, while the homogeneous continuum model is often inapplicable in real materials much below the millimeter scale. Furthermore, microstructure is often too complex to be described with the introduction in the Finite Elements model of multiple different spatial regions. As a result, materials science and engineering lack well-established computer modeling and simulation methods precisely at the length scale where interesting chemical physics phenomena often occur, i.e., at the mesoscopic level. Surface oxidation, powder compaction and sintering, and plasma spraying deposition of coatings are further examples of important processes related to materials where mesoscopic phenomena appear. The properties of these materials are irreducible to equivalent homogeneous models using statistical properties and distribution functions. This is related to the nonlocal features of the network of pores, cracks and channels that are essential to any useful description.

Computer simulation at the mesoscopic level involves drops and grains as actors. Their mechanical and thermal properties (e.g., splatting, solidification, heat transfer) become an empirical input. The successive happening of stochastic events influenced by steric effects and complemented by qualitative rules of behavior (which to decide the outcome of individual events) are the constituents of a procedure replacing continuum equations and particle equations of motion in mesoscopic simulation.

2.8. Summary

From the foregoing review, it should be apparent that the two atomistic simulation methods at both the atomistic and microscopic levels have an intimate interrelation that can be exploited in an integrated approach to modeling complex systems such as interface. While such an approach entails considerable effort in implementation, the benefit is also substantial, in that it enables one to take advantage of the unique capabilities of each of the two methods in a systematic investigation of structure- property correlations from zero temperature to melting, including the effects of external stresses applied to the system at both the atomistic and microscopic levels.

The goal of this work is to develop an integrated model for intergranular fracture at both the atomistic and microscopic levels which can be used to analyze a role of grain boundary character distribution (GBCD), texture, and microstructure in fracture resistance of polycrystalline materials in order to improve fracture toughness of brittle polycrystalline materials through optimization and control of the GBCD.

CHAPTER 3:

COMPUTER MODELS AND SIMULATION METHODOLOGY

As described previously, an integrated computer simulation of intergranular fracture requires a set of computer models and simulation methods to calculate the interaction between atoms, to describe the motion of atoms and bi-crystal system, to relate this motion to macroscopic quantities that are to be computed, and to describe the microstructure of polycrystalline materials, among other functions. The purpose of this chapter is to describe the principal physical models and computational techniques used to simulate the behavior of intergranular fracture which include the EAM functions, grain boundary model, initial geometry of grain boundary, grain boundary structure and energy, constant strain molecular dynamics, microstructure (Monte Carlo simulation), and the Markov chain fracture model.

3.1. Embedded Atom Method (EAM)

In the embedded-atom method (EAM) [Daw and Baskes 1984, Foiles et al. 1986], the total energy of a system of atoms is given by equation (2.4). $\rho_{h,i}$ is the background electron density at atom i due to the rest of the atoms in the system thought of as the host, and $F_i(\rho_{h,i})$ is the embedding energy of placing an atom into that electron density. $\phi_{ij}(r)$ is a short-range interaction representing the core-core repulsion, and r_{ij} is the distance between atoms i and j. The electron density $\rho_{h,i}$ is approximated by the superposition of atomic density which was given in equation (2.5). $\rho_j(r)$ is the atomic electron density due to atom j at the distance r_{ij} from the nucleus.

The par interaction term $\phi_{ij}(r)$ is purely repulsive. Analysis has shown that the pair interaction between two different species can be approximated through the geometric mean of the pair interaction for the individual species [Rimmer and Cottrell 1957, Abrahamson 1964, 1969]. This observation, along with the Coulombic origin of the pair interaction term, suggests expressing the pair interaction between atoms of types A and B in terms of effective charges as:

$$\phi_{AB}(r) = \frac{Z_A(r)\, Z_B(r)}{r} \tag{3.1}$$

The effective charge Z(r) is constrained to be positive and to decrease monotonically with increasing separation and can be assumed as a simple parametrized form as follows [Foiles et al. 1986]:

$$Z(r) = Z_0 (1 + \beta r^{\nu})\, e^{-\alpha r} \tag{3.2}$$

The value of Z_0 will be assumed to be given by the number of outer electrons of the atom and α, β, ν are three parameters to be determined. Empirically, it was found that the choice $\nu=1$ leads to a good representation of the elastic constants for Ni and Al, while $\nu=2$ worked better for Cu.

The atomic electron density is assumed to be well presented by the spherically averaged free-atom density calculated from the Hartree-Fork theory by Clementi and Roetti [1974], and McLean and McLean [1981]. Thus the atomic electron density $\rho(r)$ in EAM is computed from Hartree-Fork wave functions by:

$$\rho(r) = N_s \rho_s(r) + N_p \rho_p(r) + N_d \rho_d(r) \tag{3.3}$$

where N_s, N_p and N_d are the number of outer s, p and d electrons and ρ_s, ρ_p, and ρ_d are the densities associated with the s, p and d wave functions. The total number of s, p and d electrons is fixed to be the number of outer electrons of the atom, i.e.:

$$N_s + N_p + N_d = Z_0 \tag{3.4}$$

There are wave functions available for different atomic configurations, i.e., different occupations of the s, p and d orbital. The configurations used in the current calculations are indicated in Table 3.1.

Table 3.1 Fitting parameters defining the effective charges for pair interactions and atomic electron density. Here, Z_0 is the number of outer electrons of the atom; α, β, and ν are three parameters; N_s, N_p and N_d are the numbers of outer s, p and d electrons ($N_s+N_p+N_d=Z_0$); R_c is the potential cut-off.

	Z_0	α	β	ν	N_s	R_c	Atomic Configuration
Cu	11.0	1.7042	0.1806	2.0	1.000	4.95	$3d^{10}4s^1$
Ni	10.0	1.8813	0.8607	1.0	1.516	4.80	$3d^84s^2$
Al	3.0	1.3680	0.4550	1.0	1.645	5.50	$3s^23p^1$

The spherically averaged s, p and d electron densities are computed by [Clementi and Roetti 1974]:

$$\rho_m(r) = \frac{1}{4\pi} \left| \sum_i C_i R_i(r) \right|^2 \qquad (m = s, p, d), \tag{3.5}$$

and :

$$R_i(r) = \frac{(2\xi_i)^{(n_i + \frac{1}{2})}}{[(2n_i)!]^{\frac{1}{2}}} r^{n_i - 1} e^{-\xi_i r} \tag{3.6}$$

where i, n_i, ξ_i, and C_i for Cu, Ni and Al are listed in Table 3.2.

To derive a pair and three- or more-body interaction expression from the EAM functions, we need only look at the embedding energy, since the core-core repulsion term is already in the desired form. With a small distortion of the lattice, each atom will experience a slightly different electron density. The embedding energy can be expanded in the small difference and can then be written as the sum of effective pair interaction $\psi(r)$. Where the effective pair potential $\psi(r)$ is given by [Foiles 1985]:

$$\psi(r) = \frac{1}{2}\left[\,\phi(r) + 2F'(\rho_0)\,\rho(r) + F''(\rho_0)\,[\rho(r)]^2\right] \tag{3.7}$$

where ρ_0 is the average host electron density.

Table 3.2 Parameters i, n_i ξ_i and C_i used to calculate the atomic electron density for Cu, Ni and Al [Clementi and Roetti 1974].

		Cu		Ni				Al	
i	n_i	ξ_i (Å^{-1})	C_i	ξ_i (Å^{-1})	C_i	i	n_i	ξ_i (Å^{-1})	C_i
4s						3s			
1	1	56.70862	-0.00333	54.87048	-0.00389	1	1	26.88495	-0.004512
2	1	39.75909	-0.02322	38.47143	-0.02991	2	1	20.26940	0.08395
3	2	27.33830	-0.03356	27.41786	-0.03189	3	2	9.45544	-0.11622
4	2	21.63680	0.13085	20.87506	0.15289	4	2	6.86205	-0.18811
5	3	11.70368	-0.15333	10.95340	-0.20048	5	3	3.35230	0.54265
6	3	7.71895	-0.04224	7.31714	-0.05423	6	3	2.093175	0.55020
7	4	3.79376	0.41432	3.92519	0.49292	3p			
8	4	1.95931	0.69833	2.15217	0.61875	1	2	13.62079	-0.04475
3d						2	2	6.90531	-0.14977
1	3	12.84005	0.44729	12.67158	0.42120	3	3	3.17994	0.26788
2	3	5.22561	0.69683	5.43072	0.70658	4	3	1.72685	0.80384

Finally, for the sake of computational efficiency, the atomic densities and pair interactions are cut off at a distance R_c. That is, both the effective charge, Z(r), and the atomic electron density ρ(r) are set to zero beyond R_c, and within R_c a constant is added so that the functions go to zero continuously at the cutoff distance. The cuts off R_c for the different metals that are listed in Table 3.1 [Foiles 1992].

In the above assumptions, there are three adjustable parameters: α, β and N_s, needed to determine the pair potential, atomic electron density, and embedding function for each material. These have been determined for the elements Cu, Ni and Al so as to yield the elastic constants and vacancy-formation energy for each material. Note that due to the definition of the embedding function in terms of the equation of the state of the pure materials, the equilibrium lattice constant, sublimation energy, bulk modulus are guaranteed to be correct for the pure materials. The detailed fitting processes for EAM are described in the Appendix.

The parameters derived from the fitting to define the pair interactions and electron are given in Table 3.1. The properties used in the fitting process are listed in Table 3.3. The resulting embedding functions F(ρ) and embedding energies E as a function of background electron density ρ for Cu, Ni and Al are shown in Figures 3.1 and 3.2. The effective pair interaction as a function of distance r for Cu, Ni and Al at room temperature calculated form above equations are presented in Figures 3.3 and 3.4.

The calculated values for elastic constants and vacancy-formation energy of pure metal are compared with the experimental values to which they were fitted in Table 3.3. In general, the agreement between the fitted and experimental data is quite good. The poorest agreement is for shear modulus C_{44} of Al. Note, however, that this work is primarily concerned with Ni_3Al and, as will be shown below, the elastic constants of that alloy are reproduced quite well. The vacancy-formation energies accord well with the experimental estimates. The typical difference is approximately 0.1 eV and is in no case larger than 0.2 eV.

The elastic properties of the alloy are important to the mechanical behavior of the materials.

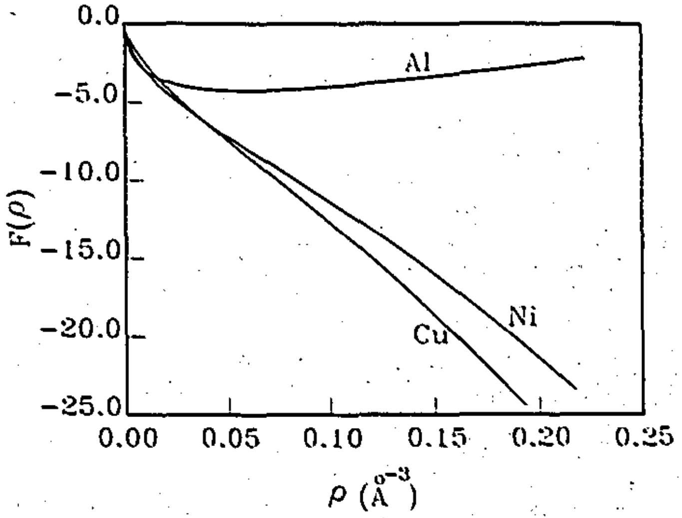

Figure 3.1 Embedding functions F(ρ) as a function of background electron density ρ for Cu, Ni and Al.

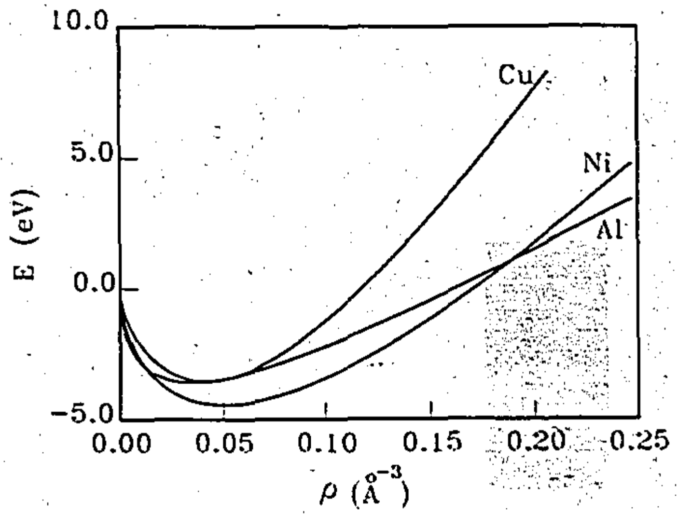

Figure 3.2 Embedding energies E of Cu, Ni and Al as a function of background electron density ρ.

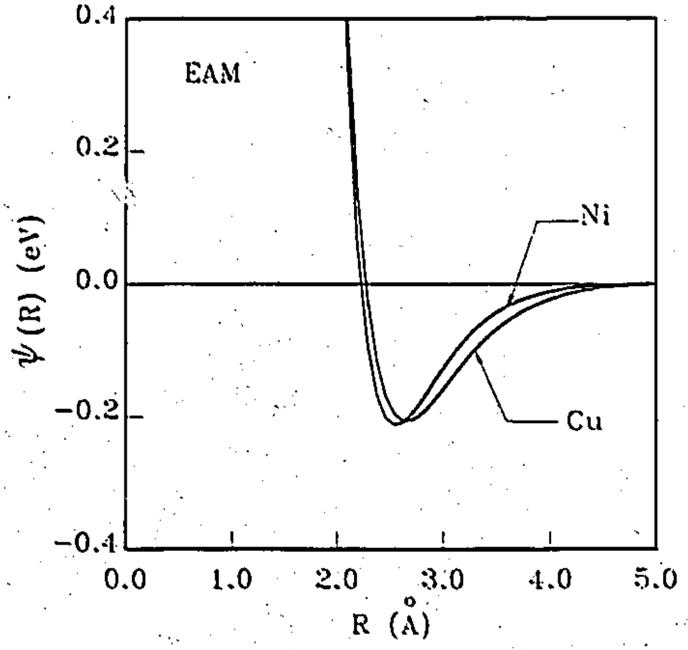

Figure 3.3 Effective pair potential for Cu and Ni calculated using EAM functions.

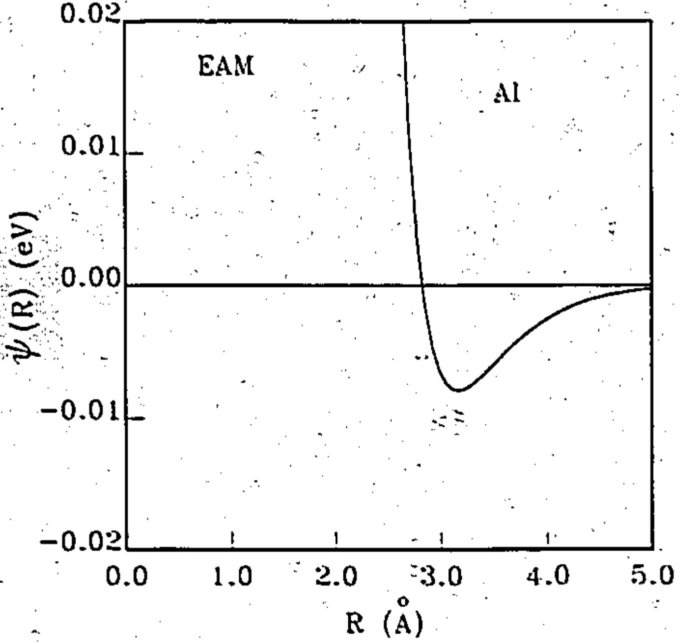

Figure 3.4 Effective pair potential for Al calculated using EAM functions.

Therefore, comparison of the elastic constants computed from EAM with the experimental values is a crucial test of the EAM functions used here and a good indicator of their predictive value. We have thus calculated the elastic constants of Ni$_3$Al which are also listed in Table 3.3. The agreement between the calculated elastic constants and experimental values is quite good and again gives confidence in the reliability of the EAM functions. We have also calculated the equilibrium lattice constants, sublimation and vacancy-formation energy of Ni$_3$Al which also agree quite well with the experimental data.

Table 3.3 Calculation of values and experimental properties ✻ for Cu, Ni, Al, and Ni$_3$Al used to determine the EAM functions: equilibrium lattice constants a_0, sublimation energy E_{sub}, bulk modulus B, elastic constants C_{11}, C_{12}, C_{44}, and vacancy-formation energy E_v^f.

	Cu		Ni		Al		Ni$_3$Al	
	Exp.	Cal.	Exp.	Cal.	Exp.	Cal.	Exp.	Cal.
a_0 (Å)	3.615[a]	3.615	3.524[a]	3.524	4.05[a]	4.05	3.57[h]	3.552
E_{sub} (eV)	3.54[b]	3.54	4.45[b]	4.45	3.58[f]	3.58	4.57[i]	4.488
B (10^{12} ergs/cm^3)	1.383[c]	1.383	1.804[c]	1.804	0.813[g]	0.813	1.752[j]	1.786
C_{11} (10^{12} ergs/cm^3)	1.70[c]	1.674	2.465[c]	2.403	1.12[g]	1.046	2.302[j]	2.421
C_{12} (10^{12} ergs/cm^3)	1.225[c]	1.238	1.473[c]	1.505	0.66[g]	0.697	1.493[j]	1.469
C_{44} (10^{12} ergs/cm^3)	0.758[c]	0.761	1.247[c]	1.268	0.28[g]	0.474	1.316[j]	1.302
E_v^f (eV)	1.3[d]	1.27	1.6[e]	1.58	0.7[d]	0.66	1.6[k]	1.58(Ni) 1.74(Al)

✻ Experimental data are obtained from the following references: [[a] Ashcroft et al. 1976, [b] Smith 1976, [c] Simmons et al. 1971, [d] Balluffi 1978, [e] Wycisk et al. 1978, [f] Fuchs 1936, [g] Englert et al. 1970, [h] Hansen 1958, [i] Hultgren et al. 1973, [j] Kayser et al. 1981, Foiles et al. 1987, [k] Wang et al. 1984].

3.2. Border Conditions

Computer simulations at the atomistic level are usually performed on a small number of atoms. The size of a system is limited by the available storage on the host computer, and, more crucially, by the speed of execution of the program. The time taken for a double loop used to evaluate the forces or potential energy is proportional to the square of the total number of atoms. Because the force/energy loop almost inevitably dictates the overall speed, smaller systems will always be less expensive [Allen and Tildesley 1991].

By its very nature, a grain boundary system is composed of two coupled regions, the grain boundary core and the surrounding bulk regions. It is an inherent difficulty in atomistic modeling to formulate proper border conditions so that (i) the size of the simulation cell can be kept to a minimum without allowing the grain boundary core to be perturbed artificially by the action of the cell borders, and (ii) the response of the bulk surroundings to grain boundary behavior is treated realistically. In simulation studies of grain boundaries, bicrystal models are used in which a planar interface, infinite in extent in two dimensions, is represented by a finite simulation cell with border conditions which are periodic in the two directions along the interface (the x- and y-borders). This is the proper representation of a coherent bicrystalline interface in which the atomic configuration is strictly periodic along the direction parallel to the plane of the interface [Lutsko et al. 1988, 1989].

For an isolated interface, one which is embedded in two semi-infinite bulk ideal crystals, two-dimensionally periodic border conditions in the two directions parallel to the interface are clearly appropriate [Lutsko et al 1988]. This embedding is accomplished by surrounding the grain boundary core, denoted as Simulation BOX in Figure 3.5, with two semi-infinite bulk ideal crystals, denoted as Crystals I and II. With the same two-dimensionally periodic border conditions applied in the directions x and y to both Simulation BOX and Crystals I, II, the system has no free surfaces. When thermal motions are considered in the calculation, the

Simulation BOX and Crystals I, II treatment together with two-dimensionally periodic border conditions is still appropriate.

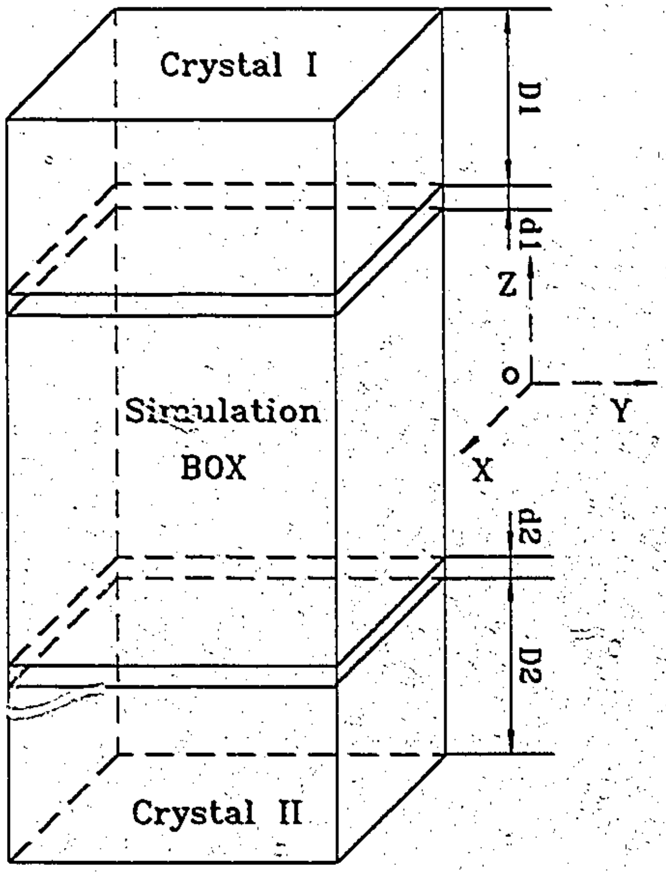

Figure 3.5 Schematic diagram of the grain boundary simulation method.

In order to handle periodic border conditions, when a particle crosses one of the borders, one usually switches attention to the image particle entering the border, by simply adding the box length to, or subtracting box length from the appropriate coordinate. One simple way to do the computer code [Allen and Tildesley 1991] for two-dimensionally border conditions in FORTRAN is to use arithmetic functions to calculate the correct number of box lengths to be added or subtracted:

$$\begin{aligned} RX(I) &= RX(I) - BOXLX * ANINT(RX(I) / BOXLX) \\ RY(I) &= RY(I) - BOXLY * ANINT(RY(I) / BOXLY) \end{aligned} \qquad (3.8)$$

where the RX(I) and RY(I) are the x and y coordinates of I atom, the BOXLX and BOXLY are the box length in x and y dimensions. The function ANINT(X) returns the nearest integer to X, converting the result back to type REAL. The minimum image convention can be coded in the same way as the periodic border adjustments.

One of the major limitations on the use of periodic border conditions is that the periodic vectors cannot be updated implicitly as a byproduct of the atomic motion. Due to the periodicity at the borders, there can be no net force exerted which would tend to modify the overall size or shape of the cell. Every force felt at the border is countered by an equal and opposite force from the neighboring cell. The end result is that the borders experience no acceleration and are therefore immobile. Because the borders are locked by opposing forces, there exists the possibility that unwanted, if not unreasonable stress will be developed within the computational cell. To alleviate this problem, Daw et al. [1985] have employed a scheme by which the borders are made dynamic and are adjusted specifically as to equate the stress state of the cell with a given state. The borders are made to move in accordance with a 'force' proportional to the difference between the actual stress observed in the cell and the stress being 'applied' there. To apply this displacement, both the border vectors and the atom positions are modified by a strain tensor on every step. The strain is proportional to the stress tensor components and the time step size as follows:

$$\varepsilon_{ii} = \frac{\sigma_{ii} \, (\Delta t)^2}{2 \, m^i_b} \qquad (i = x, y) \qquad (3.9)$$

where ε_{ii} is the iith component of the boundary strain, σ_{ii} is the iith component of the stress tensor, Δt is the time step length and m^i_b is a "border mass". (Typically, m^i_b is about 10 particle masses) [Lutsko et al. 1988].

Unlike periodic border conditions, and in contrast to the condition of a fixed z-border, the method for treating the z-borders at finite temperatures in a less-constraining manner accommodates dimensional changes normal to the interface as well as translational motions parallel to the interface plane. This method also makes use of the Simulation BOX and Crystal I, II configuration shown in Figure 3.5, where in the Simulation BOX the atoms are treated explicitly, and Crystal I, II consists of two semi-infinite rigid blocks of atoms held fixed at their ideal-crystal positions which are changed only when the lattice constant is changed, for example, when the temperature is changed. The novel feature is that the rigid blocks are allowed to move by translations parallel to the interface plane, such motions being determined by the force exerted on the blocks across the Simulation BOX and Crystals I, II borders, and by the pressure exerted on the blocks by the Simulation Box, as well as by the applied stress on the blocks. Thus, the z movement is treated in the usual manner using the Parrinello-Rahman method, while each block translates in the x-y plane as a single particle with effective mass. This border is also made dynamic and is adjusted specifically as to equate the stress state in which the stress tensor is calculated with Simulation Box and Crystal I, II, plus the applied external stress along the z-direction. Thus, the strain in z-direction is given by [Daw and Foils 1985, Lutsko 1988]:

$$\varepsilon_{zz} = \frac{(\sigma_{zz} + \sigma_a)(\Delta t)^2}{2\, m^z{}_b} \tag{3.10}$$

where σ_a is the applied external stress along the z-direction. If there is no applied external stress along the z-direction, an equilibrium state of interface can be approached, otherwise the fracture behavior of interface can be simulated.

Applications of the border conditions to grain boundaries at low and high temperatures have given satisfactory results.

3.3. Initial Geometry of Grain Boundary

In symmetrical grain boundaries, by definition, the grain boundary plane normal represents the same set of crystallographically equivalent lattice planes in the two halves of the bicrystal. This condition reduces the number of the macroscopic degree of freedom from five to only three. Let us now consider what type of symmetrical grain boundary can be generated by systematically varying the three degrees of freedom in the rotation axis **n** and misorientation θ. In cubic crystals the rotation axis **n** may be given in terms of the Miller indices, <hkl>, according to [Wolf 1992].

$$n = (h^2 + k^2 + l^2)^{-\frac{1}{2}} \begin{pmatrix} h \\ k \\ l \end{pmatrix} \tag{3.11}$$

and all relevant geometrical parameters may be expressed in terms of the h, k and l associated with a given plane. With <hkl> thus fixed, the only degree of freedom left is the rotation orientation θ. Rotation by an arbitrary value of θ generally produces a grain boundary with a much larger unit cell area. For the special angles of θ = 180°/n + k•360/n (k=1, 2, ...): the stacking sequence on one side of the grain boundary plane is inverted with respect to the other, and the symmetrical grain boundary on the <hkl> plane is obtained. For simplicity, a three-dimensional CSL is generated by a rotation vector $\mathbf{k}_r$ = <xyz> about <hkl> plane with the misorientation θ given by [Wolf 1992]:

$$\theta = 2 \tan^{-1} \left(\frac{x}{y} (h^2 + k^2 + l^2)^{\frac{1}{2}} \right), \tag{3.12}$$

and the parameter Σ given by:

$$\Sigma = x^2 + (h^2 + k^2 + l^2) y^2 \tag{3.13}$$

If the equation 3.13 yields an even number, it must be divided by two, and repeats until an odd number results.

Table 3.4 provides a list of configuration of symmetric twist grain boundary for <001>, <011> and <111> rotation axes. k_r is the rotation vector and θ is the misorientation of grain boundary. Note that symmetric twist grain boundaries with that same Σ of about one rotation axis have the same configuration, even if their misorientations are different. As we indicated earlier, a symmetric grain boundary can be described using only rotation axis and misorientation (or rotation vector). However, in Table 3.4 a full description which is used in our simulation is given. The total number of atoms in the Simulation Box is presented by N_{gb}, and the atoms in both the Crystals I and II boxes are presented by N_b. Therefore the total number of atoms in our system is (N_{gb}+N_b). A detailed arrangement in the x, y, and z directions is given by n_x, n_y, and n_z which represent the number of layers in each direction. Thus, N_{gb}= n_x*n_y*n_z, and each layer along the z direction have n_x*n_y atoms. For Crystal I & II n_{zB} presents the number of layers along the z direction, and thus we obtain N_B= n_x*n_y*n_{zB}. This table shows that the total number of atoms in our system is about 2400 - 4700.

The compound Ni_3Al has a Ll_2 crystal structure, a derivative of the face-centered cubic (fcc) crystal structure. Figure 3.6 illustrates the crystal structure, showing the ordered arrangements of atoms for Ni_3Al compound, Al atoms going to the cubic corners and Ni atoms going to the face centers [Hansen 1958]. Therefore, symmetric grain boundaries in Ni_3Al have different grain boundary compositions which depend on the rotation axis. The grain boundary composition can be described by the Ni percentage of the first layer on each side of the grain boundary core, namely: 50/100 or 75/75 grain boundaries. The 50/100 grain boundary indicates one layer NiAl and one layer Ni on each side of grain boundary core, and the 75/75 grain boundary indicates both layers on each side of the grain boundary core are Ni_3Al. There are other possible

Table 3.4 Configurations of symmetric twist grain boundary. Here $\mathbf{k}_r$ is the rotation vector and $\theta°$ is the misorientation; N_{gb} are the atoms in the Simulation Box and $2N_B$ are the atoms in the Crystals I & II boxes; $(N_{gb}+2N_B)$ are the total number of atoms in system. n_x, n_y, n_z are the layers in the x, y, z directions $(n_x*n_y*n_z=N_{gb})$; $2n_{zB}$ are the layers for static atoms in the z direction $(n_x*n_y*n_{zB}=N_B)$; C (Ni_3Al) represents the structure of grain boundary core in Ni_3Al. The 50/100 grain boundary is one layer NiAl and one layer Ni, and the 75/75 grain boundary is arranged by the same kind of layer Ni_3Al.

Axis	Σ	k_r	θ°	N_{gb}	$2N_B$	n_x	n_y	n_z	$2n_{zB}$	C (Ni_3Al)
<001>	5	<130>	36.87	2340	900	30	3	26	10	50/100
		<120>	53.13							
<001>	13a	<150>	22.62	2704	1040	52	2	26	10	50/100
		<230>	67.38							
<001>	17a	<140>	28.07	1768	680	34	2	26	10	50/100
		<350>	61.93							
<011>	3	<120>	70.53	2496	960	24	4	26	10	50/100
		<110>	109.47							
<011>	9	<140>	38.94	2808	780	26	3	26	10	50/100
		<210>	141.06							
<011>	11	<130>	50.48	3432	1320	33	4	26	10	50/100
		<320>	129.53							
<011>	17b	<230>	86.63	1768	680	34	2	26	10	50/100
		<340>	93.37							
<011>	19a	<160>	26.53	1976	760	38	2	26	10	50/100
		<310>	153.47							
<111>	3	<130>	60.0	2496	960	12	8	26	10	75/75
		<100>	180.0							
<111>	7	<150>	38.21	2912	1120	56	2	26	10	75/75
		<120>	81.79							
		<310>	158.21							
<111>	13b	<170>	27.80	2704	1040	52	2	26	10	75/75
		<350>	92.20							
		<210>	147.80							
<111>	19b	<140>	46.83	1976	760	76	1	26	10	75/75
		<370>	73.17							
		<510>	166.83							

compositions for Ni_3Al, however, in the project, we consider only 50/100 and 75/75 grain boundaries.

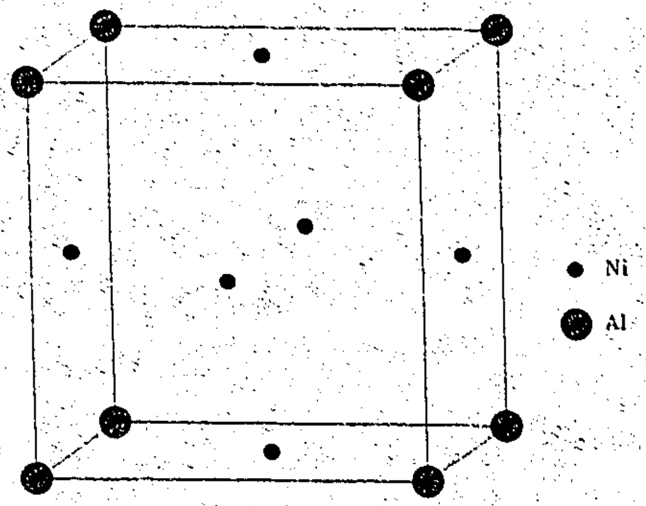

Figure 3.6 Ordered crystal structure of Ni_3Al.

Table 3.5 gives a list of configurations of symmetric tilt grain boundary for <001> and <011> rotation axes. Note that for symmetric tilt grain boundaries with the same Σ value of about one rotation axis the configurations are different when their misorientations are different.

From Table 3.4 and 3.5 we can now see that the total number of low Σ grain boundaries which are investigated in this project is 28.

Σ3 Twin Boundary

Σ3 twin boundary is a particularly special grain boundary in polycrystalline materials because the interfacial region in a Σ3 twin boundary has a structure identical to that of the ideal lattice. The grain boundaries preferentially align themselves with a common {111} plane of both crystals to form what is called a coherent twin boundary which coherently inverts the regular stacking sequence of close-packed {111} layers at the twin boundary plane. Since the nearest and

Table 3.5 Configurations of symmetric tilt grain boundary. Here k_r is the rotation vector and $\theta°$ is the misorientation; N_{gb} are the atoms in the Simulation Box and $2N_B$ are the atoms in the Crystals I & II boxes; $(N_{gb}+2N_B)$ are the total number of atoms in system. n_x, n_y, n_z are the layers in the x, y, z directions $(n_x*n_y*n_z=N_{gb})$; $2n_{zB}$ are the layers for static atoms in the z direction $(n_x*n_y*n_{zB}=N_B)$; C (Ni_3Al) represents the structure of grain boundary core in Ni_3Al. The 50/100 grain boundary is one layer NiAl and one layer Ni, and the 75/75 grain boundary is arranged by the same kind of layer Ni_3Al.

Axis	Σ	k_r	$\theta°$	N_{gb}	$2N_B$	n_x	n_y	n_z	$2n_{zB}$	C (Ni_3Al)
<001>	5	<130>	36.87	2448	960	6	8	51	20	50/100
<001>	5	<120>	53.13	2616	960	6	4	109	40	50/100
<001>	13a	<150>	22.62	2616	960	6	4	109	40	50/100
<001>	13a	<230>	67.38	2616	960	6	4	109	40	50/100
<001>	17a	<140>	28.07	2616	960	6	4	109	40	50/100
<001>	17a	<350>	61.93	2616	960	6	4	109	40	50/100
<011>	3	<120>	70.53	2592	960	6	16	27	10	75/75
<011>	3	<110>	109.47	2616	960	6	4	109	40	50/100
<011>	9	<140>	38.94	2616	960	6	4	109	40	50/100
<011>	9	<210>	141.06	2616	960	6	4	109	40	50/100
<011>	11	<130>	50.48	2640	960	6	8	55	20	75/75
<011>	11	<320>	129.52	2682	900	6	3	149	50	50/100
<011>	17b	<230>	86.63	2616	960	6	4	109	40	50/100
<011>	17b	<340>	93.37	2604	960	6	2	217	80	50/100
<011>	19a	<160>	26.53	2604	960	6	2	217	80	50/100
<011>	19a	<310>	153.47	2832	960	6	8	59	20	50/100

next-nearest-neighbor coordination is unchanged, the energy of a coherent twin boundary is very small. As a consequence, coherent twin boundaries are virtually straight and relatively immobile. Σ3 grain boundaries that are not parallel to a {111} plane in both adjacent crystals are termed incoherent Σ3 twin boundaries, which occur, for example, where a twin lamella ends within a grain, or at steps in a coherent twin boundary. A special case is where the boundary plane coincides with a common {211} plane of both crystals, which lays normally to the plane of the coherent twin boundary, which is referred to as the symmetric incoherent twin boundary.

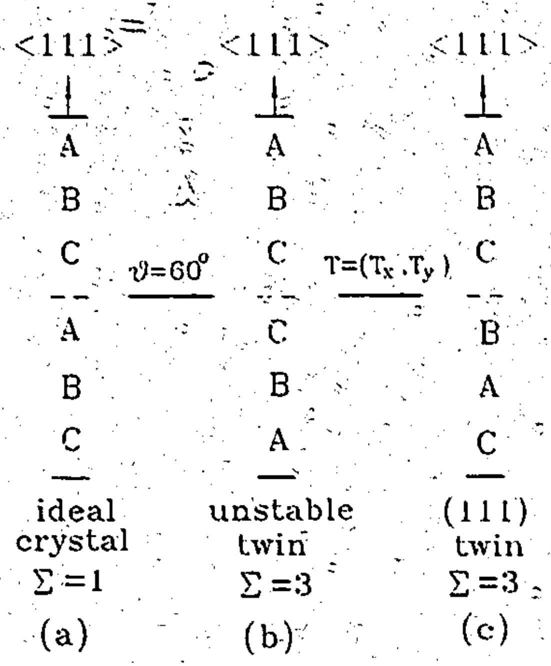

Figure 3.7 Generation of the (111) twin boundary in fcc as a 60^{0} twist boundary. (a) Three-plane ideal-crystal stacking of (111) planes; (b) a 60^{0} twist rotation of the lower half of the ideal crystal leads to an inversion of the stacking sequence; (c) translation parallel to the grain boundary plane (such that C → B and hence B → A and A → C) avoids the energetically unfavorable configuration in (b) by the familiar stacking in which C is a mirror plane [Wolf 1992].

Figure 3.7 shows the generation of the (111) twin boundary in fcc as a 60° twist boundary. For (111) planes, the perfect crystal in Figure 3.7(a) is inverted into the symmetric tilt grain boundary in Figure 3.7(b) by a 60° twist rotation of the lower half of the ideal crystal, which is an unstable twin grain boundary. A translation parallel to the grain boundary plane such that C–B (and, therefore, B–A and A–C) yield the familiar coherent twin configuration in Fig. 3.7(c).

3.4. Determination of Pressure and Stress Tensor

The pressure of a system can be obtained from the general expression [Hansen and McDonald 1976]:

$$P = n k_B T - \left\langle \frac{\partial E}{\partial V} \right\rangle \tag{3.14}$$

In this expression, n is the total atomic number density, k_B is the Boltzmann constant, T is the absolute temperature, E is the internal energy of the system, V is the volume, and the derivative refers to the change in energy due to a uniform expansion of the system. The angular brackets refer to an average computed at a constant number of particles and temperature. For EAM this expression yields the following results for pressure [Foiles 1985]:

$$P = n k_B T - \frac{n}{3N} \left\langle \sum_{i,j,i \neq j} [\, F_i'(\rho_i)\, \rho_j'(r_{ij}) + \frac{1}{2} \phi'(r_{ij}) \,]\, r_{ij} \right\rangle \tag{3.15}$$

where N is the total number of atoms, r_{ij} is the separation of atoms i and j. This choice for the pressure of a system does not make the actual calculations with this method significantly more computer intensive than the use of pair-potential models.

The internal stress tensor can be calculated by the expression [Ray and Rahman 1984]:

$$P_{ij} = \frac{1}{V}\left[\sum_{a}\frac{p_{ai}\,p_{aj}}{m_a} - \sum_{a<b}\chi_{ab}\,x_{abi}\,x_{abj}\right] \tag{3.16}$$

where p_a is the momentum components, m_a is the mass of a particle, x_{ab} is the vector joining a and b of length r_{ab}, and V is the volume containing the N particles, χ_{ab} is a scalar quantity depending on the distance r_{ab} defined as [Ray and Rahman 1984]:

$$\chi_{ab} = \frac{1}{r_{ab}}\frac{\partial\psi(r)}{\partial r_{ab}} \tag{3.17}$$

where $\psi(r)$ is the effective pair potential (Eq. 3.7). The first term in Eq. 3.16 yields the kinetic component of the stress tensor and the second term represents the force contribution to the stress tensor. This expression gives stress as the strain derivative of total energy.

3.5. Grain Boundary Structure and Energy

The central question in the study of grain boundary phenomena concerns the correlation between structure (geometrical and chemical) and the related properties of interface materials [Yip and Wolf 1989]. The unraveling of this correlation for different properties and the understanding of the underlying causes present not only a challenge but also an opportunity for atomistic simulations, particularly in view of the enormous experimental difficulties in measuring local properties near grain boundaries. In recent years, lattice-statics relaxation methods have been used rather successfully to unravel the correlation between the geometry and energy of grain boundary energy at zero temperature.

The comprehension of the relationship between the structure and energy of grain boundaries has been a subject of considerable interest for the past two decades [Yip and Wolf 1989]. Until recently, an important problem with the simulations of grain boundaries in metals had to do with the fact that the volume expansion at the grain boundary, arising from the destruction of perfect stacking at the grain boundary, cannot be satisfactorily taken into account by using pair potentials. This volume expansion gives an anisotropy and local-volume dependence in the strength of the interaction between atoms in or near the grain boundary region to many-body effects near the grain boundary. With the recent availability of volume dependent type many-body potentials, such as embedded-atom-method (EAM), it is now possible to incorporate these local-volume effects in a more satisfactory manner at least in a semi-empirical way, and thus better take into account the inhomogeneity of grain boundary systems. The grain boundary free volume at the grain boundary can then be predicted with some degree of reliability.

3.5.1. Grain Boundary Free Volume

Grain boundary free volume (or excess volume or the grain boundary expansion) is simply defined as the difference between the volume of a bicrystal and that of a single crystal containing the same number of atoms [Mehta and Smith 1993]. Thermodynamically, the free volume of a grain boundary can be defined as a parameter expressing the change in volume of a polycrystalline material with grain boundary area (A) at constant temperature, pressure, number of atoms, n, and composition, x. It is convenient to express grain boundary free volume as the extra volume per unit area of the grain boundary plane, associated with a unit cell spanning the boundary. Hence, grain boundary free volume has the linear dimensions [Mehta and Smith 1993]:

$$V_f = \left. \frac{\partial V}{\partial A} \right|_{T,P,n,x} \tag{3.18}$$

To facilitate comparisons between different materials, the free volume may be expressed in units of lattice parameter. Thus,

$$V_f = \frac{\delta a}{a} \tag{3.19}$$

where δa is the rigid body translation measured parallel to the grain boundary plane normal, and "a" is the lattice parameter.

Another measure of the grain boundary expansion is the relative displacement of the two atomic planes close to the grain boundary. Therefore, for a symmetric tilt boundary with indices (hkl), the excess volume can be defined in terms of the interplanar spacings of the grain boundary planes as:

$$V_f = \frac{d - d_{hkl}}{a} \tag{3.20}$$

where d is the interplanar spacing measured between the planes at the grain boundary, and d_{hkl} is the spacing between two parallel (hkl) planes in the grain interior. According to recent computer calculations, however, the grain boundary expansion need not be confined to the boundary plane. Instead, it may be distributed on either side of the grain boundary plane, and decay in an oscillatory fashion within each grain. In such a case, the amplitude of oscillation is at a maximum at the grain boundary plane, and decays exponentially with its distance from the grain boundary.

Frost et al. [1982] in their hard sphere model for symmetrical grain boundaries in fcc crystals, defined grain boundary free volume by considering the number of missing atoms per atom in the grain boundary plane. The grain boundary free volume V_f can subsequently be expressed as:

$$V_f = \frac{V^*}{A^*} = \frac{V - N\Omega}{A\Omega^{1/3}} \tag{3.21}$$

Here V^* is the extra volume of a unit cell associated with one repeat unit at the grain boundary, normalized to the atomic volume in the grain interior. Hence,

$$V^* = \frac{V - N\Omega}{\Omega} \tag{3.22}$$

and A^* is the normalized area per lattice point in the grain boundary plane.

$$A^* = \frac{A}{\Omega^{2/3}} \tag{3.23}$$

In the above expressions, V is the volume of a unit cell formed across the grain boundary planes and contains N atoms, A is the area of the repeat unit at the boundary, and Ω is the atomic volume. It is straightforward to obtain the atomic volume Ω, and the area per lattice point in the grain boundary plane, in terms of lattice parameter if the structure is known. It is apparent that the free volume as defined in equation 3.17 is a dimensionless parameter. This expression has been used through out our calculations for grain boundary free volume. Similar expressions can be deduced for other structures.

3.5.2. Grain Boundary Energy

The grain boundary energy, E_{GB} can be defined as [Wolf 1988]:

$$E_{GB} = \frac{\sum_{i=1}^{N} U_i - NU_0}{A} \tag{3.24}$$

where U_i is the energy of atom i in a unit cell formed across the grain boundary plane which contains N atoms, U_0 is the energy of an atom in the perfect crystal, and A is the area of the repeat unit at boundary.

3.5.3. Static Energy Minimization

Figure 3.8 presents the structure of the program code in terms of the information data flow involved in performing a static energy minimization with a constant stress at the borders. The energy minimization process is accomplished iteratively with two separate operations existing within the main iterative loop. The first process is an iterative attempt to reduce total excess stress on the borders by adjusting the period vectors along the x and y directions and the cell length in the z direction. Once convergence is obtained within this loop, the second process is used to minimize the energy of the system by moving atoms individually, subject to the interatomic force on them, with fixed border conditions. Convergence is obtained once both loops are satisfied simultaneously.

3.5.4. Grain Boundary Structure Relaxation

By applying the steepest descent relaxation method with a constant stress at the borders, energy minimization was performed on the grain boundary structure model using dynamic borders. In this relaxation method, the rigid Crystal I and II blocks are allowed to slide parallel to the grain boundary plane, at the same time as periodic borders x and y are allowed to move according the internal stress tensor along these directions. The minimization was halted once the largest change in any atoms position had been reduced to below 10^{-5} r.u. (reduced unit) on any two successive steps. The constant stress calculation which controls border conditions was terminated once each of the 9 components of the excess stress tensor had been reduced to less than 1 MPa.

By applying this relaxation method, the grain boundary structure, as well as its optimum bicrystal volume and minimum energy, can be determined using equation 3.21 and 3.24.

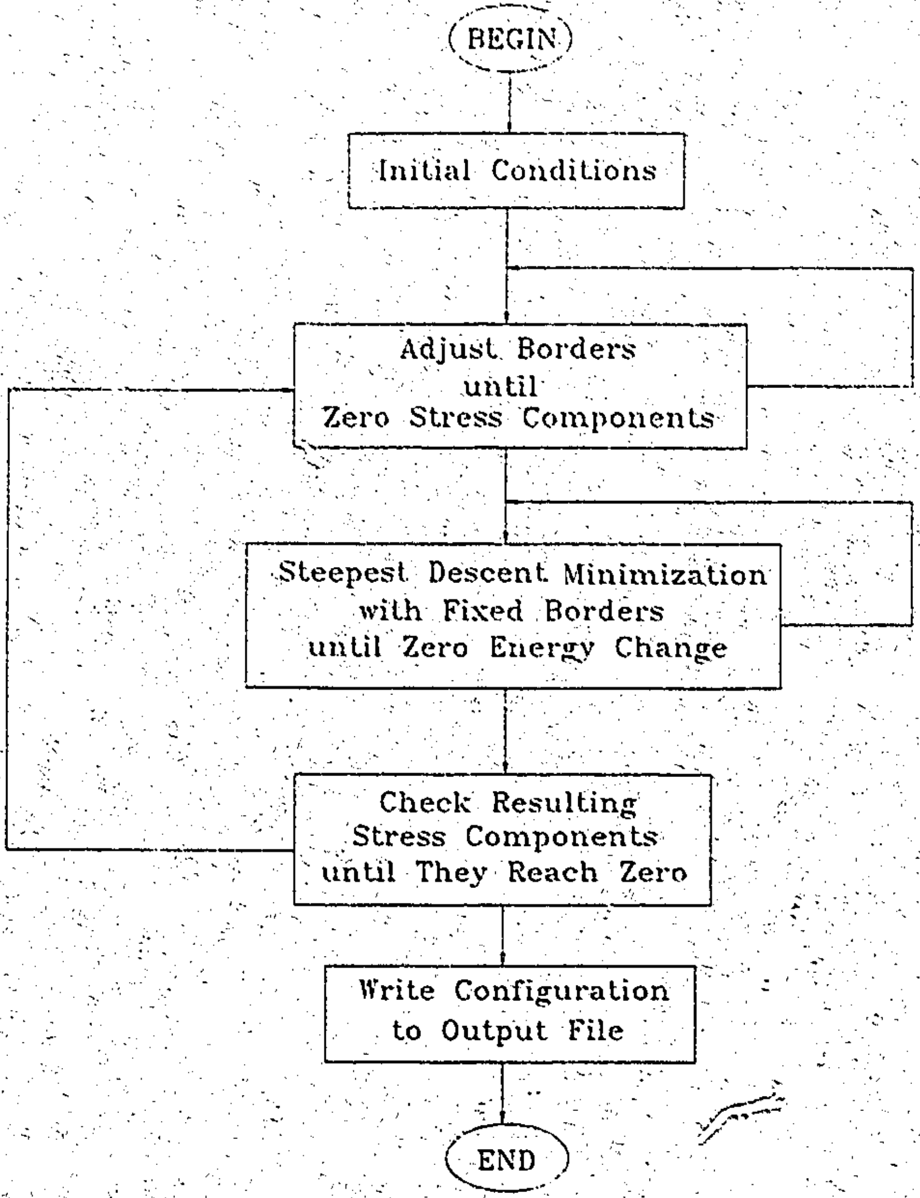

Figure 3.8 Data flow of steepest descent energy minimization with constant stress.

3.6. Molecular Dynamics Simulation

Having reviewed the general concept of the molecular dynamics simulation in the previous chapter, now we undertake to describe the procedure in more detail, and the manner in which the concepts are implemented into a functional computer simulation.

3.6.1. Basic Procedure

The goal of the molecular dynamics simulation is to describe the positions of atoms within a region of solid or liquid materials. The method may be used to track the time dependent motion of each of the atoms throughout the course of a physical process such as phase transformation or crack propagation. Once the positions are known, the method may be employed to compute energy levels, forces, and stresses throughout the region of interest.

The core of the MD method is the determination of atomic positions from the potential energy equation 2.4. This relation is used to compute the force placed on each atom, i, as $\mathbf{F}_i=-\partial U(r)/\partial \mathbf{r}_i$, the gradient in potential energy with respect to the position of the atom, $\mathbf{r}_i$. The forces may then be used to determine the equilibrium structure as the collection of $\mathbf{r}_i$ that yield zero net force on each atom, or to track the time evolution of the positions of each atom by integrating the accelerations, $\mathbf{a}_i=\mathbf{F}_i/m_i$ forward in time.

Once the atomic positions have been determined, the other variables of interest may be computed. Potential energy for each atom is determined from Eq. 2.4, and the kinetic energy of each particle is computed as $\frac{1}{2} m_i v_i^2$, where m_i is the mass and v_i is the velocity of atom i. The other quantities of interest, such as the local stress tensor, pressure and structure factor, may also be computed.

3.6.2. Implementation

In molecular dynamic simulations, one seeks to investigate the time dependent evolution of atomistic configurations and to study time varying phenomena. To do this, the position of each atom is integrated forward in time subject to Newtonian force laws and the prevailing interatomic potentials (Eq. 2.7 or 2.8). The integration is carried out numerically, with each particle being moved a small distance within each of a series of short time steps. Several techniques such as Central-difference, Euler-Cauchy and simple Predictor-Corrector methods are available to perform the integration. One of the more popular techniques is the Nordsiek integration, which is the method selected by Daw, Baskes and Foiles at Sandia [1985].

Operationally, the method may be described as follows: Start with X(t) as an atom's position, and express the first five time derivatives (multiplied by the time step, Δt) as:

$$\begin{aligned} U_1 &= \frac{dX}{dt}\Delta t \\ U_2 &= \frac{1}{2}\frac{d^2X}{d^2t}\Delta t^2 \\ U_3 &= \frac{1}{6}\frac{d^3X}{d^3t}\Delta t^3 \\ U_4 &= \frac{1}{24}\frac{d^4X}{d^4t}\Delta t^4 \\ U_5 &= \frac{1}{120}\frac{d^5X}{d^5t}\Delta t^5 \end{aligned} \tag{3.25}$$

The predicted values for X and the U's at the end of the time step $(t+\Delta t)$ are:

$$\begin{aligned} X(t+\Delta t) &= X(t) + U_1(t) + U_2(t) + U_3(t) + U_4(t) + U_5(t) \\ U_1(t+\Delta t) &= U_1(t) + 2U_2(t) + 3U_3(t) + 4U_4(t) + 5U_5(t) \\ U_2(t+\Delta t) &= U_2(t) + 3U_3(t) + 6U_4(t) + 10U_5(t) \\ U_3(t+\Delta t) &= U_3(t) + 4U_4(t) + 10U_5(t) \\ U_4(t+\Delta t) &= U_4(t) + 5U_5(t) \\ U_5(t+\Delta t) &= U_5(t)\,. \end{aligned} \tag{3.26}$$

The predicted value of X is then used to evaluate the force at time (t+Δt) and a displacement function, χ, is used to correct the predictions of X and the U's.

$$\chi = \frac{1}{2}\,\frac{F}{m}\,(\Delta t)^2 - U_2(t + \Delta t)\,, \qquad (3.27)$$

where F is the force on the atom and m is its mass. The corrected values for X and derivatives are then expressed as:

$$\begin{aligned}
X^c(t+\Delta t) &= X(t+\Delta t) + C_0\chi\,, && (C_0 = 3/16)\\
U_1^c(t+\Delta t) &= U_1(t+\Delta t) + C_1\chi\,, && (C_1 = 251/360)\\
U_2^c(t+\Delta t) &= U_2(t+\Delta t) + C_2\chi\,, && (C_2 = 1)\\
U_3^c(t+\Delta t) &= U_3(t+\Delta t) + C_3\chi\,, && (C_3 = 11/18) \qquad (3.28)\\
U_4^c(t+\Delta t) &= U_4(t+\Delta t) + C_4\chi\,, && (C_4 = 1/6)\\
U_5^c(t+\Delta t) &= U_5(t+\Delta t) + C_5\chi\,, && (C_5 = 1/60)
\end{aligned}$$

3.6.3. Structure of Molecular Dynamics Code

Molecular dynamics simulations are performed by integrating the equation of motion for the atoms and borders over a preselected number of fixed length time steps. Figure 3.9 presents the data flow of a molecular dynamics simulation. Within each step, the particle positions are used to determine forces and the overall stress tensor. External forces may be applied once the atom-atom couples have been computed. The positions and velocities are then updated and the borders moved in preparation for the next time step.

3.6.4. Treatment of Temperature

It is necessary to be able to monitor and control the effective temperature of the computational system. The temperature of the system is measured in terms of the average kinetic

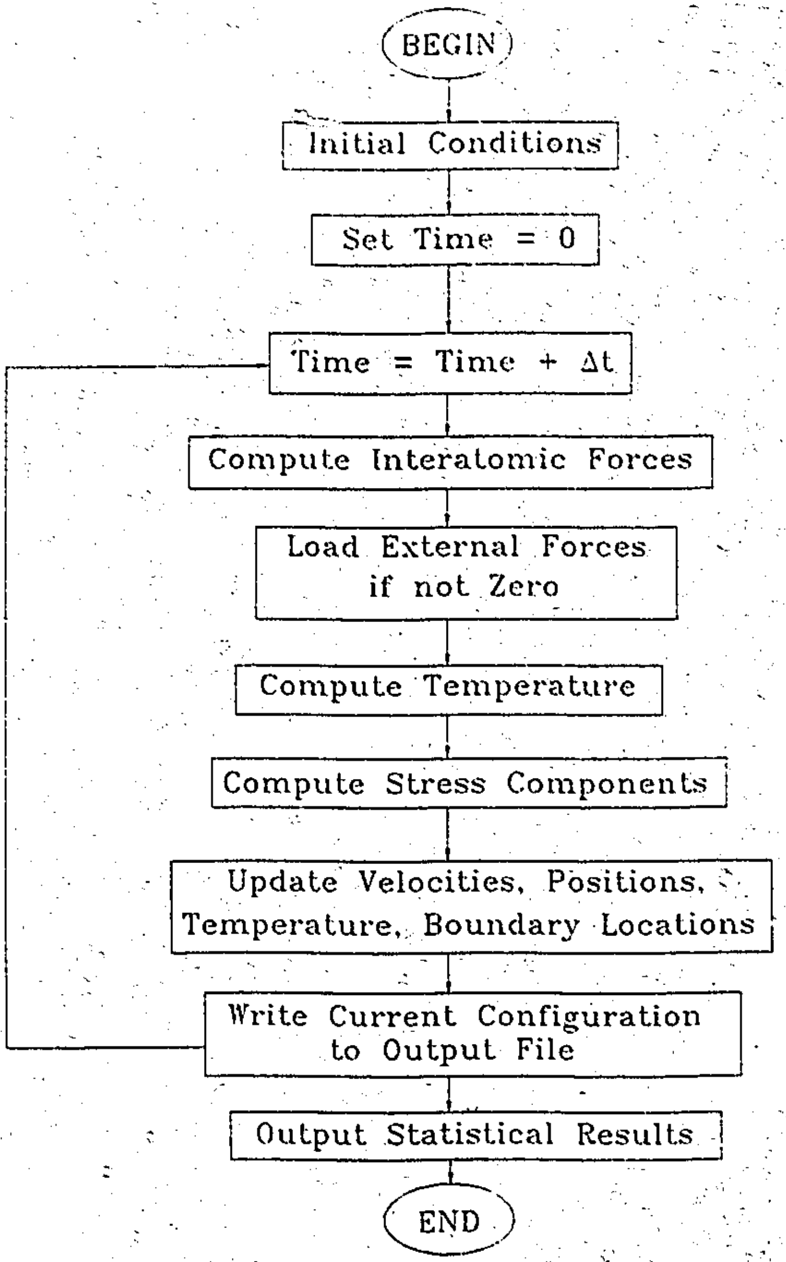

Figure 3.9 Data flow of molecular dynamics simulation.

energy of all the atoms:

$$T = \frac{2}{3\,k_B} E_{ke} = \frac{2}{3\,k_B N} \sum_{i=1}^{N} \frac{1}{2} m_i\, V_i^2\,, \tag{3.29}$$

where T is absolute temperature, E_{ke} is total kinetic energy, k_B is the Boltzman constant, and N is the total number of particles. This relation is sufficient for use in measuring temperature, but in order to control it, a mechanism is required by which energy can be added to or removed from the system in such a way as to influence the kinetic energy of the ensemble.

Two methods have been suggested to bring about this energy transfer. The first, and potentially more correct, is to add or subtract energy only through the borders by magnifying or damping the kinetic energy of the border atoms in accordance with a heat transfer law properly evaluated for the existing temperature difference. The larger the temperature difference, the greater the flux of heat into or out of the system will be as is expected for the actual system.

The second method is perhaps slightly less correct conceptually, but is simpler to implement and probably equal in accuracy over the range of simulations performed in most applications. In this method, kinetic energy is added or subtracted from atoms uniformly across the system with no regard to their spatial arrangement. In this case, heat transfer is treated as though it occurred through some radiative process in which the carrier waves were of such high frequency as to pass unattenuated through large lengths of the materials. The temperature equilibration model operates on an energy deficit/excess expressed in terms of the difference between the target and the actual temperature [Daw et al. 1985]:

$$\Delta E = E_0 - E_{cal} = \frac{3}{2} k_B T_0 - \frac{1}{N} \sum_{i=1}^{N} \frac{1}{2} m_i\, v_i^2 \tag{3.30}$$

where T_0 is desired temperature and T_{cal} is calculated temperature. This energy may be added to or removed from the system by applying a fictitious force, $\Delta F = \Delta E/dx = \Delta E/\tau v$, over a distance dx. Here dx is computed as the velocity, v, multiplied by an adjustable time constant, τ. The time constant is used to control the speed at which the energy deficit/excess is communicated into or out of the system. The actual expression for ΔF is written so that the calculated temperature is computed from the average particle velocity and the amount of force applied to any given atom is proportional to its own velocity. This scheme tends to preserve the shape of the initial velocity distribution. The force applied to atom i is given as [Daw et al. 1985]:

$$\Delta F_i = v_i \frac{\Delta E}{\tau v} \tag{3.31}$$

In the case of a single particle, it can easily be seen that this treatment leads to an exponential decay of energy excess or deficit in time. The time constant of the decay is related to the adjustable parameter τ.

The initial velocity distribution of the system is given as random distribution and then scaled to desired temperature.

3.6.5. Treatment of Time

The molecular dynamics simulation is intended to solve Newton equations of motion numerically for given system configuration, velocities, and other dynamic information at time t under the assumption of constant force, and then to obtain the system configuration, velocities etc. at a later time $t+\Delta t$, to a sufficient degree of accuracy, for a small time interval Δt. The equations are solved on a step-by-step basis. The choice of the time interval Δt will depend to some degree on the method of solution, however, Δt will be significantly smaller than the typical time taken for a particle to travel its own length. In the limit $\Delta t \to 0$ the solution is exact. Therefore, time unit is a very important variable for the molecular dynamics simulation. When the time interval Δt is too large, the numerical solution is far from the exact one expressed in the equations. When Δt is too small, however, it will cost much more computing time.

Considering the vibration of atoms, a reasonable time step is approximately $10^{-14}-10^{-16}$ seconds [Allen and Tildesley 1991]. In our simulation the time step is kept at 5.0×10^{-15} seconds, which is very good for most metals.

3.6.6. Treatment of External Stress

In order to conduct molecular dynamics simulations of fracture and other stress driven processes, it is necessary to be able to apply an external load to the computational system. In our model, the borders and the atoms within Crystals I and II are subjected to an external influence expressed in terms of a constant load, which means that an external force may be set to a constant value or varied as a function of time. The scheme for conducting stress experiments is to better approximate the true behavior of the atoms by tracking their motion in response to stress. In principal, this method might exactly duplicate the conditions of a laboratory experiment, but in actual practice, the stresses must be increased quite quickly in time to take a sample from equilibrium to fracture in a reasonable expenditure of computer time. Molecular dynamics simulations generally extend to tens of picoseconds, yielding results for a very fast stress-strain experiment.

Molecular dynamics simulations under stress were performed in order to demonstrate the behavior of a laboratory stress strain experiment conducted under a constant extension rate. The simulations were performed by assigning external forces to atoms at the borders and the static atoms within Crystals I & II in accordance with the desired external load. In these cases, periodicity was limited to two dimensions in order to create two free sides that could be used as grips. In this investigation, only pure tensile loads were used, applied along the non-periodic directions. Force, rather than extension is used as the control variable because it is simpler to deal with and imposes fewer artificial constraints on particle movement. The simulations were initiated at 300K and given 4000 steps without stress to allow temperature equilibration. After 4000 steps the external forces are engaged, and ramped linearly in time from zero until the sample fractures or the time limit is reached.

The actual propagation of cracks across individual lattice planes is expected to occur very quickly, and as a result the molecular dynamics method is very well suited to a simulation of the mechanisms and processes of fracture. In this investigation, the molecular dynamics method was selected in order to focus attention on the atomistic of the fracture processes and to study the direct influence of grain boundaries upon these processes. A key point in making molecular dynamics simulations under external stress is to select a force ramp rate low enough to minimize any shock wave effects that may result when the external load is increased faster than the rate at which the forces can be communicated to the interior of the materials. If the force is ramping too quickly, stress gradients will result, yielding a non-uniform stress state, and possibly erroneous information on properties such as fracture strength and elastic moduli. When the ramp rate is reduced, elastic waves have time to distribute the force throughout the material, resulting a uniform stress state that better matches the conditions in an actual experiment. In the present investigation, the ramp rate was taken as 1.9×10^{-5}eV/$Å^3$ per time step [Daw et al. 1985]. The rate was determined by comparing the stress rate with the speed of elastic waves within the crystal and was found through experimentation to be an upper limit on the value for which the results of simulations are insensitive to the exact ramp rate employed. As such, the rate is optimal for use in production simulations insensitive to this value, as most samples can be stressed to fracture within about 16,000 time steps.

3.7. Surface Energy

The fracture properties of polycrystalline materials are also known to be sensitive to microstructure and the properties of the surfaces of the exposed grain boundary. The surface energy is an important quantitative property of the free surface which can influence fracture toughness. The surface of the exposed grain boundary with high energy is unfavorable to fracture. The surface energy is known to depend on microstructure of the free surface, i.e., the surface normal, however, it does not depend on crystallographic orientation as much as on the grain boundary energy.

Free surfaces, characterized by only two degrees of freedom (namely those associated with the surface normal), represent the simplest of all planar defects. This simplicity should be of great aid in unraveling structure-property correlations. The goal of this section is to calculate the zero-temperature surface energy associated with relaxed free surfaces, the geometry of which is derived from the perfect-crystal positions of the atoms.

The unrelaxed structures of the free surfaces considered here were obtained by cutting a perfect crystal along a certain plane normal and subsequently removing of the atoms on one side. In a deliberate attempt to discourage surface reconstruction, the atoms were kept at their perfect-crystal sites prior to relaxing the structure at zero temperature by means of an iterative energy minimization method. Three free surfaces (100), (110) and (111) were considered. For the many-body potential of embedded-atom method, the perfect-crystal cohesive energy per atom, $E_{coh}=U/N$, is readily obtained from eq. 2.4. Here U is the total energy of a system of N atoms. The surface energy, γ_s, then becomes [Wolf 1990]:

$$\gamma_s = \frac{1}{A}\left(n E_{oh} + \sum_i F(\rho_i) - \sum_i \sum_{i<j} \phi(r_{ij}) \right) \tag{3.32}$$

where i and j are now summed over a free surface containing n atoms in the unit cell of area A.

3.8. Monte Carlo Simulation

The fracture properties of many polycrystalline materials are known to have a close dependence on microstructure and the properties of the grain boundaries that compose the microstructure. Microstructure can also have deleterious effects on fracture toughness. For example, weak grain boundaries in a material provide an easy path for crack propagation. In classical fracture mechanics, changes in microstructure are usually accounted for by simply modifying the values of a fracture toughness parameter. In many cases, however, this need has been addressed by performing careful analyses of the interaction between individual cracks and individual grain boundary. While this approach has proven to be quite useful and successful, it ignores the fact that microstructure consists not of a single grain boundary but of large ensembles or networks of grain boundaries.

In order to simulate fracture in a polycrystalline material, a realistic polycrystalline microstructure must first be mapped onto the microstructural model. Such a polycrystalline microstructure may be produced by experiment or by using the Monte Carlo simulation procedure introduced by Anderson et al. [1984] and Srolovitz et al. [1984]. The Monte Carlo simulation procedure has been shown to produce microstructures with grain size and grain topology distributions in excellent accordance with experiment.

In the Monte Carlo simulation, a continuum microstructure is described by a two-dimensional triangular lattice matrix containing 10,000 sites. Each site represented a small area of the microstructure and was assigned a number, S_i, which corresponds to the orientation of the grain in which it is embedded. The number of distinct grain orientations is Q. The lattice site which is adjacent to neighboring sites with different grain orientations is regarded as being adjacent to a grain boundary, while a site surrounded by sites with the same grain orientation is in the bulk or grain interior. The grain boundary is specified by associating a positive energy with grain boundary bonds and zero energy for bonds in the grain interior, according to:

$$E_i = -J \sum_{j}^{nn(i)} (\delta_{S_i S_j} - 1) \tag{3.33}$$

where δ_{ij} is the Kronecker delta, the sum is taken over nearest neighbor (nn) sites of site i, and J is a positive constant that sets the energy scale of the simulation. The kinetics of boundary motion is simulated via a Monte Carlo technique in which a lattice site is selected at random and its orientation is randomly changed to one of the other grain orientations. The change in energy associated with the change in orientation is evaluated. If the change in energy is less than or equal to zero, the reorientation is accepted. However, if the energy is raised, the reorientation is rejected.

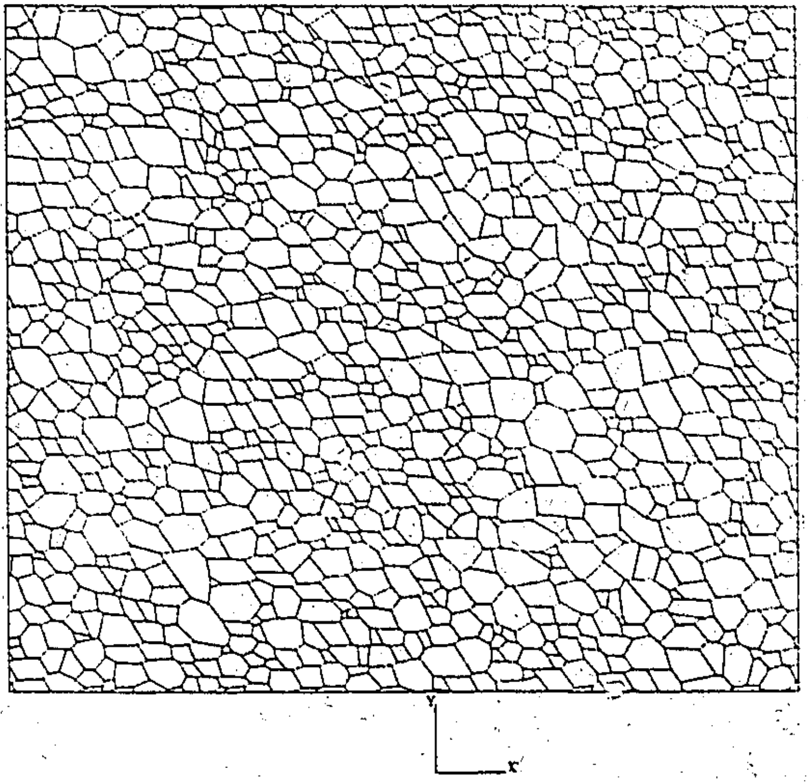

Figure 3.10 An example of the two-dimensional microstructure with 1141 grains and 3265 grain boundaries obtained from Monte Carlo simulation after 10,000 MC steps.

For the simulations of polycrystalline microstructure, the orientations are initialized by randomly assigning an index between 1 and Q to each lattice site and then running the Monte Carlo simulation procedure until the desired grain size is produced [Szpunar and Hinz, 1993]. In our simulation, the maximum value Q is 1500. In the results obtained from the Monte Carlo simulation, we defined the grain boundary as the direct link between the nearest triple points within a grain. The grain boundary character, energy, and fracture resistance are then assigned to each grain boundary according to the grain boundary distribution.

The resultant two-dimensional polycrystalline microstructures are similar to those often found from taking cross-sections through three-dimensional polycrystalline materials. Figure 3.10 shows an example of the two-dimensional microstructure with 1141 grains and 3265 grain boundaries obtained from the Monte Carlo simulation after 10,000 MC steps. A related grain size distribution as determined from this cross-section is shown in Figure 3.11. The shape of the grain size distribution function obtained from this simulation is similar to typical experimental shapes. Not only does the Monte Carlo simulation produce an accurate representation of observed microstructures, it also has the advantage of producing microstructures on the same map as that employed for the microstructural mechanics simulations.

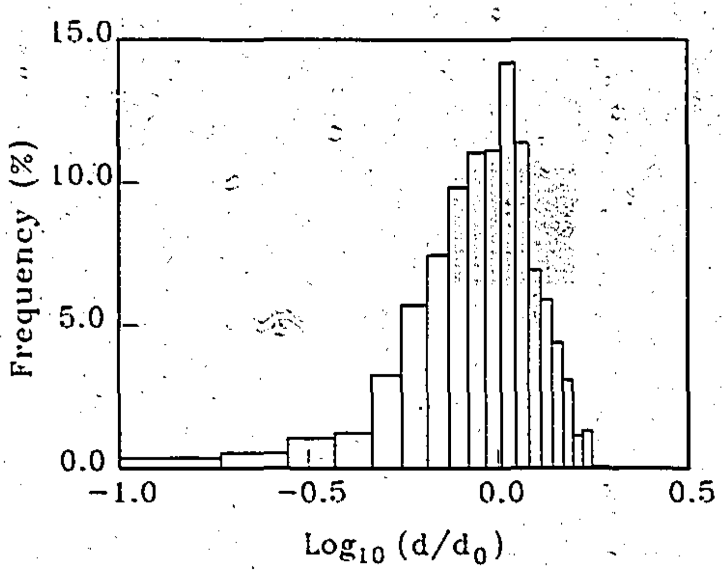

Figure 3.11 Grain size distribution as determined from cross-sections of the microstructure with 1141 grains and 3265 grain boundaries. Here d_0 is the average grain size.

3.9. Fracture Models at the Microscopic Level

Having presented the computer models and simulation methods at atomistic level in the previous sections, we now describe in this section a microscopic computer models based on the microstructure calculated from the Monte Carlo simulation.

3.9.1. Intergranular Fracture Toughness

To investigate the fracture process in polycrystalline materials, we must deal with the energetics of intergranular fracture and focus on energy change between the grain boundary and the surface of fractured bicrystal specimen. According to the energetics, when the intergranular fracture occurs and the plastic deformation is involved, the driving of the crack propagation energy γ is given by:

$$\gamma = 2\gamma_s - \gamma_{GB} + \gamma_p \tag{3.34}$$

where γ_s is the surface energy of the exposed grain boundary, γ_{GB} is the energy of the preexisting grain boundary, and γ_p the plastic energy associated with the propagation of the microcrack. It is clear that the energy γ is smaller in the absence of plastic deformation, than in the presence of plastic deformation. Moreover, it should be noted that as the contribution of γ_p to γ decreases, a stronger dependence of fracture energy γ on the grain boundary energy γ_{GB} is expected. This is an indication that the intergranular fracture becomes more important [Watanabe 1989]. Therefore, the fracture mode in brittle materials is predominantly intergranular.

The grain boundary energy γ_{GB} is known to depend on the type and the structure of the grain boundary, i.e., the boundary misorientation and inclination described by the crystallographic and geometrical parameters. We can expect that the fracture energy depends on the type and structure of the grain boundary. The γ_{GB} is a measure of this dependence, and the surface energy

γ_s does not change with crystallographic orientation as much as γ_{GB} does. This opens the possibility of theoretical analysis of structure-dependent intergranular fracture. From Eq.(3.34), it is evident that the low-energy grain boundaries are expected to require more energy to break than the high-energy grain boundaries. In other words, the low-energy grain boundaries are more resistant to fracture [Watanabe 1989].

From Eq.(3.34), when intergranular fracture occurs in the absence of plastic deformation, the fracture toughness of brittle material can be defined by the following expression:

$$\mathcal{G} = -\sum_{i=1}^{N} \frac{\gamma_{GB}}{2\gamma_s} \qquad (3.35)$$

and with a reference fracture toughness $\mathcal{G}_{ref} = |\mathcal{G}|$ for $\gamma_{GB}=2\gamma_s$. Here N is the total number of fractured grain boundaries in the crack paths.

3.9.2. Markov Chain Fracture Model

The idea of the Markov chain fracture model is based on a simple geometric model which was recently proposed to evaluate the potential effects of grain boundary design and control on intergranular fracture and intergranular stress corrosion [Palumbo et al. 1991, Aust 1993]. In this simple geometric model, the susceptibility of a bulk material to failure by stress corrosion cracking is defined in terms of the probability of propagating a crack, by the combined action of stress and corrosion, through a finite distance. This length defines a limit, beyond which crack propagation would continue to the point of component failure, even in the absence of active grain boundary paths or a corrosive environment; its magnitude is primarily dependent on the specific stress state. Intergranular stress corrosion cracking susceptibility can thus be considered in terms of the probability of finding a continuous path through grain boundaries to the critical crack length. The crack path consists entirely of intrinsically susceptible grain boundary segments, and each segment is favorably oriented to the direction of the applied or residual tensile stress. A susceptible grain boundary segment can be defined as a crystal interface (planar), which as a result of its structural and/or chemical characteristics, is prone to enhanced corrosion (relative to the lattice) in the specific environment, and/or preferential sliding or fracture under the local operative stress condition.

In the Markov chain fracture model, a realistic geometric microstructure and a realistic grain boundary character distribution were considered. The geometric microstructure could be obtained from the experiment or from the Monte Carlo simulation. The grain boundary character distribution could also be obtained from the experiment. In addition, the probability of intergranular fracture at a given triple junction is calculated according to the fracture resistances of grain boundaries at this triple junction. On the basis of geometric considerations, intergranular crack arrest (i.e., crack blunting or transition to transgranular crack propagation) can be considered to occur at a triple junction when the probability of crack continuation along either of the two available intergranular paths becomes negligible. As represented in Figure 3.12, this local probability can be considered to be a function of both the orientation of the interface relative to the stress axis (n), and the intrinsic character (structure and chemistry) of the grain boundary.

In the Markov chain fracture model, when both the orientation of the grain boundary plane relative to the stress axis and the intrinsic character of grain boundary are considered, the probability of crack front extension for a grain boundary at a given triple junction can be shown to be given by:

$$P = \begin{cases} 1, & \sigma(\theta) \geq \sigma_{GB} \\ \exp\left(\dfrac{\sigma(\theta)}{\sigma_{GB}} - 1\right), & \sigma(\theta) < \sigma_{GB} \end{cases} \qquad (3.36)$$

where $\sigma(\theta)$ is the applied tensile stress on the grain boundary, θ is the angle between the grain boundary plane and the stress axis, σ_{GB} is the fracture resistance of the grain boundary. The probability of crack extension along a given grain boundary is one when the fracture resistance of this grain boundary is less than the applied tensile stress on it (i.e., the grain boundary path will allow forward advance of the crack propagation). When the fracture resistance of the grain boundary is greater than the applied tensile stress on the grain boundary, there is still a chance of advance of the crack propagation according to the calculation from eq. 3.34.

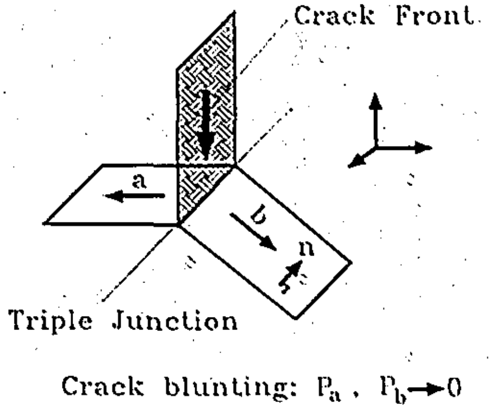

Figure 3.12 Schematic representation of conditions leading to intergranular cracking termination (crack blunting or transition to transgranular) at a triple junction. P_a, P_b are the probability of crack front extension [Palumbo et al, 1991].

For a given grain boundary character distribution, the propagation of a crack through a polycrystalline microstructure started at the triple junction in the surface of the sample. This was necessary since prior to the development of the crack, the sample was elastically homogeneous. The crack begins by propagating along the low cohesion grain boundary network until it reached a point where both grain boundary paths at the triple points do not allow forward advance of the crack propagation, thereby arresting the crack's advance. The vertical distance from this triple point to the start point in the surface is called the crack arrested distance. If the crack path propagates through the whole sample, the crack arrest distance is equal to the sample's width and this sample is a definite failure. All possible crack paths must be calculated with the possible initial crack at triple points in the surface of the sample. In addition, for a given grain boundary character distribution, there exist many possible configurations for each grain boundary in the microstructural sample. Therefore, in order to get very good statistic simulation results, as many configurations as possible must be calculated. In this investigation, we have calculated 80 configurations by using 80 different initial random seeds. In our experience, every calculated result converges to a value when 60 configurations are used. In the calculations we assume that (i) no transgranular fracture, and (ii) the maximum value of the applied tensile stress on the grain boundary is half of the fracture resistance of a single crystal. The final normalized crack arrest distance required to arrest 99% of all propagating cracks is calculated by:

$$\frac{L}{d_0} = \frac{1}{d_0}\sum_j \sum_i L_{ij} \qquad (3.37)$$

where d_0 is the average grain size. The first sum is taken over all possible initial cracks at triple points in the surface area and the second sum is taken over 80 different configurations of grain boundary in the sample. Figure 3.13 presents the data flow of the Markov chain fracture simulation.

Using this microscopic model, the crack path, crack arrest distance and fracture of polycrystalline materials were investigated by changing the grain boundary character distribution, i.e., the fraction of low-energy grain boundaries, the grain boundary fracture resistances, and the orientation distribution of grain boundary plane and grain shape factor.

The grain shape factor f_{sp} is calculated by:

$$f_{sp} = \frac{1}{N}\sum_{i=1}^{N} \sin^2\theta \qquad (3.38)$$

where N is the total number of grain boundaries in the sample and θ is the angle between the grain boundary plane and applied stress axis.

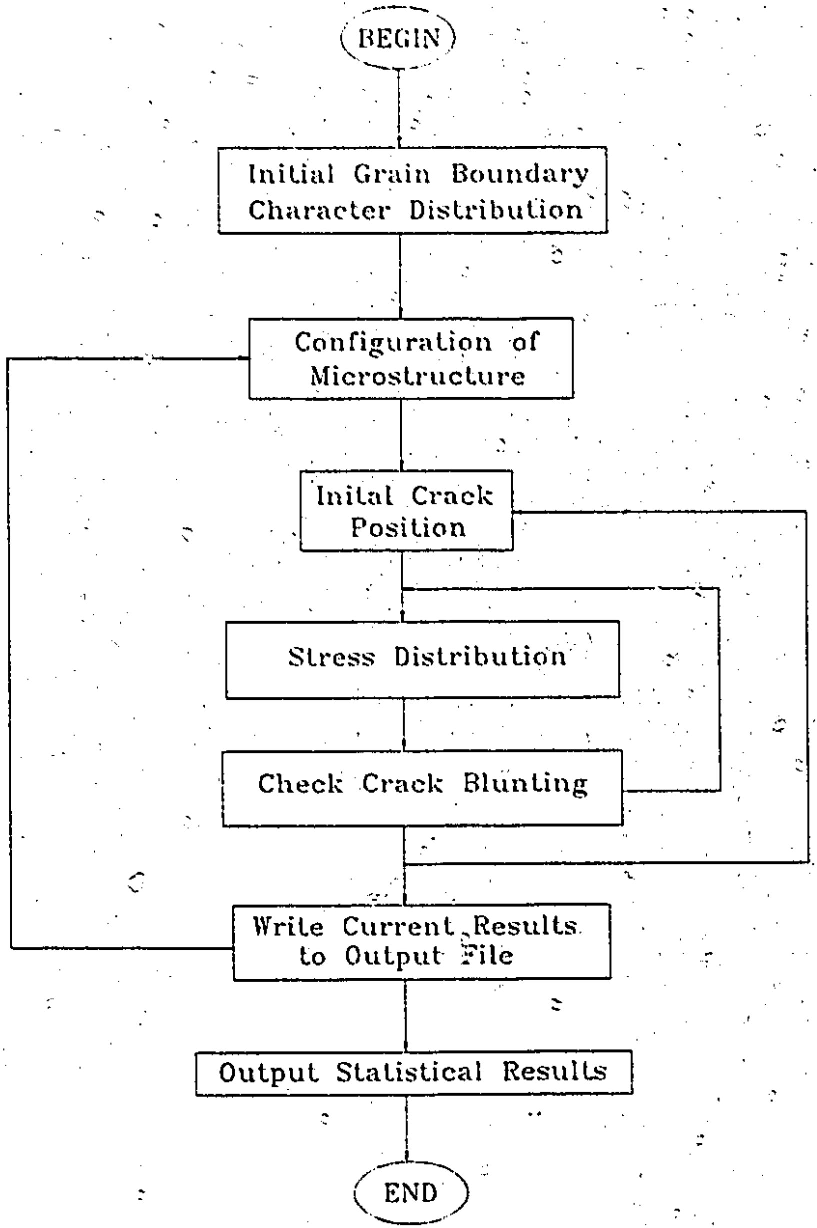

Figure 3.13 Data flow of Markov chain fracture simulation.

In order to study the effects of orientation distribution of the grain boundary planes on the intergranular fracture, three regions are defined based on the orientation of grain boundary planes relative to the applied tensile stress as shown in Figure 3.14.

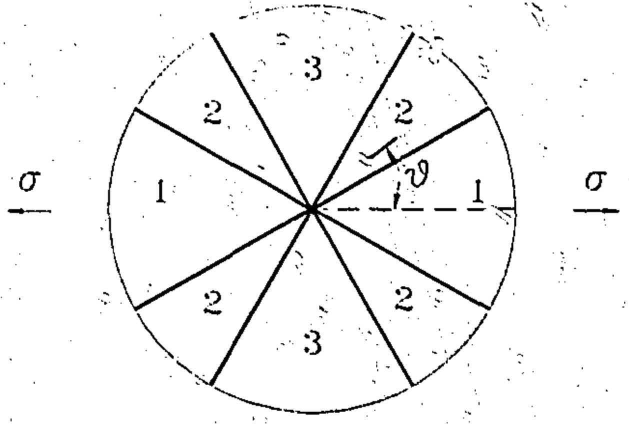

Figure 3.14 Three orientation regions of grain boundary planes. θ is the angle between the grain boundary plane and applied stress σ axis.

3.10. Integrated Approach to Intergranular Fracture

As we have discussed in Chapter 2, the computer simulations have an intimate inter-relation that can be exploited in an integrated approach to modeling complex systems such as interface and intergranular fracture. While such an approach entails considerable effort in implementation, it has the substantial advantage of enabling one to take advantage of the unique capabilities of each of the computer simulations at both the atomistic and microscopic level in a systematic investigation of structure property correlations from zero temperature to melting, including the effects of external stresses applied to the system. The idea is illustrated in Figure 3.15.

The integrated computer codes, enabling a systematic investigation of structure property correlations for interface materials, involves three different levels. At the first level the initial geometry is considered. The input required consists of the macroscopic degrees of freedom needed for the geometrical characterization of a given problem and process. At the second level, it includes the lattice statics and molecular dynamics, and at the third level, it includes the Markov chain fracture model and Monte Carlo simulation.

The integrated approach described here takes full advantage of the complementarity of the different simulation methods. We believe that the interactive aspect of this approach holds the greatest promise in our goal to unravel the correlation between the structure and properties of materials. It is the insights gained from such an approach which, in our view, will lead to the ability to design materials with the desired properties.

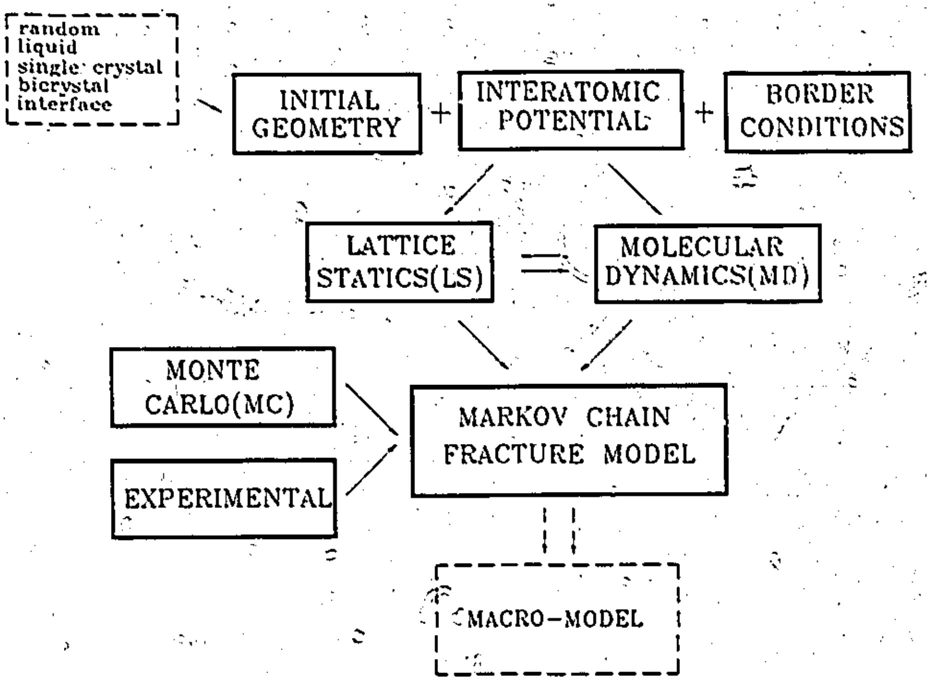

Figure 3.15 Integrated approach for computer modeling of intergranular fracture.

CHAPTER 4:

VERIFICATION OF COMPUTER SIMULATION MODELS

The aim of this project is to model the behavior of grain boundary systems that are not well understood and known. In order to obtain reliable results, it is necessary first to apply the computer simulation models to simple systems for which data are experimentally available and can be used to verify the model's predictive ability. To this end, the applications of embedded-atom method to liquid, glass formation and crystallization of liquid and glass for transition metal Ni, and the applications of bi-crystal model to the grain boundary melting of Al are presented in this chapter.

4.1. Liquid, Glass Formation and Crystallization of Glass for Ni

- A Verification of Embedded-Atom Method

4.1.1. Introduction

As we already know, the equilibrium lattice constants, sublimation energy, bulk modulus, elastic constants and vacancy-formation energy calculated using the embedded-atom method agree quite well with the experimental values. This gives us confidence in the reliability of the EAM functions. We also know, however, that although the EAM functions and their calculations are based on the perfect fcc crystal with very simple defects at low temperature, we are not certain these EAM functions are good for the bulk materials with complex defects at higher temperatures. In order to determine the true result, we have conducted simulations of the liquid metal Ni at high temperature, glass formation of the liquid, and crystallization of the glass, which can be compared with available experimental results.

Liquid metal and glass are very complex system. Glass formation and crystallization processes of liquids by quenching simple metals such as sodium [Watanabe and Tsumuraya 1987, Qi et al. 1992], rubidium [Hsu and Rahman 1979, Mountain and Basu 1983, Brown and Mountain 1984, Lu and Szpunar 1992] and Lennard-Jones (LJ) system [Swope and Andersen 1990, Mandell et al. 1977] have been investigated by Molecular-dynamics (MD). Unfortunately, there is no suitable energetic modeling of transition metals for the study of complex defects or glass systems. As an alternative to be used in these cases, however, pair potentials require large volume-depend terms representing the energy of electron gas and the structure-independent portion of the electron-ion interactions [Johnson 1972]. It is not clear how these contributions should be treated near extended defects and surfaces. Recently, Daw and Baskes [Daw and Baskes 1983, Daw and Baskes 1984] and Finnis and Sinclair [Finnis and Sinclair 1984] have developed the embedded atom method (EAM) for calculating the energetics of transition metals. The major development in the EAM is the replacement of the volume dependency with a more complex term which can be interpreted in a variety of ways and incorporate an approximation of the many-atom interactions neglected by the pair potential.

MD simulation is potentially capable of providing very detailed microscopic features of materials. However, most of these MD simulation studies on glass formation and crystallization held the volume of the system constant throughout the simulation. In recent work on LJ systems [Nosé and Yonezawa 1986], the constant pressure MD approach was adopted. However, the total pressure of the state did not include the effects of the density dependence (due to the electronic screening effect) of the effective ion-ion potential. Only the two-body interactions were considered. This cannot adequately explain such experimental results as the volume, energy, and other thermal properties, as well as their variation with the temperature of transition metals and alloys. With the EAM the contribution of the pressure of a system can be easily calculated by using of the so-called "pressure equation of state".

The computer simulation used here is based on constant pressure molecular dynamics (N-P-T-MD), by which the volume of a system can adjust itself so that it is consistent with given pressure and temperature. It is a powerful technique used for investigating of the glass formation and crystallization. This technique allows us to calculate atomic trajectories and thus simulate the microscopic behavior of both equilibrium and non--equilibrium systems at constant pressure by changing the temperature.

In the present study, the EAM is applied to investigate the glass formation and crystallization of supercooled metallic liquid Ni based on the two different cooling rates, the crystallization process of metallic glass Ni with elevating temperature using the N-P-T-MD technique. The pair distribution function is calculated for each final state, and the atomic volume and the microstructure factors are also given as a function of temperature.

4.1.2. Simulation Procedure

The liquid, metallic glass and crystal structure of Ni are simulated using the constant pressure molecular dynamics (N-P-T-MD) technique which adjusts the atomic volume to keep the pressure equal to atmospheric pressure and constant throughout all simulation runs. The N-P-T-MD simulation is carried out in a cubic box subject to periodic boundary conditions for a system with 6912 atoms. The effective pair potential is cut off at 21.0 a.u. The time unit is 3.73×10^{-13} s and the time step is 5.0×10^{-15} s. We use the damped force method [Hoover et al. 1982, Evans 1983, Brown and Clarke 1984] to change the temperature. In order to get an equilibrium liquid at the beginning of the simulation, the system starts at 1773 K, this temperature being higher than the melting temperature of Ni by 46 K, and the system is kept constant at this temperature for 20,000 time steps. Then two different quenching processes were carried out. One is a fast cooling process in which the system is cooled from the liquid state at 1773 K to the metallic glass state at 300 K, with a cooling rate of 2.48×10^{14} K s^{-1}. The other is a slow cooling process from the liquid state at 1773 K to the crystal state at 300 K with cooling rate of 5.95×10^{12} K s^{-1}. The metallic glass then is heated from 300 K to 1000 K at a heating rate of 2.80×10^{12} K s^{-1} to study the crystallization of metallic glass Ni. The atomic volumes Ω and the structural configurations are recorded during simulations. The structural analysis of liquids, metallic glasses and crystals is performed by using the pair analysis techniques and the index of Honeycutt and Andersen [1987]. The pair distribution functions (PDF's) g(r) are given by:

$$g(r) = \frac{1}{N} \sum_{i,j>i} \delta(r_{ij} - r) \tag{4.1}$$

and were calculated every 4000 time steps and then averaged at each final temperature.

4.1.3. Results and Discussion

The calculated pair distribution function (PDF) at 1773 K for Ni is shown in Figure 4.1(a). This curve is very close to the experimental data (represented by circles in the figure) obtained from Fourier transform of the experimental structure factor [Waseda 1980]. The result indicates that in this simulation, at 1773 K the metal is in the liquid state. The atomic volume predicted for pure Ni at 1773 K is 86.78 a.u., which is very close to the experimental value 85.19 a.u. [Waseda 1980].

Rapid solidification has generated new classes of materials ranging from metallic glasses to microcrystalline unconventional materials. A metallic liquid can form either a non-equilibrium phase (a metallic glass or a quasicrystal), which is obtained by quenching it quickly so that the nucleations of equilibrium phases are suppressed, or an equilibrium phase, if the quenching process is slow. Hence different materials with different microstructure can be formed by changing the quenching process. Some of these materials have demonstrated exceptional mechanical properties, as well as other unique physical properties. These properties are largely influenced by the relaxation and crystallization after heating.

Figure 4.1(b) shows the pair distribution function at 300 K, simulated with the fast quenching rate. In the figure, the second peak of the PDF appears to be split and has a neighboring peak at a higher value of r. This phenomenon is a well-known feature in the PDF's of metallic glass

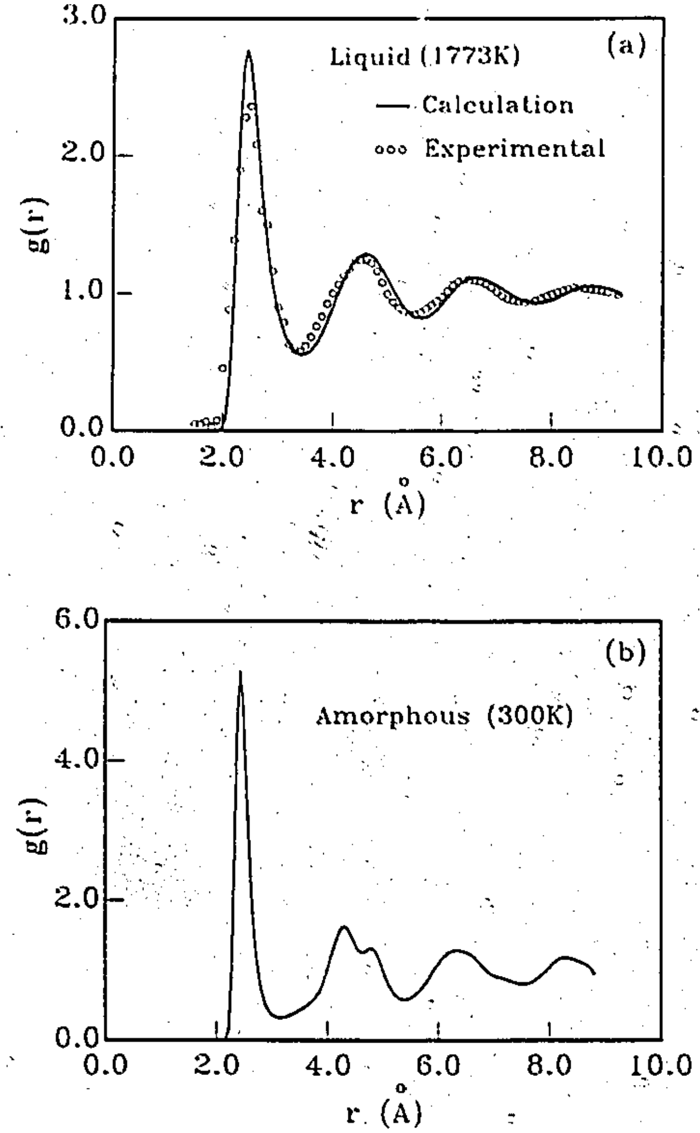

Figure 4.1 Calculated pair distribution functions for pure Ni in

(a) liquid state at 1773 K (46 K above T_m) (The circles represent the data obtained from Fourier transform of the experimental structure factor [Waseda 1980]);

(b) glass state at 300 K obtained after 2.48×10^{14} K s^{-1} quenching from liquid;

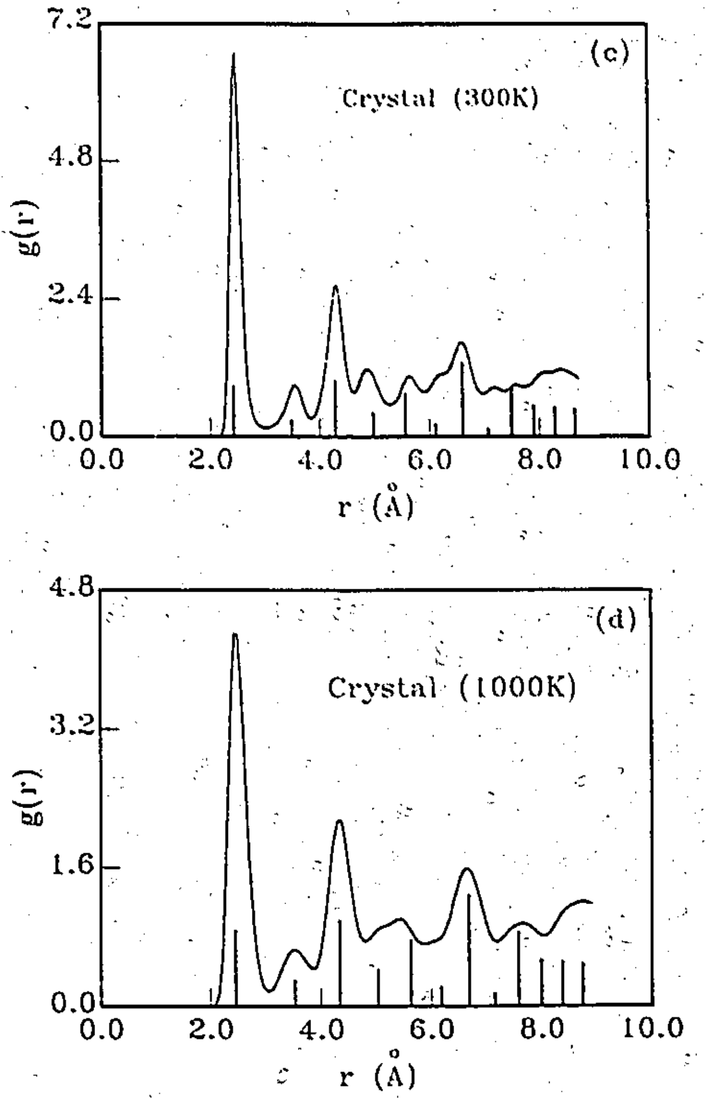

Figure 4.1 Calculated pair distribution functions for pure Ni in
(c) crystalline state at 300 K obtained after 5.95×10^{12} K s^{-1} quenching from liquid;
(d) crystalline state at 1000 K obtained after 2.80×10^{12} K s^{-1} heating from metallic glass.
The vertical lines represent the positions of g(r) maxima for a perfect fcc lattice.

states. The result indicates that the non-equilibrium phase obtained in a supercooled liquid through a fast quenching process is metallic glass which cannot be obtained experimentally in the laboratory for pure Ni.

The pair distribution function in Figure 4.1(c) shows the structural ordering at 300 K obtained using a slow quench rate. There are several peaks in the curve which are compared with the vertical lines that mark the g(r) maxima for a perfect fcc lattice with the experimental atomic volume 73.89 a.u. This means that the crystal resulting from a supercooled liquid through a proper cooling process is a fcc-type, which is consistent with the results obtained experimentally.

The cooling rate controls the structure by influencing the nucleation phenomena. High cooling rates do not allow for nucleation of the equilibrium phases and also make it possible to achieve a high degree of supercooling prior to nucleation. Non-equilibrium phases can thus be formed having a free energy related to the level of supercooling. In fact, under these conditions, equilibrium phases which exist only at low temperatures can also have a chance to nucleate and grow. Such phases grow at a slow rate by solid state transformation under equilibrium conditions.

From the above simulation results, only the final structures can be predicted, whereas the structural transformations with temperature during the rapid solidification are still unknown. As is well known, the atomic volume and structural ordering of a system are closely related to the structure. In our N-P-T-MD simulation, the volume changes as the pressure is kept constant. We could therefore say that these continuous processes are reflecting the real experiments. We have examined the structural changes during quenching by modifying the atomic volume. Figure 4.2(a) shows the atomic volume as a function of temperature for both quenching processes. The open circles are used to show the glass formation during solidification. In this process, the atomic volumes decrease almost linearly with temperature to T_g, below which the atomic volume's decrease is still linear but slower. The profiles observed are characteristic of the variation of the atomic volume during the glass formation process. The glass transition temperature T_g is marked in Fig. 4.2 In this simulation, the T_g for pure Ni is about 995 K with a cooling rate of 2.48×10^{14}

K s^{-1}. The atomic volume at 300 K of the metallic glass Ni is about 76.94 a.u., which is higher than the experimental value 73.89 a.u. for a perfect fcc Ni crystal. The results indicate that the metallic glass of Ni metal is a metastable phase and will crystallize when the time factor and the temperature are changed.

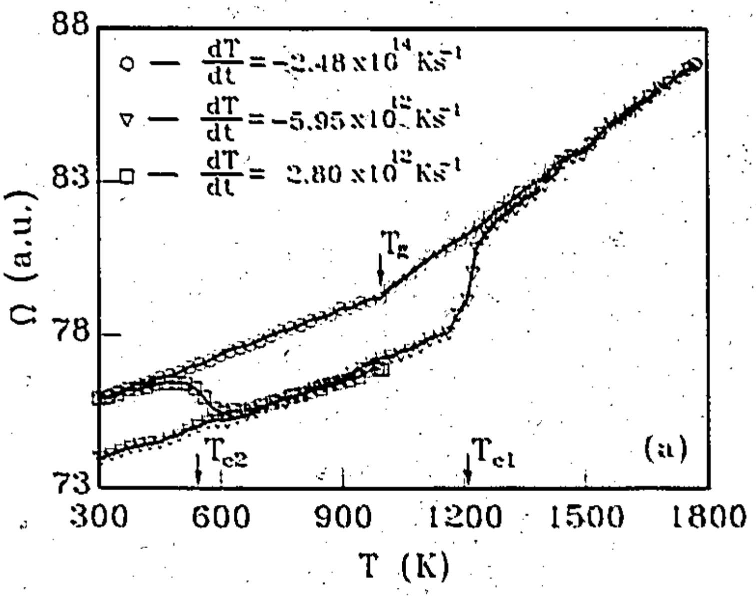

Figure 4.2(a) Atomic volume as a function of temperature. The circles represent the glass formation. The triangles represent the crystallization of supercooled liquid; the squares represent the crystallization of the metallic glass.

The triangles in Figure 4.2(a) are used to describe the atomic volume changes with temperature during the solidification process using the slow quench rate. In this process, the atomic volumes also decrease linearly with temperature to about T_{c1} (1210 K), although the slope is higher than that observed during the glass formation. At T_{c1}, the atomic volumes change dramatically. This indicates that there is a phase transition at T_{c1} for pure Ni cooled with the rate of 5.95×10^{12} K s^{-1}. After this phase transition occurs, the atomic volumes again decrease linearly with temperature.

It appears from the present results that there is a sharp change in the microstructure of the system as the temperature approaches T_{c1}, and that the thermal vibration of atoms has a great influence on the structure of the solid metal at T_{c1}. This conclusion should also apply to the solid metal obtained from the usual liquid-crystal transition, which is known as a first-order phase transition in the Ehrenfest scheme in the literature. Accordingly, the change in the structure of a metallic system during the crystal transformation from a supercooled liquid state is similar to that which occurs in the crystal transformation from the normal liquid state at melt temperature, and hence, the phase transition would be a first-order like transition.

The atomic volume of the crystalline Ni at 300 K is about 74.01 a.u., the value being slightly higher than experimental values (73.89 a.u.) for a perfect crystal. The difference may result from the rapid quenching process. By changing time, the value obtained from the simulation will approach the experimental values characterizing the equilibrium phase.

The microscopic local structure can be described using the Honeycutt-Andersen pair analysis technique. The fivefold symmetry bonds and other kinds of bonds can easily be identified. Figures 4.2(b) and (c) show the percentage of 1551 and 1421 pairs as a function of temperature for both solidification processes. The 1551 bonds represent the configuration of two neighboring atoms with five common neighbors that form a pentagon of near-neighbor contact. The percentage of 1551 bonds is a direct measure of the degree of icosahedral ordering. The 1421 bonds represent the configuration of two neighboring atoms with four common neighbors that form a rectangle with two parallel near-neighbor contacts. These are found mainly in fcc and hcp materials. During fast quenching, the percentage of 1551 pairs increases with decreasing temperature, and 1421 pairs also increase, but no sharp change occurs. That means that the glass structure formation is characterized by an increasing number of 1551 pairs. For slow quenching, the numbers of the 1421 pairs sharply increase whereas the numbers of the 1551 pairs sharply decrease at the crystallization temperature T_{c1}. Figure 4.2 (a), (b) and (c) all illustrate that the

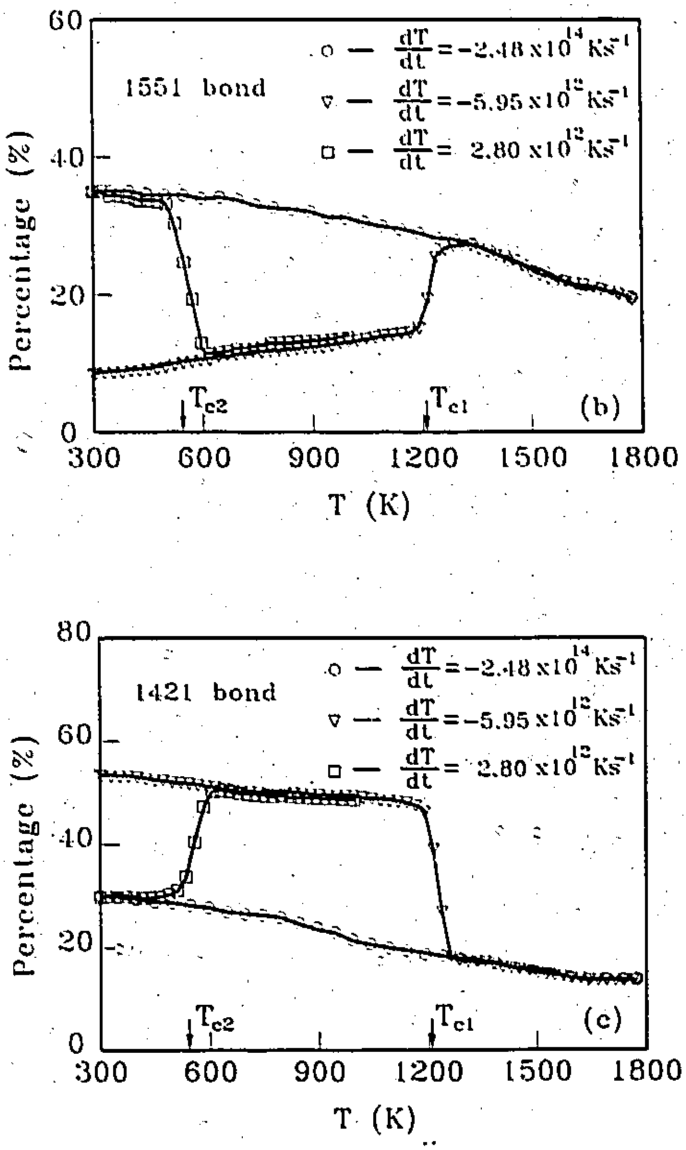

Figure 4.2 (b) Percentage of 1551 pairs, (c) percentage of 1421 pairs as a function of temperature.
The circles represent the glass formation.
The triangles represent the crystallization of supercooled liquid.
The squares represent the crystallization of metallic glass.

phase transition temperature for the slow quenching process is at 1210 K (T_{c1}). The above results indicate that rapid solidification can be clearly described by the atomic volume, the total internal energy and the pair analysis technique.

Metallic glasses produced by rapid solidification from the melt are not completely stable in the quenched condition, so that the microscopic structure and certain properties such as specific heat and internal friction show significant changes during annealing below and above the crystallization temperatures. The crystallization of simple (one-component) metallic glasses is associated only with structural rearrangements in a medium, the composition of which already satisfies the stoichiometric conditions. During crystallization, glass regions may form with the composition of future crystals. In other words, crystallization is preceded by an independent primary pre-crystallization phase. This pre-crystallization occurs due to the formation of glass nuclei of a critical size which are capable of further growth. Detailed microstructural changes such as these are very difficult to investigate using the conventional experimental methods.

Since metallic glass is thermodynamically unstable, a spontaneous transformation to a stable phase should occur above the crystallization temperature. As the metallic glass is heated, it generally transforms progressively to its final stable phase through a sequence of metastable phases. This transformation sequence can be followed by measuring the structural arrangements and temperature dependence of some related properties such as differential specific heat and electrical resistivity. In order to examine the fine structure of the final states after heating from 300 K to 1000 K with a 2.80×10^{12} K s^{-1} heating rate, we have obtained the pair distribution function shown in Figure 4.1(d). There are several sharp peaks in the curve which match the g(r) maxima of a perfect fcc lattice (vertical lines). This means that the crystal structure resulting from the crystallization of metallic glass Ni is a fcc-type structure, which is also consistent with the stable solid structure of Ni.

The squares in the Figure 4.2(a) are used to represent the atomic volume change during the temperature increase. This curve indicates that the crystallization of the metallic glass Ni occurs at about 545 K (T_{c2}) with a heating rate of 2.80×10^{12} K s^{-1}. During heating, the atomic volumes increase linearly with temperature to about 545 K. At this temperature, the atomic volumes decrease dramatically. After crystallization occurs, the atomic volumes again increase linearly with temperature.

The microscopic local structure during the crystallization of metallic glass can also be described using the Honeycutt-Andersen pair analysis technique. The squares in Figures 4.2(b) and (c) represent the percentage of 1551 and 1421 bonds as a function of temperature during the crystallization of metallic glass Ni. When heating begins, the percentage of 1421 bonds increases slightly with temperature, while the percentage of 1551 bonds slowly decreases. At about T_{c2}, the numbers of the 1421 pairs increase dramatically, while the numbers of the 1551 pairs sharply decrease. Above T_{c2}, the 1421 and 1551 pairs change linearly. It appears from these results that there are sharp changes in the microstructure of the system at T_{c2}. Accordingly, the change in structure of a metallic system during crystal transformation from a metallic glass state is similar to that which occurs in the crystal transformation from a normal liquid state at melt temperature. Thus, the phase transition would be also a first-order like transition.

4.1.4. Conclusions

We have applied the embedded-atom method (EAM) to study the glass formation and crystallization of supercooled metallic liquid Ni and crystallization of metallic glass Ni, using the constant pressure molecular-dynamics simulation. The agreements between calculations and experiments for the pair distribution function and atomic volume for liquid Ni are quite good. The microstructures are greatly affected by the quenching rates. The non-equilibrium phase obtained in a supercooled liquid using a fast quenching process is a metallic glass and the equilibrium phase resulting from a slow cooling rate is a fcc-type crystal phase. The metallic glass is not stable in the quenching condition, and with a rise in temperature, crystallization of the metallic glass occurs. The crystal structure resulting from the crystallization is a fcc-type structure. The calculated relationships between the atomic volume, pair structural indexes and the temperature give us a good illustration of the structural transformations and give results which are consistent with the results obtained experimentally.

4.2. Melting of a Twist Σ=5 Grain Boundary - A Verification of Grain Boundary Model

4.2.1. Introduction

The grain boundary melting discussed in this work has been studied experimentally by Chan et al. [1985], who observed visible grain boundary dislocation (GBD) in $\Sigma5<100>$ twist boundaries and in $\Sigma5<100>$ symmetrical tilt boundaries with (310) parallel to the boundary plane. The observations were made for Al during heating to 0.89 T_m and 0.92 T_m, respectively. Upon further heating partial melting of the specimen occurred. Hsieh and Balluffi [1989] observed localized GBDs up to 0.96 T_m for some other special grain boundary, and complete grain boundary melting was detected below 0.999 T_m. These results are clearly in disagreement with previous atomistic modeling calculations [Deymier et al. 1987, Nguyen et al. 1986] which predict a rapid onset of extensive disorder (which appears to be complete melting) at a temperature as low as 0.7-0.8 T_m. Theoretical results were analyzed by Pontikis [1988] who discussed possible reasons for different results obtained in different simulations of grain boundary melting.

The purpose of the present work was to test for the existence of a possible grain boundary disordering transition of the melting type below T_m in an aluminium bicrystal with a Σ=5 (001) twist boundary by a molecular dynamics simulation during heating from 300 K to near T_m. An important aspect of this calculation is that the z borders of the simulation cell are allowed to expand or contract in the z direction according to the pressure within the cell. We consider the simulation cell to be periodic in the x and y directions. In the present simulation, the effective ion-ion interaction [Hasagawa and Watabe 1992, Wang and Lai, 1980] is introduced by calculating the total internal energy of the metal up to the second order of the electron-ion pseudopotential. The contribution of the pressure of a system is calculated using the so-called "pressure equation of state" [Hasagawa and Watabe 1992]. This "pressure equation" is modified to include the density-dependence of the effective ion-ion potential by means of the pseudopotential formalism for electron-ion interaction. We focus on the stability of the grain boundary structure with regard to thermal excitations, but also consider other physical properties such as the internal energy, the structure factor along the direction perpendicular to the interface, and the radial distribution function. We also retain snapshots of the atomic configurations at various stages of the simulation.

4.2.2. Simulation Procedure

We consider a system composed of N particles. In the absence of the three- and higher-body interactions, the Hamiltonian can be expressed as [Hasagawa and Watabe 1992]:

$$H = \sum_{i=1}^{N} \frac{\underline{p}_i^2}{2m} + \frac{1}{2}\sum_{i \neq j} V(\underline{r}_{ij}\,;\,\Omega) + V(\Omega) \tag{4.2}$$

where $\underline{\mathbf{p}}_i$ is the momentum of the i-th particle, m is the mass of the particle, $\underline{\mathbf{r}}_{ij}$ is the vector from i-th particle to j-th particle, Ω is the mean atomic volume, and $V(\Omega)$ and $V(\underline{\mathbf{r}}_{ij};\Omega)$ represent, respectively, the one- and two-body interactions. $V(\underline{\mathbf{r}};\Omega)$ is the interatomic pair potential at certain atomic volume Ω, based on the non-local pseudopotential (EINMP) theory [Wang and Lai 1980, Li et al., 1986] which was discussed in Chapter 2. The pair potential is cut off at 21.0 a.u.

The MD simulation is carried out in a cell subject to periodic border conditions in the x and y directions, while the z border condition is dynamic and non-periodic. The time unit is 4.2796×10^{-13} seconds and the time step is 5.0×10^{-15} seconds. The planar area (x-y plane) of each cell was allowed to change with temperature and the cell length in the z direction was allowed to fluctuate according the internal pressure of the cell. We choose to simulate the Σ=5 (001) twist boundary. This is a boundary on the (001) plane obtained by rotating two perfect semi-crystals with (120) faces by an angle of 36.87° about the <001> direction. A representation of the cell is shown in Figure 4.3(a), viewed from the <001> direction. The simulation cell consists of 36 (001) planes parallel to the x-y plane. Each plane contains 40 atoms, for a total of 1440 atoms. There are 5 fixed layers on both sides of the bicrystal which extend beyond the cutoff length of the pair potential so that a mobile atom near the fixed layer interacts with a perfect bulk solid.

Before the MD simulation can be carried out, the ideal atom positions given by the CSL model must be modified so that each atom feels no force; in other words, the static 0-K structure for the bicrystal must be found. This static structure was found using a steepest-descent energy minimization [Stillinger et al. 1982, 1986] technique which allows the bicrystal to expand or contract in the z direction and also permits each atom to move relatively to its neighbors until each atom feels no force.

The MD simulations were performed using a constant-pressure technique (N-P-T-MD) by which the volume of the system can adjust itself so that it is consistent with the system pressure and temperature. A description of the computational method for determining the total internal energy and the total pressure of a system was presented in the reference [Lu and Szpunar 1992]. At time t=0, each atom was given a velocity consistent with a total system energy chosen so that the system would equilibrate by the time a desired temperature was reached. In order to get an equilibrium structure, the system was first run for 16000 time steps at a given temperature. The atom positions were then recorded at 200 time step intervals, and the pair distribution functions were calculated after 4000 time steps. These values were then averaged.

It proved useful to monitor the atomic ordering by calculating the structure factor S(**k**,z), which is Fourier transform of the atom density. This is given by:

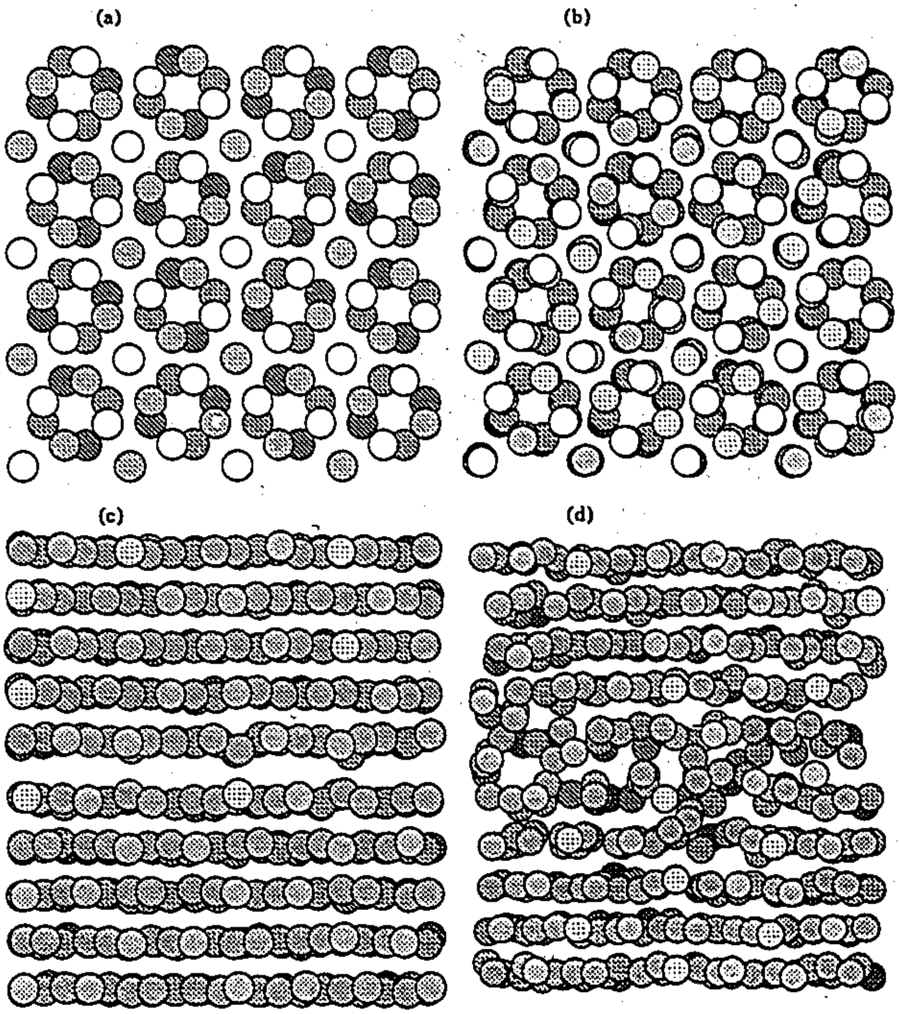

Figure 4.3 Atomic level images for the $\Sigma=5$ (001) twist grain boundary.
(a) initial configuration viewed from <001> direction;
(b) configuration at 300 K viewed from <001> direction;
(c) configuration at 300 K viewed from <010> direction;
(d) configuration at 900 K viewed from <010> direction.

$$S(\boldsymbol{k}, z) = \langle \frac{1}{N_z^2} \left| \sum_{j=1}^{N_z} \exp (i \boldsymbol{k} \cdot \boldsymbol{r}_j) \right|^2 \rangle \tag{4.3}$$

where k is the reciprocal-lattice vector $(4\pi/a_0)(1,0,0)$, N_z is the number of atoms in a thin (x-y) planar slab of the model at a given depth z, r_j is the position of atom j, and < > denotes a time average. The value S(**k**) ranges from 1.0 for a perfectly ordered solid to 0.0 for a perfectly disordered or melted one.

4.2.3. Results and Discussion

The choice of atomic potential will affect the results of any MD simulation, and did indeed affect our simulation of the melting process. Therefore, a verification of our potential and calculation was carried out as the first stage. Fig. 4.4(a) shows the average atomic volume Ω of the system as a function of temperature during heating for both bulk and bi-crystal Al. The calculation for the bulk was carried out in a cubic box subject to periodic boundary conditions for a system with 2048 atoms. To obtain an equilibrium state, the system was run for 10000 time step using the constant pressure MD simulation. The result indicates that the calculated melting temperature T_{cm} of the bulk is around 960 K. Fig. 4.4(b) shows the calculated pair distribution function for Al with Ω=135.73 a.u. at 1000 K ($1.042T_{cm}$). We see from this figure that the calculated curve is very close to the experimental data (represented by circles in the figure) obtained from Fourier transform of the structure factor with Ω=127.57 a.u. at 943 K ($1.011T_m$) [Waseda 1980]. This result indicates that the potential we chosen produces good results at temperatures close to the melting temperature of Al.

The structure equilibration and thermal expansion were investigated by running MD simulations for several cells at various temperatures using the constant pressure method. The results of these simulations were also used to verify that the cell heating was causing thermal expansion. The computed mean atomic volume Ω, thermal expansion coefficient α and grain

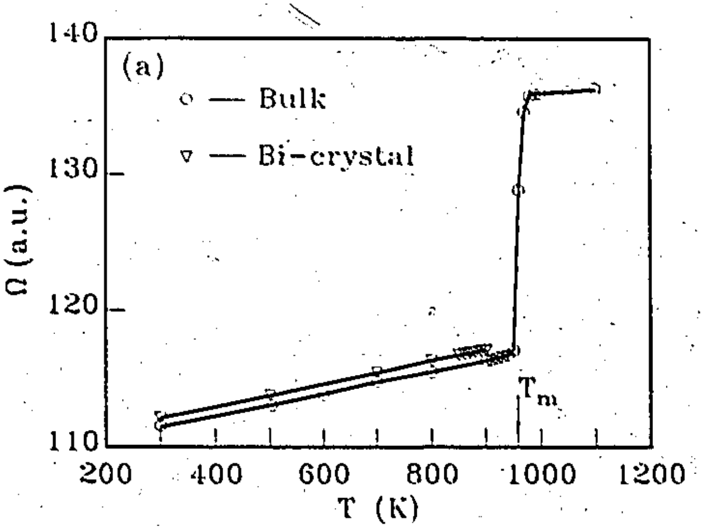

Figure 4.4(a) Average atomic volume Ω as a function of temperature during heating for both bulk and bi-crystal Al. Calculated melting temperature T_{cm} of the bulk is about 960K.

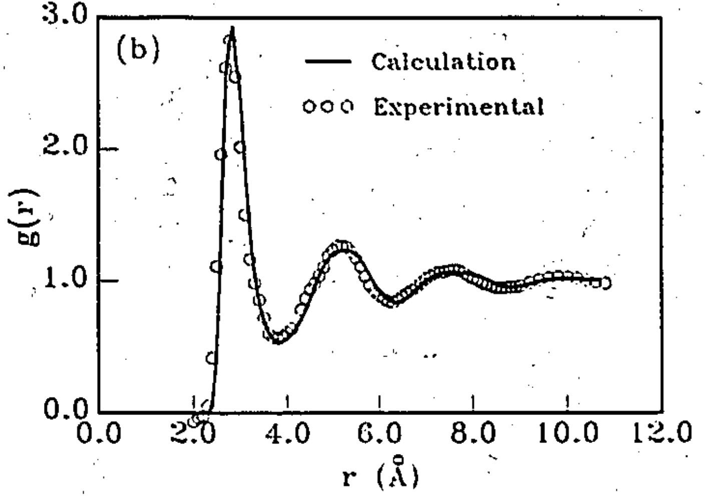

Figure 4.4(b) Calculated pair distribution function for Al with Ω=135.73 a.u. at 1000 K ($1.042T_{cm}$). The circles are obtained from Fourier transform of the experimental structure factor with Ω=127.57 a.u. at 943 K ($1.011T_m$) [Waseda 1980].

boundary energy E_{gb} for the Σ=5 twist grain boundary at different temperatures are listed in Table 4.1. The atomic volume at 300K for the Σ=5 twist grain boundary of Al is approximately 112.09 a.u. This value is slightly higher than the experimental value (111.90 a.u.) [Waseda 1980] and the value of our previous MD simulation of cooling from liquid (112.05 a.u.) [Lu and Szpunar 1993]. Since all the MD simulations are made at constant pressure, this difference could be the result of the existence of the grain boundary. Table 4.1 demonstrates that the thermal expansion coefficients α are in reasonable agreement with the experimental values ($2.31\times10^{-5}K^{-1}$) for Al.

One of the most fundamental properties of a grain boundary is its structure on an atomic level. The grain boundary structure provides insight into other physical properties such as the diffusion or the segregation of impurities at grain boundaries. Comparison of the simulated grain boundary structures with experimental results is useful, not only because it can help us to analyze the experimental observations but because it provides a crucial test of the bi-crystal model and the interatomic interactions used. The grain boundary structures predicted by molecular dynamics simulations using pseudopotential are very consistent. Figure 4.3(b) shows the structure at 300K using a projection along the [001] direction after a total of 20000 time steps. Compared with initial configuration (Figure 4.3(a)), it is evident that the basic crystal structure and a Σ=5 CSL twist grain boundary still exist. It is difficult, however, to image the grain boundary structure in three dimensions from this viewing direction. Figure 4.3(c) illustrates the same grain boundary structure along the [010]. From this image, it is easy to see that the equilibrium grain boundary structure predicted by the MD simulation retains the coincident site lattice periodicity, and that the lowest energy structure corresponds to the coincident site arrangement of the two ideal crystals. It is also apparent that the grain boundary was formed by a migration of atoms from their initial positions to the upper, lower and central areas of the bi-crystal. This migration results in larger average interplanar spacing at the grain boundary than in the surrounding bulk regions. This migration changes the average profile of the grain boundary. Specifically, the disorder near

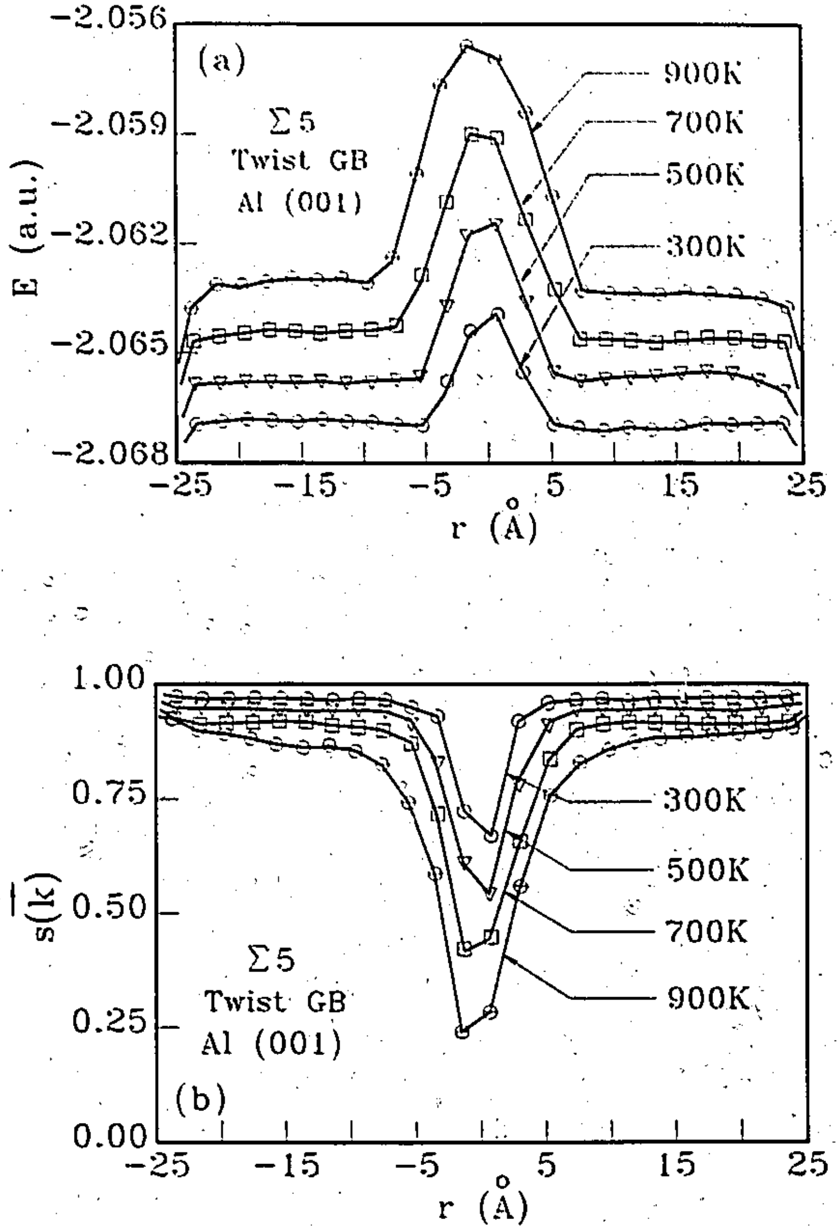

Figure 4.5 (a) Total internal energy E, and, (b) structure factor S(k) calculated across the z direction of the bicrystal model at various temperatures.

the grain boundary has now spread over a wider spatial region.

The energy profile for different temperatures is shown in Figure 4.5(a). Atoms at the grain boundary, as well as several layers of atoms affected by the boundary, all lie in higher energy positions. All the other layers behave exactly like layers of the perfect crystal atoms: the total internal energy curve for these layers is flat, and the values of the total internal energy of these atoms remains the same. This proves that the grain boundary is embedded in a perfect crystal environment.

Table 4.1 Average atomic volume Ω, thermal expansion coefficient α and grain boundary energy E_{gb} calculated using pseudopotential for a simulation cell with a $\Sigma=5$ twist grain boundary.

T(K)	Ω(a.u.)	$\alpha(10^{-5}K^{-1})$	$E_{gb}(ergcm^{-2})$
300	112.09	—	653.17
500	113.74	2.44	880.20
700	115.39	2.40	1144.34
800	116.24	2.45	1325.88
850	116.67	2.46	1367.37
860	116.76	2.57	1381.89
870	116.85	2.50	1396.24
880	116.94	2.48	1410.21
890	117.03	2.46	1469.61
900	117.08	2.42	1555.35

As the temperature increases, the total internal energy of the atoms of both the perfect crystal and grain boundary increase, as do the number of the layers affected by the grain boundary.

Figure 4.3(d) shows the predicted structures at 900K ($0.9375T_{cm}$) in a projection along the [010]. The image shows that the equilibrium grain boundary structure at $0.9375T_{cm}$ predicted by the MD simulation contains two atomic layers which have lost their coincident site lattice periodicity. This indicates an increased migration of atoms at the grain boundary at high temperatures. From the total internal energy curve, however, it is clear that the grain boundary core structure still exists and perfect crystal structure exists outside the grain boundary. Figure 4.6(a) shows the pair distribution functions for the whole system at various temperatures.

These results confirm that the structure of the crystal is still fcc and the grain boundary structure core of whole system still exists up to $0.9375T_{cm}$.

As the temperature increases, the peaks of the PDF broaden and shift away from each other because of thermal expansion and the disorder caused by thermal effects. The most common form of atomic-level structural disorder in the crystal arises from the thermal motion of its constituent atoms, which is usually associated with thermal expansion. As is well known, this homogeneous type of disorder results in a volume expansion originating from the anharmonicity of the interactions among the atoms. Conversely, interface materials are structurally disordered at the atomic level even at low temperatures, due to the very presence of the interfaces. At or near the interfaces, this type of disorder is inhomogeneous. The effect of the interfacial disorder on the volume of the material is nevertheless similar to that of thermal disorder, and usually leads to a volume expansion at the interfaces. However, at very high temperatures near melting temperature, conditions change dramatically, resulting in a type of disorder which is dissimilar to homogeneous thermal disorder.

Figure 4.6(b) represents the pair distribution functions of different regions along the z direction at 900K. The curves (i), (ii), (iv) and (v), which are calculated for the upper and lower blocks with 240 atoms, indicate that the structure in these regions at 900K is fcc. The curve (iii), calculated for the grain boundary core with 80 atoms (two atomic layers), indicates that the structure of this region at 900K represents a liquid-like disorder, the state of so-called partial

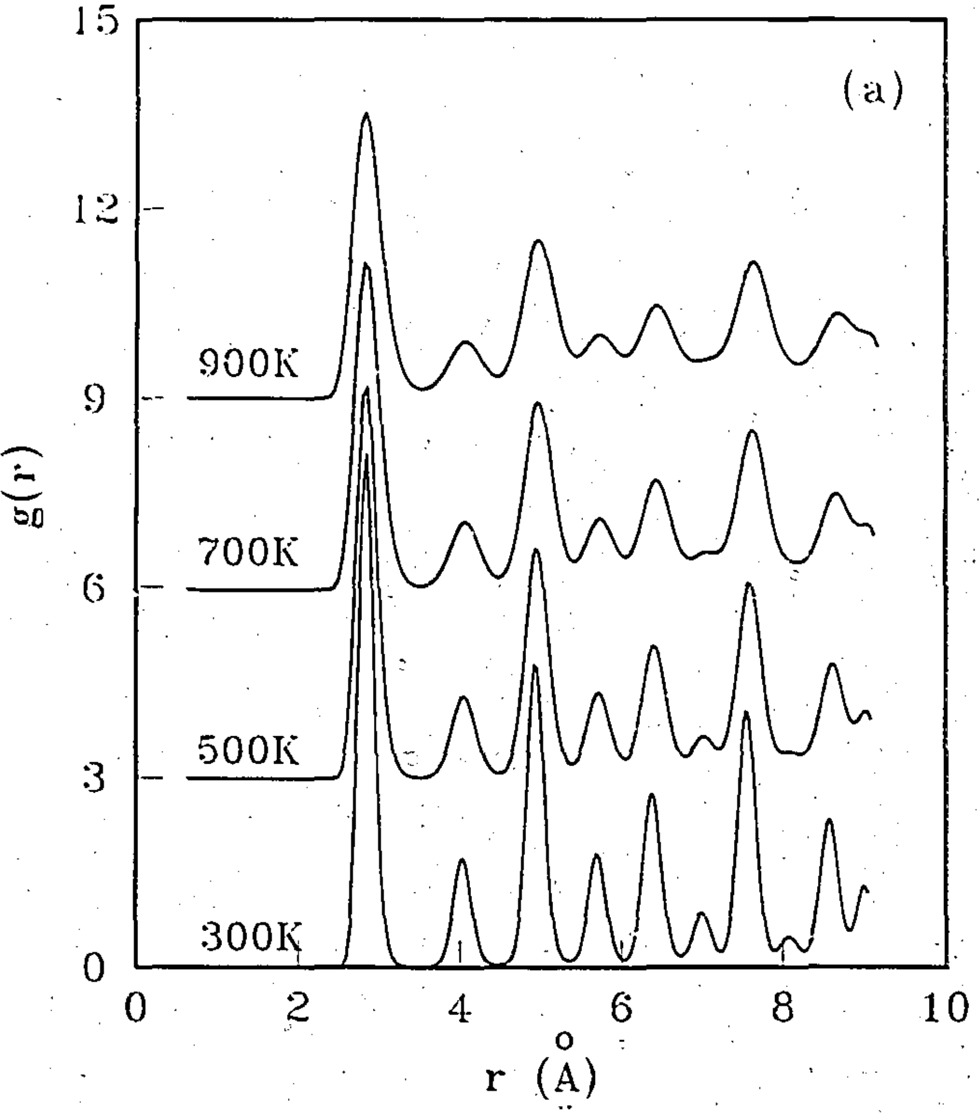

Figure 4.6(a) Pair distribution functions calculated for the whole system at various temperatures;

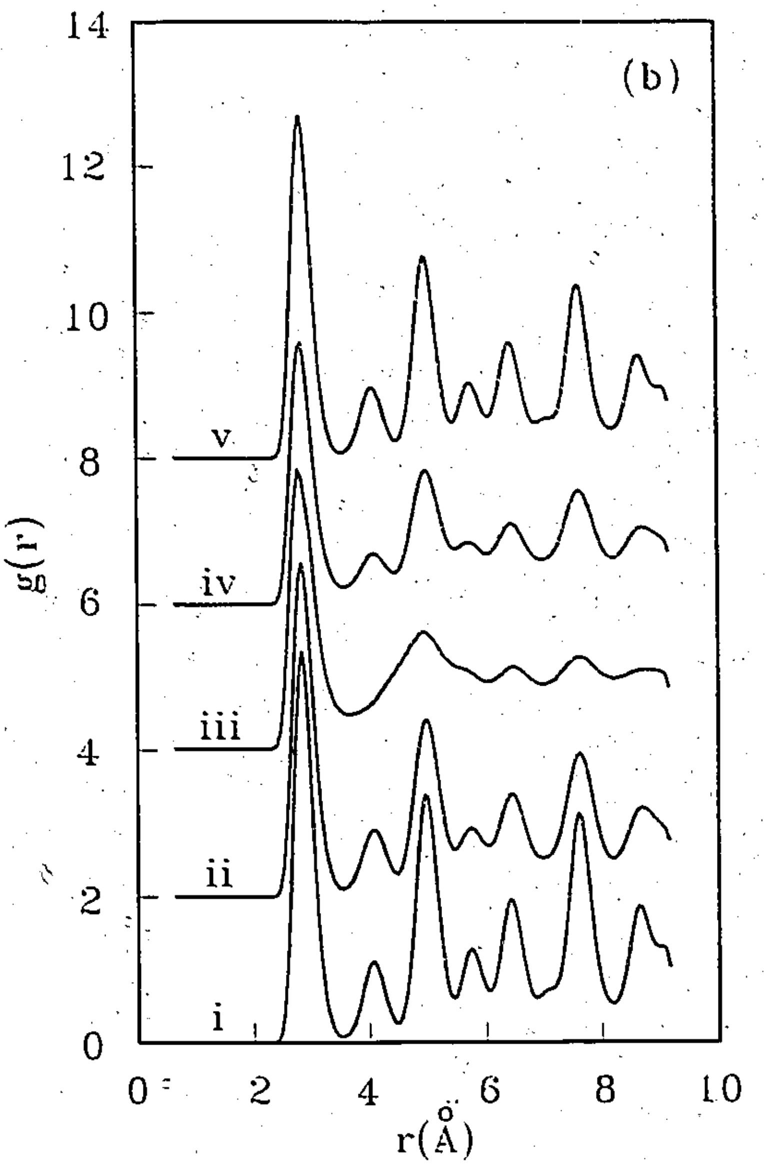

Figure 4.6(b) Pair distribution functions at 900 K calculated across the z direction for different regions with different numbers of atoms: (i) from 6th to 12th plane (240 atoms); (ii) from 13th to 18th plane (240 atoms); (iii) from 19th to 20th plane (80 atoms); (iv) from 21st to 26th plane (240 atoms); (v) from 27th to 32nd plane (240 atoms).

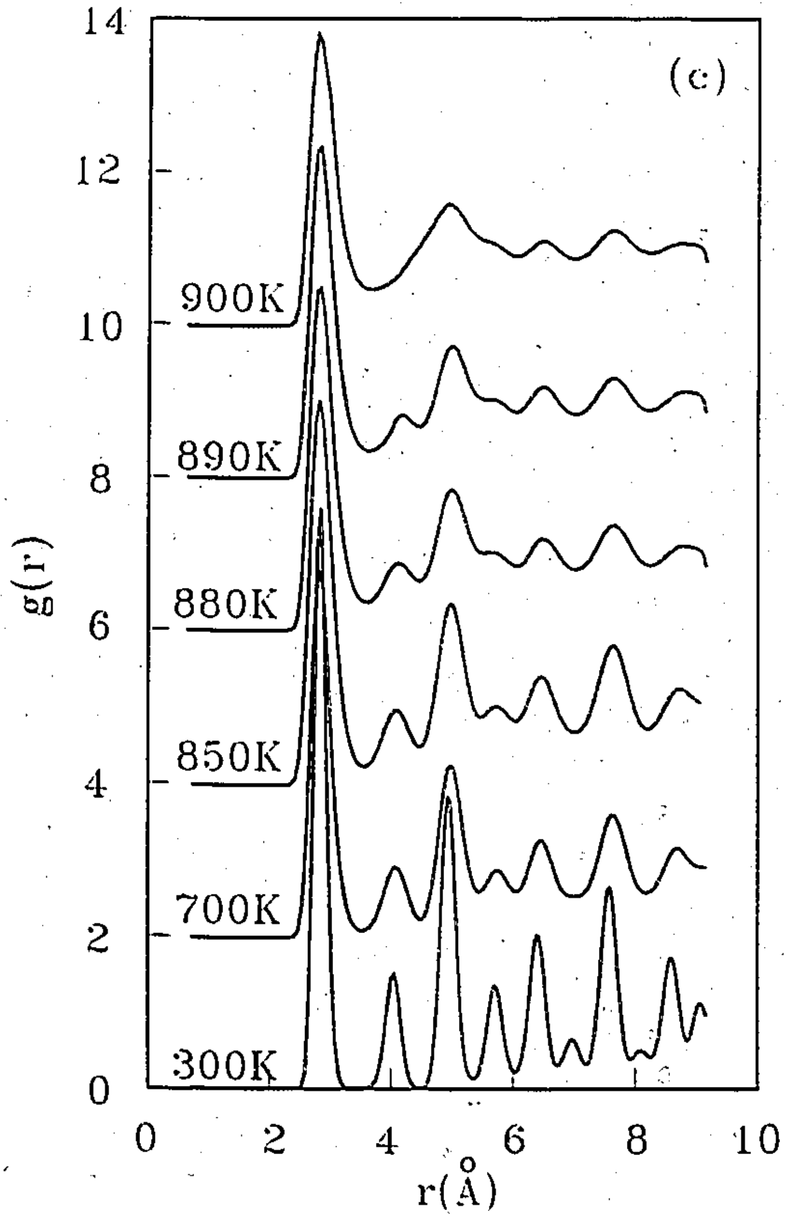

Figure 4.6(c) Pair distribution functions of the grain boundary core at 300, 700, 850, 880, 890 and 900 K with 80 atoms (from 19th and 20th plane).

melting. Figure 4.6(c) shows the pair distribution functions for the grain boundary core with 80 atoms at various temperatures. This figure shows with a rise in temperature, the structure of the grain boundary core is increasingly disordered and at 890 K is still a fcc-type structure. In conclusion, the partial melting of the twist $\Sigma 5$ (001)grain boundary began at around $0.9375T_{cm}$. From Fig. 4.4(a) one can see that the average atomic volume of the bi-crystal system is slightly larger than that of the bulk system, but one cannot see the partial melting of the grain boundary core at 900K because the average atomic volume is calculated for the whole bi-crystal system and partial melting occurs in the grain boundary core with 80 atoms (two atomic layers). Our results are clearly in agreement with all previous experimental results of Al [Chan et al. 1985, Hsieh et al. 1989], and disagree with some other atomistic calculations [Deyimer et al. 1987, Nguyen et al. 1986] which predicted a complete melting at temperatures as low as 0.7-0.8 T_m. Among the factors that can lead to erroneous conclusions [Pontikis 1988], the boundary conditions imposed on the computational cell, the interatomic potential and the size of the cell are worthy of mention.

Another indicator of grain boundary melting is the structure factor S(k) calculated along the z direction for different temperatures (as shown in Fig. 4.5(b)). At 300K the grain boundary is less ordered than the bulk, although the grain boundary core is quite well defined, and S(k) still has a value indicating a certain amount of structural order. The total internal energy in this region is higher than it is in the bulk region. With an increase in temperature, S(k) in the middle of the grain boundary region decreased to a smaller value. Correspondingly, the energy in the grain boundary region increases. It is seen that for all temperatures below T_m, crystal regions which are far from the grain boundary behave like a perfect crystal.

4.2.4. Conclusions

A constant pressure molecular dynamics simulation has demonstrated the effect of temperature on the structure of a $\Sigma=5$ (001) twist grain boundary. The equilibrium grain boundary structure at 300K, predicted by the molecular dynamics simulation using pseudopotential, retains the coincident site lattice periodicity, while the lowest energy structure corresponds to the coincident site boundary between two ideal crystals. This indicates that the grain boundary was formed by atoms migrating from their initial positions to the center of the bi-crystal, and by some other atoms migrating to the upper or lower regions. As a result, the average interplanar spacing in grain boundary are significantly larger than they are for the surrounding bulk regions. Also, higher energy levels of atoms in the grain boundary are apparent. With an increase in temperature, the total internal energy of atoms for both the perfect crystal and the grain boundary increase, and the number of layers affected by the grain boundary also increases. The grain boundary core structure and the perfect crystal structure existing outside the grain boundary still exist at $0.9375T_{cm}$. However, the equilibrium grain boundary structure core at $0.9375T_{cm}$ has two atomic layers which have lost the coincident site lattice periodicity. The structure of these two layers is representative of a liquid-like disorder. Therefore, partial melting of the $\Sigma 5$ grain boundary has occurred at a temperature of about $0.9375T_{cm}$.

4.3. Summary of the Verification

The verification of computer simulation models indicates that the agreement between the model's predictions and experimental results is quite good, which again gives confidence in the reliability of the Embedded-Atom method and the grain boundary model.

CHAPTER 5:

RESULTS AND DISCUSSION OF INTERGRANULAR FRACTURE

The purpose of this chapter is to present the results and discussion of the intergranular fracture investigation that has been conducted using the methods described in Chapter III. The following sections detail the investigations of grain boundary structure and energy, grain boundary fracture of bi-crystals at atomistic level, intergranular fracture of bulk at microscopic level, and an integrated approach of intergranular fracture of polycrystalline materials.

5.1. Grain Boundary, Surface Structure and Energy

5.1.1. Grain Boundary Structure and Energy

The structure, energetics, and free volumes associated with different types of boundaries and their statistical distribution within a polycrystal are expected to exert a dominant influence on macroscopic material properties such as intergranular fracture, grain boundary sliding, boundary migration, and grain boundary diffusion. Grain boundaries in pure metals represent ideal model systems for the investigation of the strictly geometrical aspects of structure-property correlations for the following three reasons [Wolf and Merkle 1992]. First, one avoids the complexity due to the myriad of possible choices of materials combinations forming the interface, thus enabling the researcher to focus on the different roles of the three distinct geometrical aspects of the structure. Second, because grain boundaries are bulk interfaces, dimensional interface parameters (such as the modulation wavelength in strained-layer superlattices, or the thickness of epitaxial layers) do not enter into the problem. Finally, grain boundary energy is thought to play a central role in various grain boundary properties, such as impurity segregation, grain boundary mobility and fracture among others. A better understanding of the correlation between the structure and energy of grain boundaries therefore promises to offer insight into more complex structure-property correlations as well. Also, it represents a base line against which the effects of interfacial chemistry can be probed.

Despite a variety of controlled bicrystal experiments performed to date, a systematic experimental exploration of the special Σ grain boundary with the five macroscopic and three microscopic degree of freedoms has not been performed well. Because of the relative ease with which the macroscopic degree of freedoms can be manipulated in the computer, an approach utilizing the complementary capabilities of atomic-level computer simulation and experiment seems to be particularly promising. However, while a comparison between experiments and modeling results in crucial test cases is absolutely essential, the main strength of such simulations lies in their ability to provide atomic-level insights into structure-property correlations.

It should also be noted that, since real bicrystal is produced at finite temperatures, entropic and kinetic effects may also play a role in determining the properties of bicrystals. At elevated temperatures, the kinetics of all of these thermally activated processes becomes sufficiently rapid that their contributions to the overall behavior of the material are substantial. The common feature associated with all of these phenomena is thermally activated motion in a reduced coordination environment. Free volume provides a good measure of average grain boundary coordination. It is therefore logical to correlate the kinetics of these thermally activated macroscopic material properties with the boundary free volume. Free volume is useful because (a) free volume is a potentially more readily measurable quantity than grain boundary energy, and (b) in some cases it provides a direct link between structure and properties, such as grain boundary energy, grain boundary sliding, migration and fracture, etc.

Energy minimization was performed on the grain boundary structure model, using dynamic borders, by applying the steepest descent relaxation method with a constant stress at the borders. Using the embedded-atom method potentials for Cu, Ni and Al, the correlations between energy, structure, and volume expansion for grain boundaries in Cu, Ni, and Ni_3Al have been investigated. An example of Σ5 (001) twist grain boundary structure for Ni_3Al is shown in Figure 5.1 viewed from the <001> and <010> directions. This grain boundary structure is similar to the grain boundary structure for Al in Figure 4.3, which was calculated using the pseudo-potential. The results of grain boundary energy and grain boundary free volume of 28 Σ grain boundaries in Cu, Ni, and Ni_3Al are listed in Tables 5.1 and 5.2 for symmetric twist and tilt grain boundaries, respectively.

In these studies, it was found that both the grain boundary energy and free volume depend to a high degree on the grain boundary plane. The energy of (001) boundaries is more than twice as large as that of the (111) boundaries. The grain boundary energy and free volume are highly interrelated. A general trend of increasing grain boundary energy with increasing grain boundary expansion was observed. The Σ3, (111) twist and (110) 70.53° tilt coherent twin boundaries have zero expansion and zero grain boundary energy because those grain boundary configurations are identical to the perfect crystal. The results from Table 5.1 and to 5.2 suggest that an important role is played by the grain boundary plane. The interpretation of the large differences in the grain boundary energy and free volume for different planes is essentially based on Pauli's principle [Yip and Wolf 1989]. Although the density in the grain boundary region has decreased due to the volume expansion at the grain boundary, and thus the average distance between atoms has increased, some atoms in a high defected environment are at separations closer than the crystalline nearest-neighbor distance. It appears that in any grain boundary unit cell there are regions of very poor match across the interface which cannot be sufficiently relaxed even when the volume increases.

It should be noted that for most of the boundaries the experimentally obtained volume expansions are about twice as large as the calculated ones, however, the volume expansion for the Σ3 (111) twin boundary in copper [Wood et al. 1986) found by HREM was only about 0.001±0.004nm ($\delta a/a=0.0028\pm0.011$) which agrees very well with the theoretically predicted value.

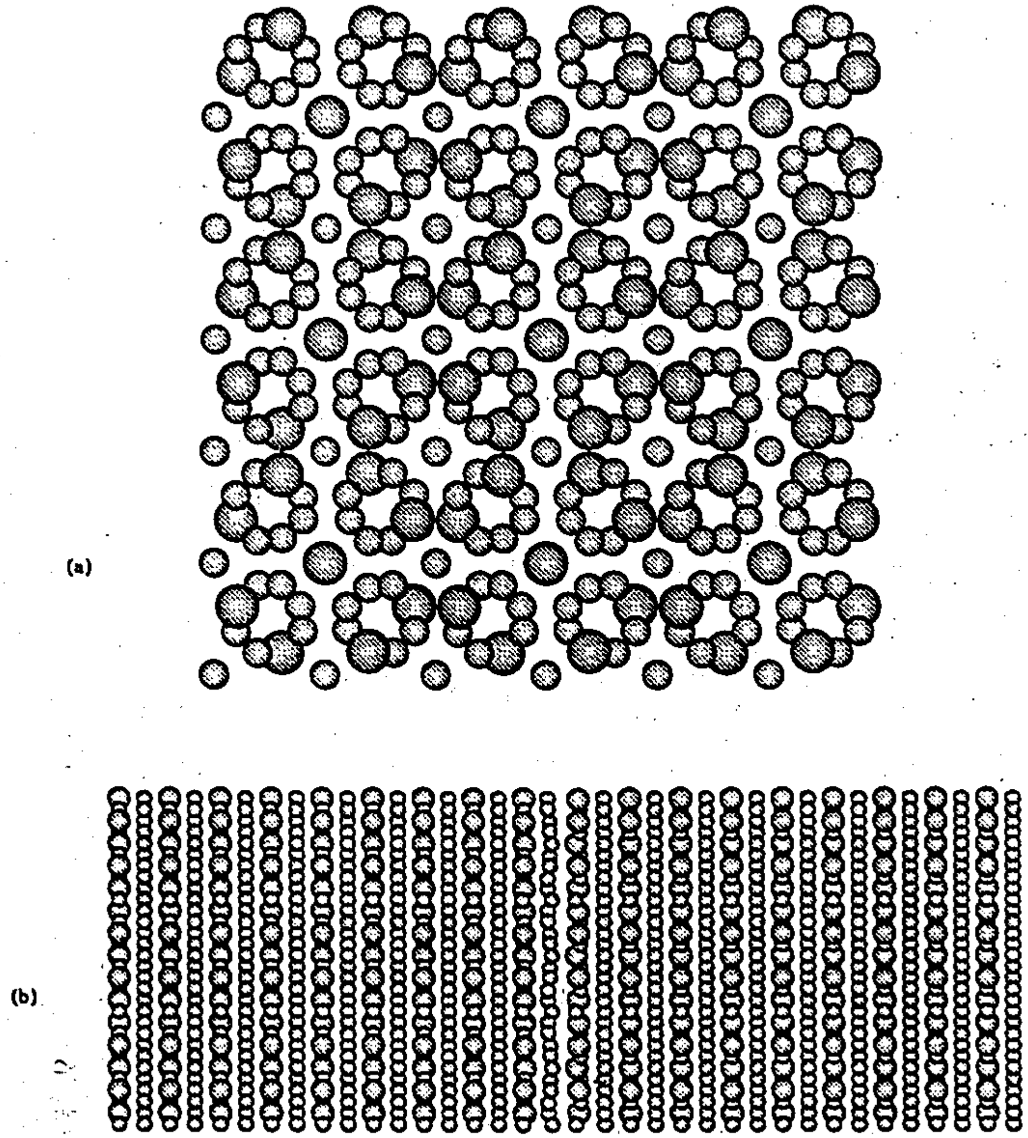

Figure 5.1 The Structure of $\Sigma 5$ (001) twist grain boundary for Ni_3Al viewed from (a) <001> direction, and (b) <010> direction. Ni - small balls; Al - large balls.

Table 5.1 Results of symmetric twist grain boundary for Cu, Ni, Ni_3Al.
E_{GB} is the grain boundary energy;
$\delta a/a_0$ is the grain boundary free volume;
σ_{max} is the maximums of tensile stress.

Axis	Σ	E_{GB} (erg/cm^2)			$\delta a/a_0$			σ_{max} (GPa)		
		Cu	Ni	Ni_3Al	Cu	Ni	Ni_3Al	Cu	Ni	Ni_3Al
100	5	663.32	922.58	971.17	0.077	0.072	0.078	12.31	17.25	16.86
100	13a	619.10	874.54	902.96	0.073	0.075	0.074	12.65	17.87	17.49
100	17a	703.52	995.98	1012.55	0.084	0.086	0.083	11.77	16.73	16.61
110	3	937.93	1307.33	1350.92	0.063	0.061	0.061	11.75	14.67	14.22
110	9	993.10	1396.73	1421.03	0.081	0.082	0.079	11.28	13.97	13.48
110	11	965.52	1343.54	1404.98	0.072	0.069	0.073	11.72	14.26	14.07
110	17b	1062.01	1482.41	1526.09	0.093	0.091	0.092	10.94	13.62	13.19
110	19a	896.55	1252.98	1307.84	0.076	0.074	0.078	12.41	15.34	14.87
111	3	0.0	0.0	0.0	0.0	0.0	0.0	17.84	26.46	26.15
111	7	285.43	402.73	419.46	0.030	0.033	0.032	15.61	23.31	22.26
111	13b	297.49	411.95	437.97	0.032	0.031	0.034	14.24	22.43	21.14
111	19b	265.33	377.94	381.27	0.025	0.028	0.024	16.09	24.27	23.88

Table 5.2 Results of symmetric tilt grain boundary for Cu, Ni, Ni_3Al.
E_{GB} is the grain boundary energy;
$\delta a/a_0$ is the grain boundary free volume;
σ_{max} is the maximums of tensile stress.

Axis	Σ	θ°	E_{GB} (erg/cm^2)			$\delta a/a_0$			σ_{max} (GPa)		
			Cu	Ni	Ni_3Al	Cu	Ni	Ni_3Al	Cu	Ni	Ni_3Al
100	5	36.87	846.44	1199.48	1241.07	0.091	0.092	0.093	9.75	11.63	11.22
100	5	53.13	878.38	1225.79	1295.45	0.085	0.083	0.087	9.53	11.36	10.74
100	13a	22.62	818.18	1151.04	7798.04	0.064	0.066	0.066	10.27	12.41	11.75
100	13a	67.38	678.13	960.86	969.68	0.060	0.063	0.058	11.34	14.01	13.89
100	17a	28.07	853.81	1193.32	1215.78	0.082	0.079	0.080	9.74	11.68	11.47
100	17a	61.93	834.15	1178.84	1205.23	0.080	0.081	0.079	9.83	11.84	11.59
110	3	70.53	0.0	0.0	0.0	0.0	0.0	0.0	17.72	26.58	26.36
110	3	109.47	502.38	715.90	750.48	0.059	0.060	0.063	14.46	18.82	17.86
110	9	38.94	769.05	1078.91	1180.70	0.071	0.073	0.070	11.19	13.64	12.75
110	9	141.06	540.48	751.65	795.80	0.061	0.058	0.064	13.52	17.25	16.69
110	11	50.48	642.26	907.64	924.01	0.064	0.065	0.062	12.42	15.32	14.97
110	11	129.52	280.95	401.05	420.95	0.043	0.045	0.044	16.03	22.35	21.56
110	17b	86.63	497.62	692.22	713.57	0.038	0.036	0.037	15.18	19.92	18.78
110	17b	93.37	538.10	748.21	780.34	0.048	0.047	0.047	14.34	18.30	17.37
110	19a	26.53	766.65	1081.84	1102.21	0.072	0.074	0.071	11.13	13.64	13.19
110	19a	153.47	633.34	895.22	913.64	0.069	0.071	0.067	12.43	15.52	15.15

It should also be noted that for all boundaries in Cu, our calculated grain boundary energies and volume expansions are very close to the values predicted by Yip and Wolf [1989]. Our calculated grain boundary energy for several boundaries in Ni and Ni_3Al agrees well with the values obtained by Chen et al. [1986] and Baskes et al. [1989].

A linear relationship between grain boundary energy and volume expansion was observed for Cu, Ni and Ni_3Al as shown in Figures 5.2(a), (b) and (c). It should be noted that many material properties correlate directly or inversely with the grain boundary energy. A linear relationship between the boundary energy and volume expansion suggests that many grain boundary related material properties can be easily correlated with the average volume expansions of the boundaries constituting a polycrystal. A trend of increasing grain boundary energy and free volume with an increase in the interplanar period was observed. The grain boundary energy and volume expansion as a function of misorientation showed sharp minima (or cusps) at those values of misorientation angles which left the boundary in purely symmetric configurations. These results agree with the calculations made by Yip and Wolf [1989].

These results indicate that the agreement between our calculations and others is quite good and again gives us confidence in the reliability of our grain boundary model to make further modeling and predication for our purposes.

Because the propensity of Ni_3Al to intergranular fracture could be attributed to a low cohesive energy of the grain boundaries, it is of interest to investigate the energetics of the grain boundary for this alloy. The cohesive energy represents the energy required to cleave the boundary. It is therefore the sum of the surface energy of the two free surfaces that are created minus the energy of the grain boundary which is cleaved when the intergranular fracture occurs in the absence of plastic deformation (Equation 3.34). For the symmetric twist grain boundary, the surfaces created have the same orientation as the grain boundary plane. However, for the symmetric tilt grain boundary; the surfaces created have a different orientation from the grain boundary plane. For Ni_3Al alloy the surface energy depends on whether the exposed surface

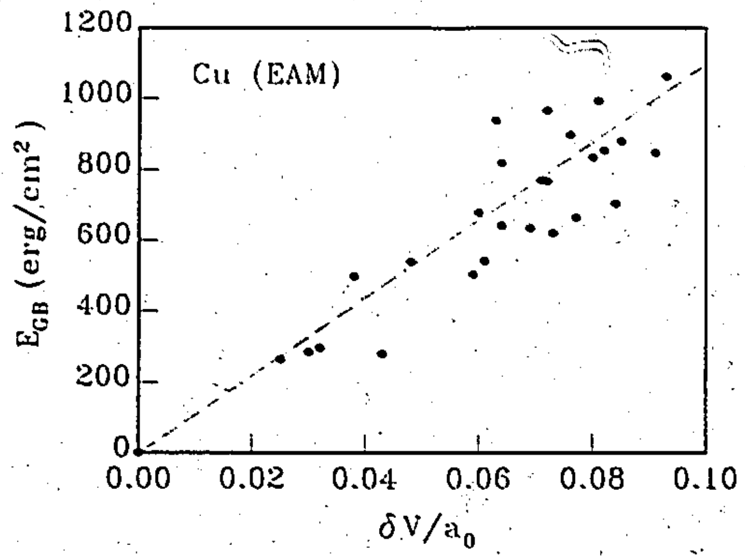

Figure 5.2(a) Relationship between grain boundary energy E_{GB} and volume expansion $\delta V/a_0$ for Cu.

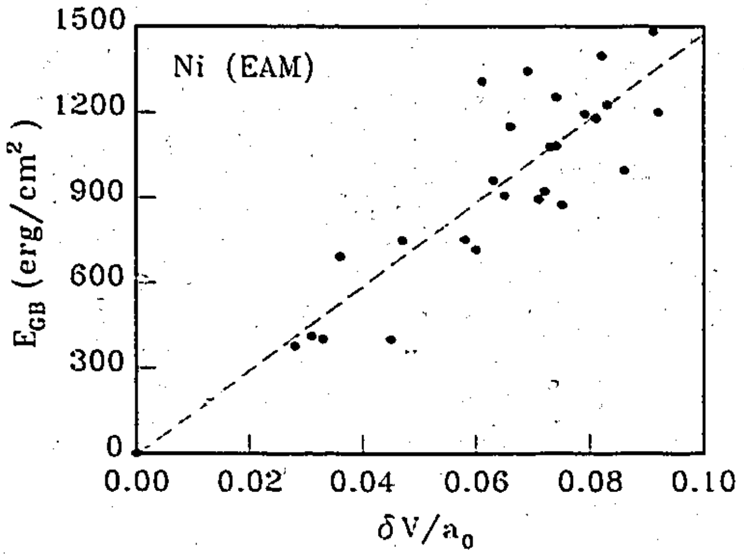

Figure 5.2(b) Relationship between grain boundary energy E_{GB} and volume expansion $\delta V/a_0$ for Ni.

plane is the pure Ni plane, or pure Al plane, or the mixed composition plane which is listed in Tables 3.4 and 3.5.

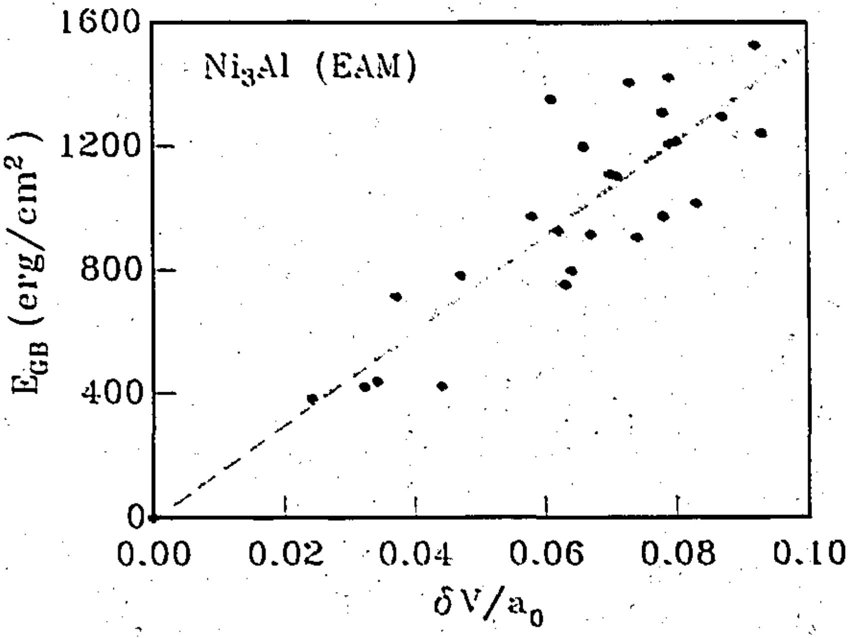

Figure 5.2(c) Relationship between grain boundary energy E_{GB} and volume expansion $\delta V/a_0$ for Ni$_3$Al.

5.1.2. Surface Energy

In this investigation, surface energies were calculated for only three principal fcc surfaces (100), (110) and (111) using the embedded-atom method in Cu, Ni and Ni$_3$Al. Metal surfaces have provided a convenient proving ground for the embedded atom method. Enough accurate measurements are available for some fundamental properties (for example, surface relaxations) that close comparison to experiment is possible. The EAM is seen to be capable of describing metal surfaces adequately because the effective interatomic interactions are influenced by the environment. The key here is the role of the many-body interactions incorporated in the model.

The surface energy and structure of the low-index surface (100), (110) and (111) of Cu, Ni and Ni_3Al were obtained. The calculations were performed by minimizing the total energy of thick slabs with (100), (110) and (111) surfaces.

The results for the surface energies are presented in Table 5.3. In general, the surface energies are systematically lower than the experimental results [Tyson and Miller 1977], though the ordering with respect to face is correct. The error in the absolute surface energy can be traced back to a neglect of the slope of the background density experienced by the surface atoms [Daw 1989].

From Table 5.2, for pure Cu and Ni, (111) surface has the lowest surface energy and (110) has the highest surface energy. For Ni_3Al alloy, mixed (100) surface has the lowest surface energy, (111) has the second lowest, and pure Ni (110) has the highest surface energy. According to Wolf's [1990] calculation the surface energies of other surface planes are between the lowest and highest. These surface energies can be estimated from Figure 5.3.

5.1.3. Summary

The results of grain boundary energy and surface energy indicate that the cohesive energy of grain boundaries in Ni_3Al alloy is not significantly different from pure Ni, which implies that the tendency to intergranular fracture is not simply due to poor cohesion of the individual boundaries. Similar results have been obtained from calculations performed by Chen et al. [1986] and [Baskes et al. 1989]. Therefore, further modeling and calculations are necessary to seek the main reasons of the brittleness of Ni_3Al and to improve its fracture resistance and toughness.

Table 5.3 Experimental average surface energy [Tyson and Miller 1977] and calculated surface energies of three principal fcc surfaces for Cu, Ni and Ni$_3$Al (EAM).

γ (ergs/cm^2)					
Materials		(100)	(110)	(111)	Experimental (average face)
Cu		1288.17	1307.81	1103.42	1790
Ni		1795.97	1820.72	1573.26	2380
Ni$_3$Al	Pure Ni	1895.44	1936.52	1676.31	/
	Pure Al	1821.76	1865.30		
	Mixed	1641.87	1743.04		

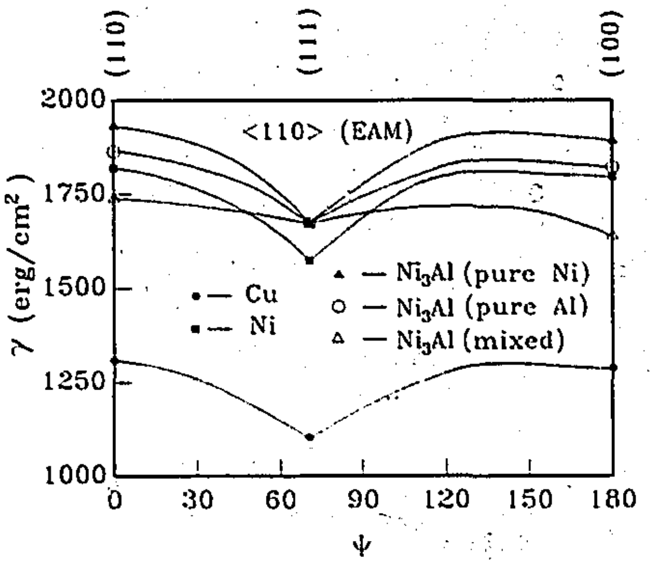

Figure 5.3 Surface energy for surfaces with normals perpendicular to <110>. ψ is the rotation angle about the pole axis.

5.2. Intergranular Fracture at Atomistic Level

5.2.1. System Equilibrium

The system equilibration was investigated by running molecular dynamics simulation at room temperature in the absence of an applied load. The simulation extended to 4,000 time steps in order to bring the system to the equilibrium lattice constant at the specified target temperature. Because the atom velocities were initialized at random according to the desired temperature, the extra thermal energy of some atoms is converted into stress, which is communicated to the borders and causes them to expand or contract. As a result, the atom velocities (temperature) and border positions begin to oscillate out of phase with each other in time until all atoms and borders reach equilibrium. Figure 5.4 illustrates the typical approach to the equilibrium cell length in z direction at room temperature without external stress applied during the equilibrium process. The cell length in z direction versus time step curve takes the form of an exponential decay as expected from the formulation of the model, and it was determined that 4,000 equilibration time steps would be adequate for all grain boundaries which were investigated in this project.

Stress-strain simulations were conducted for each of the grain boundaries at room temperature using the molecular dynamics technique. The runs were conducted on two-dimensional periodic cells with external loads placed along the non-periodic direction (z-axis). The load was applied by assigning external forces to the z-borders and the atoms in Crystals I and II (Figure 3.5) and slowly increasing the force linearly with time.

The principal results of these dynamics simulations are manifested in a stress-strain-to-fracture curve for each run. An example of this output is also given in Figure 5.4 in which the time dependent total length of the computation cell in z direction is plotted as a function of the time step number. Since the applied stress is ramping linearly with time, the plot contains all the information of a conventional engineering stress-strain curve and is easy to convert into a true-stress versus true-strain curve. The statistical fluctuation seen in the curves results from the fact that the system is still not large enough. However, as we can see from this curve, the statistical noise does not make it difficult for us to determine the properties of bicrystal under the applied load. The elastic properties and fracture resistance can easily be estimated from the stress-strain-to-fracture curve.

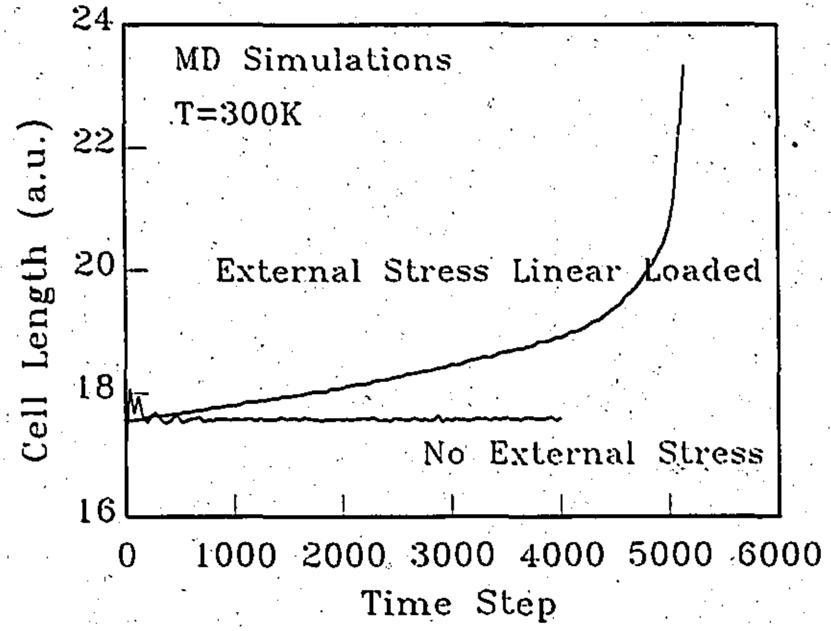

Figure 5.4 Typical cell length changes in z direction with or without external stress loaded during Molecular dynamics simulations at 300 K.

As expected, following an initial period of 4,000 steps used for system equilibration in the absence of external stress, the cell length curve proceeds in time to the point of fracture. Because at the beginning of the simulations, the cell length changes linearly with the time step, plots of this type were used to determine an average Young's modulus for each run, and to verify that the basic operation of the simulation was proceeding as expected.

5.2.2 Verification of Young's Modulus

Important aspects of the verification of the simulation's basic operation are the relative insensitivity of the overall results to variations in the selected time step and force step increments. Simulations were made for the copper sample at 300 K, the force rate being halved at constant step length, and the step length was halved at constant force rate. In each case the resulting value of the Young's modulus for the cell was used for comparison and found to be insensitive to the values selected for either parameter. As shown in Table 5.4, values of the modulus changed by only 5 GPa (<4%) when the step length and force rate were modified. This value is well within the error caused by the statistical fluctuations in the stress and strain curves.

Table 5.4 Computation of Young's Modulus with variation of Force Rate and Time Step in Cu.

Time Step	Force Ramp Rate (10^{-5}eV/Å^3)	Modulus (GPa)
2000	2.5	134.16
2000	2.0	133.65
3000	2.0	130.79
3000	1.5	127.94
Experimental value*		129.45

* Obtained from Smith [1976].

5.2.3. Evolution of Atomistic Image and Stress-Strain Curve

For the purpose of investigating intergranular embrittlement in pure metal and simple alloy, the most important aspect of computer simulation is to guarantee a consistent occurrence of failure on the grain boundary. The cases which failed far away from the boundary are harder to interpret because the grain boundary is the only defect for bicrystal in pure metal and simple alloy and there is no segregated impurity (such as B that could enhance grain boundary) existing in the system. This is also a way to verify the operation of simulation. In our investigation all cases of fracture in bicrystal occur on the grain boundary. Figure 5.5 shows the stress-strain curve for $\Sigma5$ (120) symmetrical boundary in Ni_3Al alloy. Figures 5.6(a)-(f) illustrate structure of the grain boundary images of deformation and fracture behavior for symmetric tilt $\Sigma5(210)$ Ni_3Al boundary. In the figures the small balls represent Ni and the large balls represent Al. Figures 5.6(a)-(f) correspond to the a-f status in Fig.5.5.

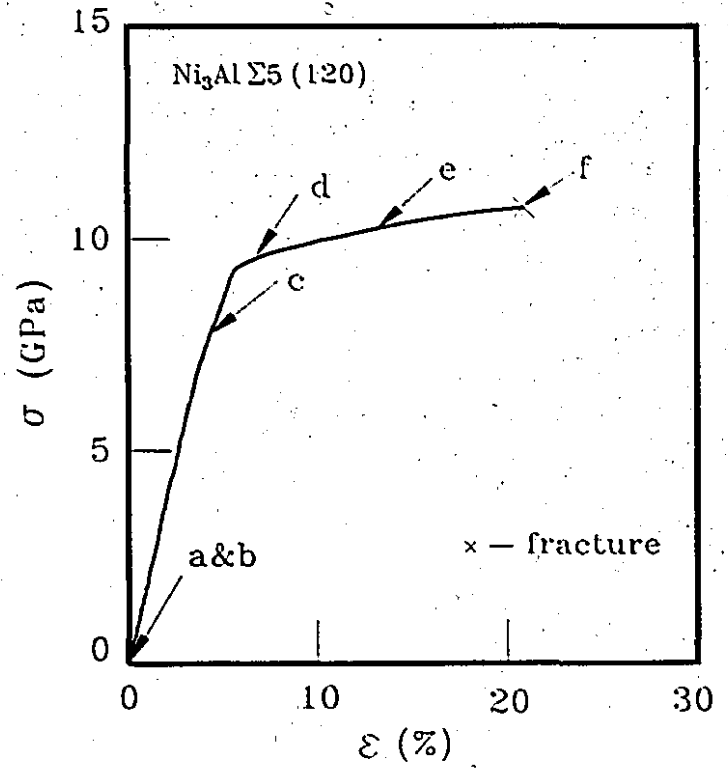

Figure 5.5 Stress-strain curve for $\Sigma5$ (120) symmetric boundary in Ni_3Al alloy. (a-f) corresponds with the image structure in Figure 5.6(a)-(f).

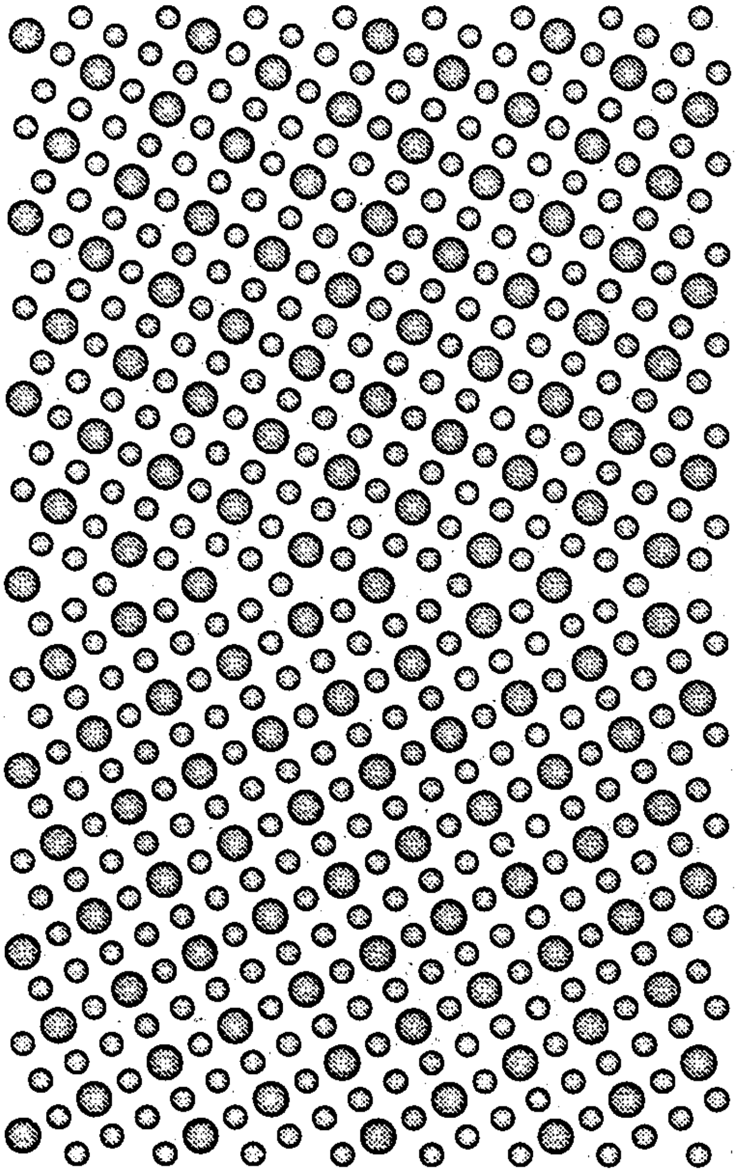

Figure 5.6(a) The relaxed structure of Σ5 (120) symmetrical tilt grain boundary in Ni_3Al. Ni - small balls; Al - large balls.

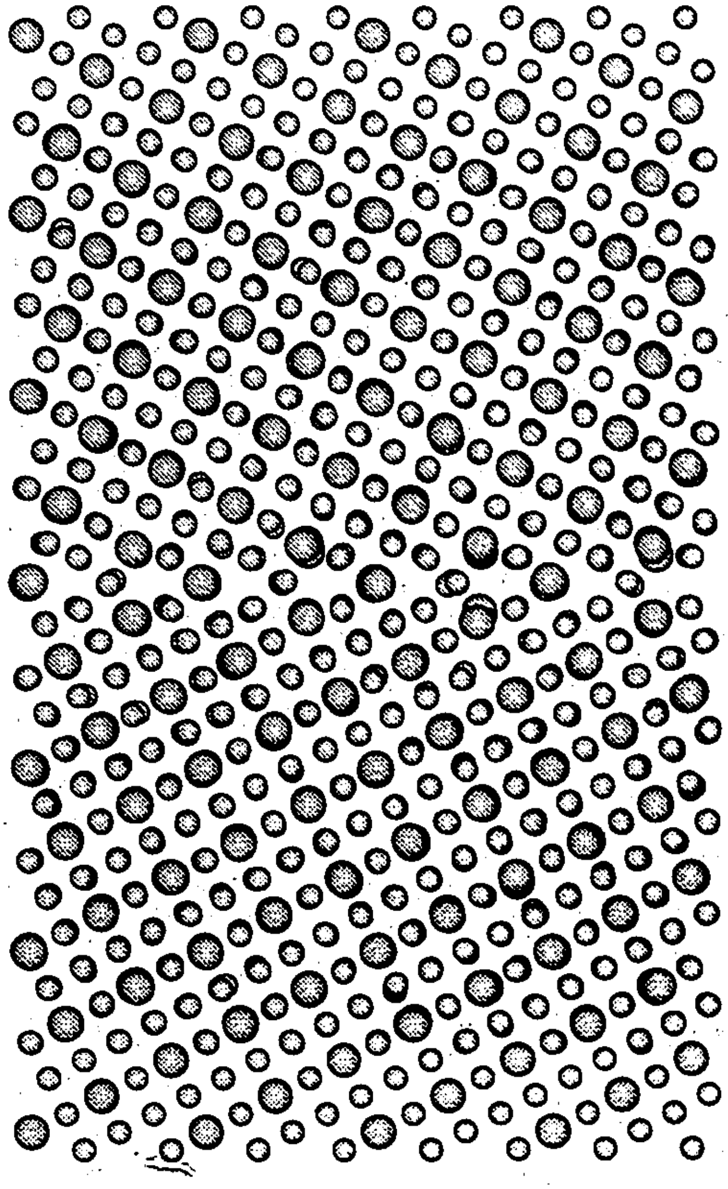

Figure 5.6(b) The dynamics structure of $\Sigma 5$ (120) symmetrical tilt grain boundary at 300 K without applied stress in Ni_3Al.

Ni - small balls; Al - large balls.

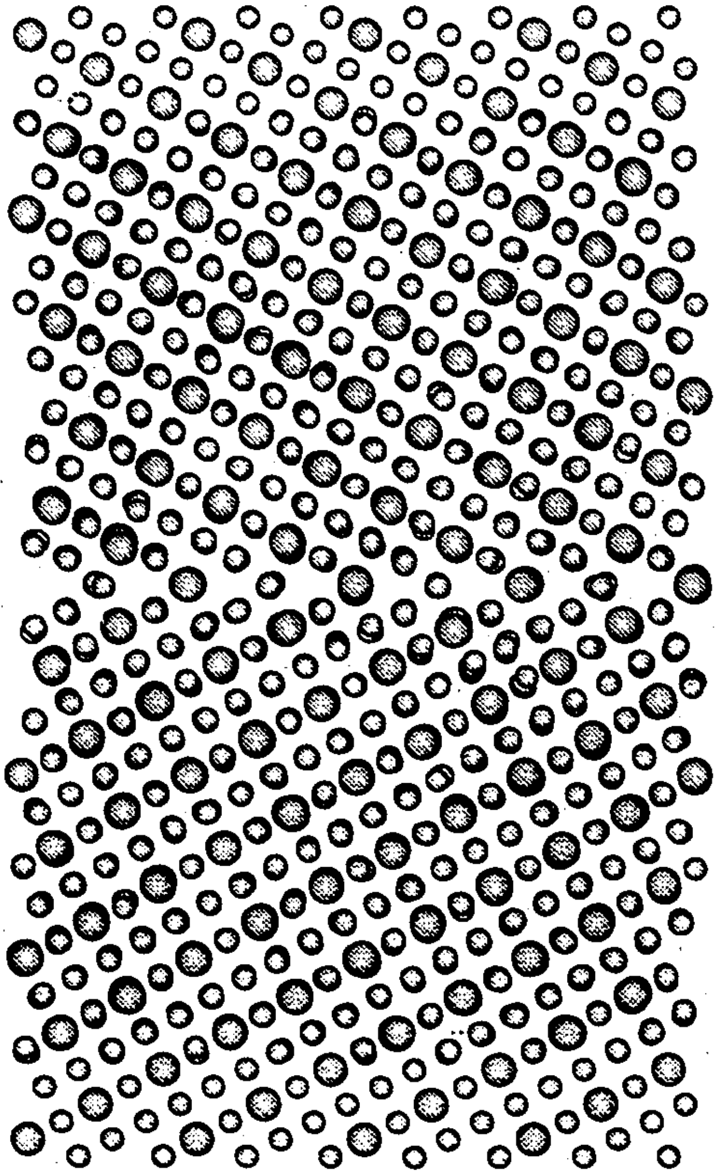

Figure 5.6(c) The structure image with elastic deformation for $\Sigma 5$ (120) symmetrical tilt grain boundary in Ni_3Al.

(c) corresponds to the status in the Figure 5.5.

Ni - small balls; Al - large balls.

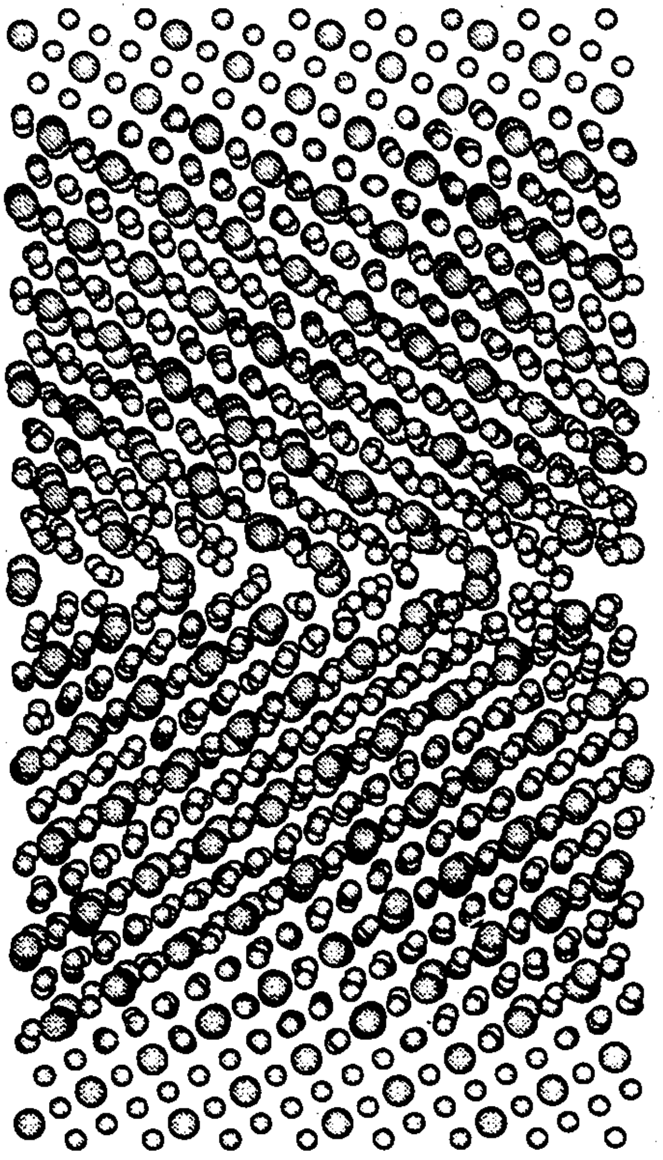

Figure 5.6(d) The structure image for $\Sigma 5$ (120) symmetrical tilt grain boundary in Ni_3Al.

(d) corresponds to the status in the Figure 5.5.

Ni - small balls; Al - large balls.

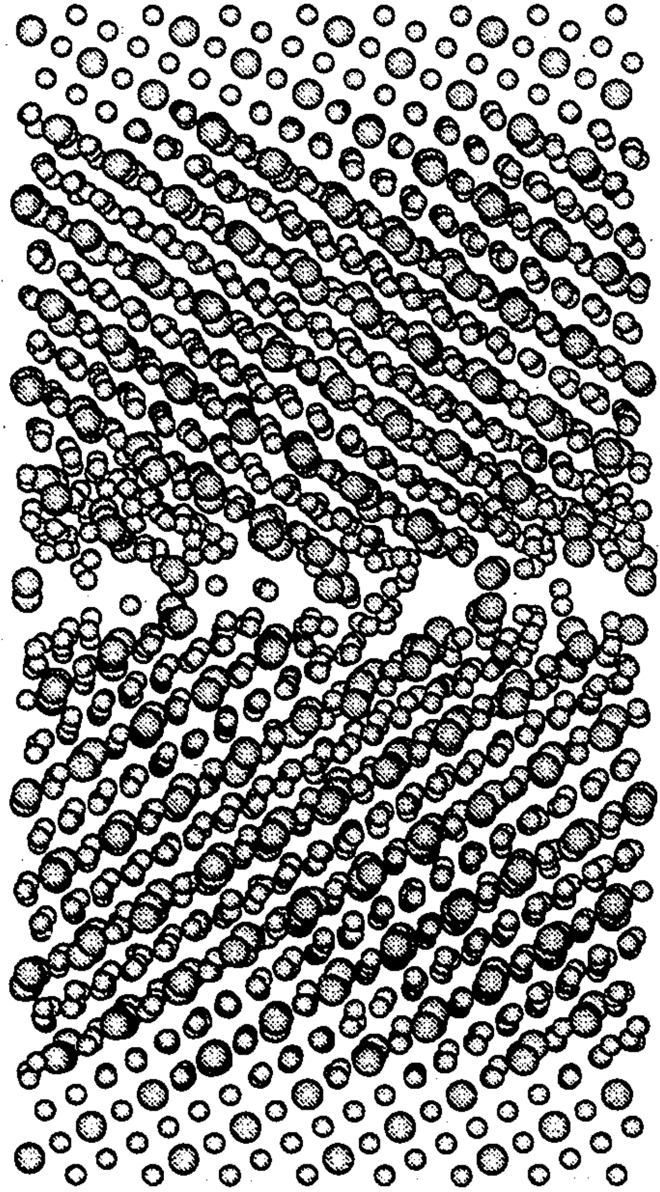

Figure 5.6(e) The structure image with plastic deformation for $\Sigma 5$ (120) symmetrical tilt grain boundary in Ni_3Al.

(e) corresponds to the status in the Figure 5.5.

Ni - small balls; Al - large balls.

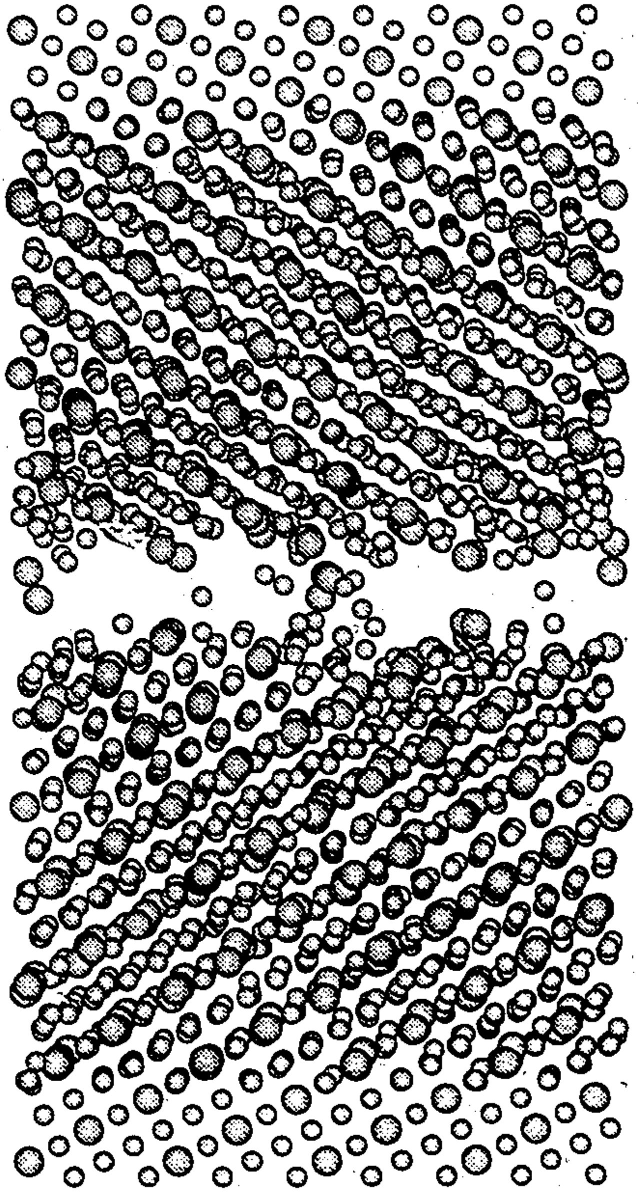

Figure 5.6(f) The structure image after fracture for $\Sigma 5$ (120) symmetrical tilt grain boundary in Ni_3Al.

(f) corresponds to the status in the Figure 5.5.

Ni - small balls; Al - large balls.

As we can see from Figure 5.5, at the beginning of the stress-strain curve the stress increases linearly with the strain, which means that at this stage only elastic deformation occurs in the sample. When the applied stress becomes much greater and is beyond the yield point of materials, the strain increases dramatically with only a small increase in applied stress until the fracture happens.

Figure 5.6(a) shows the relaxed structure for $\Sigma 5$ (120) symmetric boundary in Ni_3Al alloy. It is easy to see that the basic crystal structure exists in the bulk and that a $\Sigma=5$ CSL tilt symmetric boundary structure repeats along the grain boundary plane. Thus, the grain boundary structures predicted by the steepest-descent energy minimization technique using the embedded-atom method potential are very consistent with our previous calculations and others' predictions. Figure 5.6(b) shows the dynamics structure image of $\Sigma 5$ (120) symmetrical boundary in Ni_3Al alloy at 300K without external stress after a total of 4,000 time steps. Compared with the relaxed structure in Figure 5.6(a) it clearly indicates that the basic fcc crystal structure and $\Sigma 5$ CSL tilt symmetric boundary still exist. This means that the grain boundary structures predicted by our molecular dynamics techniques using the same embedded-atom method potential are also very consistent. The next graph (Figure 5.6(c)) shows the structure image with large elastic deformation for $\Sigma 5$ (120) symmetric boundary in Ni_3Al alloy at 300K, which corresponds to stage (c) in Figure 5.5. There is no significant difference between this structure image and the previous one. One notes only that the distance between atoms along the direction perpendicular to the grain boundary plane increases, and the basic fcc crystal structure and $\Sigma 5$ CSL tilt symmetric boundary still exists. Figure 5.6(d) shows the structure image at the beginning of elastic plastic deformation for $\Sigma 5$ (120) symmetric boundary in Ni_3Al alloy at 300K, which corresponds to stage (d) in Figure 5.5. It is evident that the fracture occurs at the core of the grain boundary, and that the basic fcc crystal structure and CSL boundary structure disappear at the grain boundary. The atomic structures looks disordered and a high level of deformation appears in the sample. Far away from the grain boundary plane one still can find the basic fcc crystal structure. The next graph (Figure 5.6(e)) shows the structure image with a much higher plastic deformation for $\Sigma 5$ (120) symmetric boundary in Ni_3Al alloy at 300K which corresponds to stage (e) in Figure 5.5. One can see that the separation of the grain boundary grows larger and the atomic structure becomes more disordered. The final graph (Figure 5.6(f)) shows the structure image when the fracture occurs for $\Sigma 5$ (120) symmetric boundary in Ni_3Al alloy at 300K, which corresponds to stage (f) in Figure 5.5. When the fracture occurs the interaction between two bi-crystals is zero. We identify the end of the fracture when the interaction between two bi-crystals is zero. At this time, however, the strain increases very quickly with only a small increase in applied stress. Because of this behavior of stress-strain it is not easy to determine the exact strain at the fracture point, but the fracture stress can be estimated with sufficient accuracy. The maxima of tensile stress for various CSL grain boundaries in Cu, Ni and Ni_3Al are listed in Tables 5.1 and 5.2.

5.2.4. Stress-strain Relationships for CSL Boundaries in Cu, Ni and Ni_3Al

In these cases where fracture occurs consistently at the grain boundary, the fractures for different CSL grain boundaries generally behave similarly until the point where fracture happens. In all cases observed, the stress-strain curves of the grain boundaries are nearly identical. The evolution of the atomistic configuration is also similar throughout the fracture process. Under the influence of external stress, the bi-crystal samples elongate uniformly in the matrix region with a slightly different strain rate at the grain boundary plane. As a strain across the grain boundary is increased, the restoring force is reduced and the grain boundary core separates rapidly. Depending upon the atomistic configuration of the first few boundary planes, the separation may occur in either a clean brittle fashion or one in which bands of material are drawn into the center from either side. Figures 5.7(a), (b) and (c) show the calculated stress-strain curve in Cu for various CSL symmetric twist, <100> tilt and <110> tilt grain boundaries, respectively. One can easily find, that the fracture stress varies for different CSL grain boundaries. For the symmetric

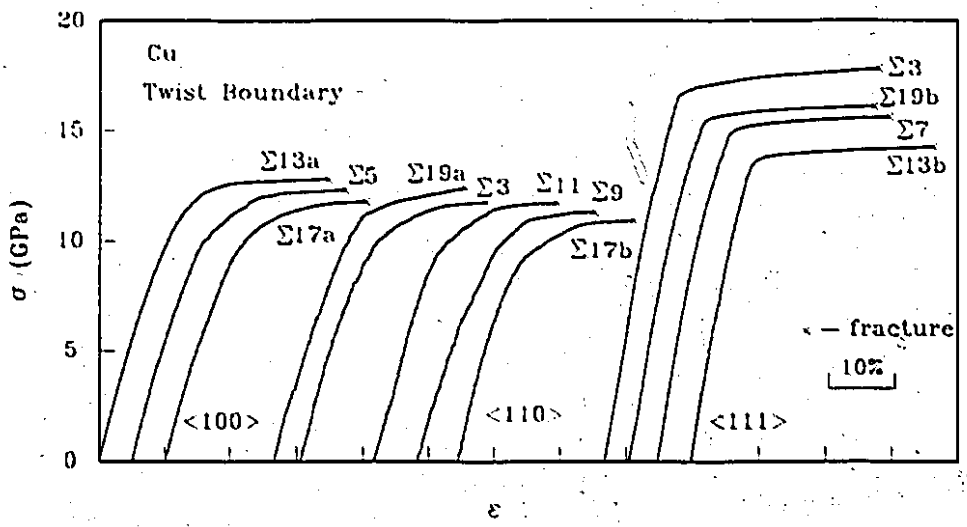

Figure 5.7(a) Stress-strain curves for various symmetric twist grain boundaries in Cu.

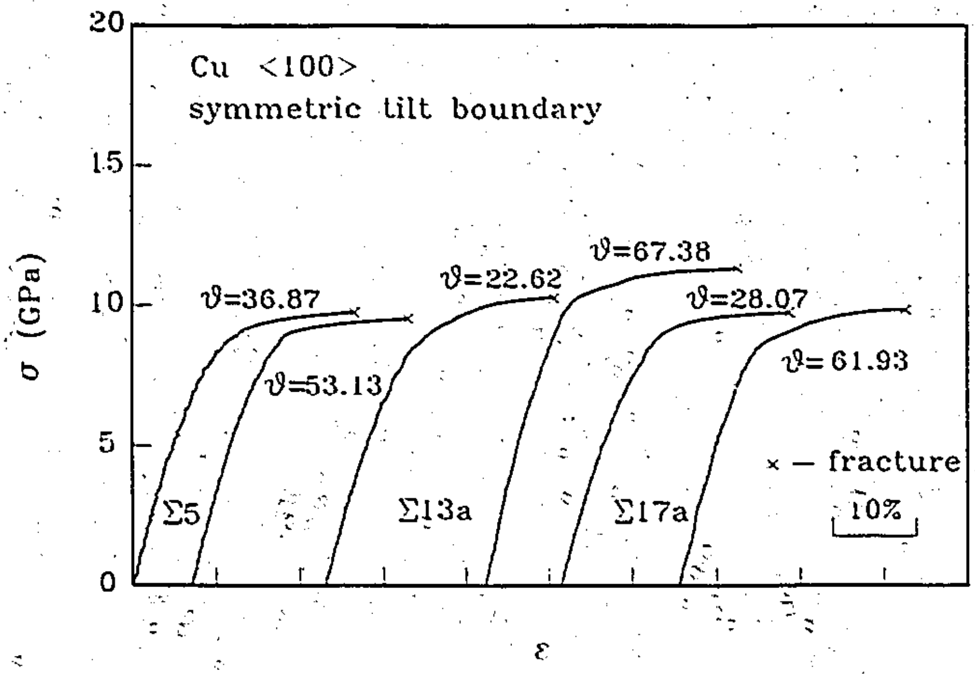

Figure 5.7(b) Stress-strain curves for various <100> symmetric tilt grain boundaries in Cu.

twist boundaries in Cu, the fracture stress of boundaries at <111> plane is much higher than those at <100> and <111> planes. Among these high fracture stress boundaries, the fracture stress of Σ3 twin boundary at <111> plane is the highest, while the fracture stress of Σ3 boundary at <110> plane is much lower. Σ17b boundary at <110> plane has the lowest fracture stress of all calculated symmetric twist boundaries in Cu. The fracture stress (Figure 5.7(b)) of the <100> symmetric tilt boundaries in Cu are low compared to the symmetric twist boundaries. However, for the <110> symmetric tilt boundaries in Cu there are several grain boundaries with much higher fracture stresses. These grain boundaries are Σ3(70.53°), Σ11(129.52°), Σ17b(86.63°), etc. The results also indicate that for tilt grain boundaries with the same Σ values and different misorientation the fracture stresses are totally different. Therefore, the grain boundary fracture stress depends on the type and structure of grain boundary, i.e., the boundary plane and misorientation described, at least, by the crystallographic and geometrical parameters.

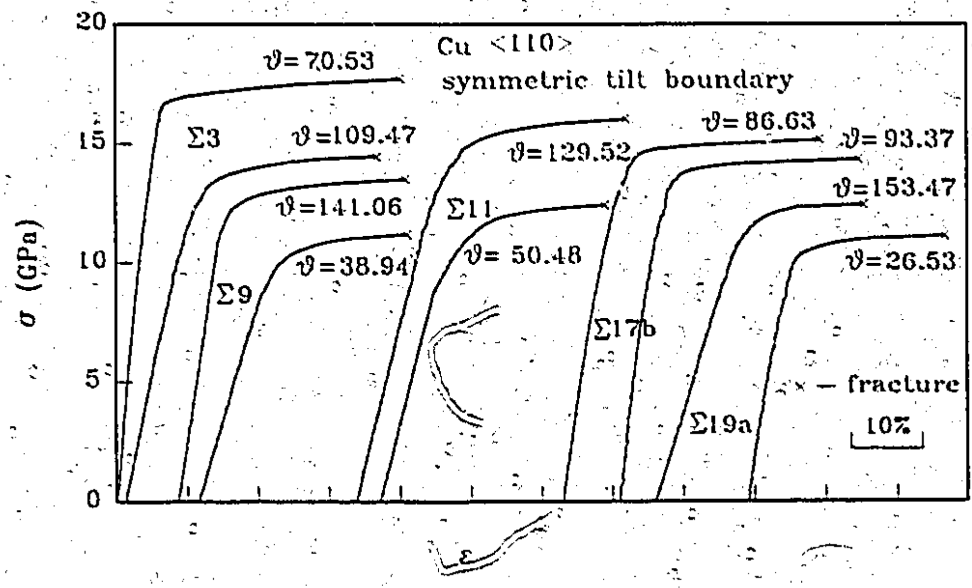

Figure 5.7(c) Stress-strain curves for various <110> symmetric tilt grain boundaries in Cu.

We have conducted the same kind of modeling test for the same grain boundaries in pure Ni metal and Ni_3Al alloy and obtained similar results. The stress-strain curves for symmetric twist boundaries, <100>, and <110> symmetric tilt boundaries in Ni and Ni_3Al are shown in Figures 5.8(a)-(c) and 5.9(a)-(c), respectively. The fracture stresses for various CSL grain boundaries in Ni and Ni_3Al are also listed in Tables 5.1 and 5.2. One may note the fluctuation in all stress-strain curves. Some noises are small while some are quite large. These fluctuations seen in the curves result from two facts: (i) the system size and shape, especially the width of specimen; (ii) the thermal vibration of particles. In our modeling the fluctuation has been minimized through the use of relative large systems and the calculation of true temperature at each step. Even with these efforts the noise is still be observed because the thermal vibration of particles cannot vanish in the molecular dynamics modeling. The noise will be much greater when the temperature is high. Another reason is that the system may still not be large enough to eliminate the size effects [Pontikis 1988]. However, compared with the same kind of fracture dynamics modeling by Smith and Was [1989], our noise is 10-20 times lower. The curves in Simth's and Was's calculations must be plotted separately rather than in the form of a true-stress versus true-strain curve, because the statistical fluctuation of each quantity in time makes the composite σ-ε curve extremely difficult to read. Smith and Was also thought that the statistical noise seen in their curves resulted from the low number of atoms in the system(256 atoms).

The results of stress-strain relationship and fracture stress indicate that the fracture behavior of various CSL grain boundaries in Ni_3Al alloy is not significantly different from those in pure Ni metal. That implies that the tendency to intergranular fracture in Ni_3Al alloy is not due merely to poor fracture resistance of the grain boundaries.

As expected, a linear relationship between the fracture stress and grain boundary energy was found in Cu, Ni and Ni_3Al as shown in Figures 5.10(a), (b) and (c), respectively. Because many material properties correlate directly or inversely with grain boundary energy, a linear relationship between the fracture stress and boundary energy suggests that this relationship can be extended

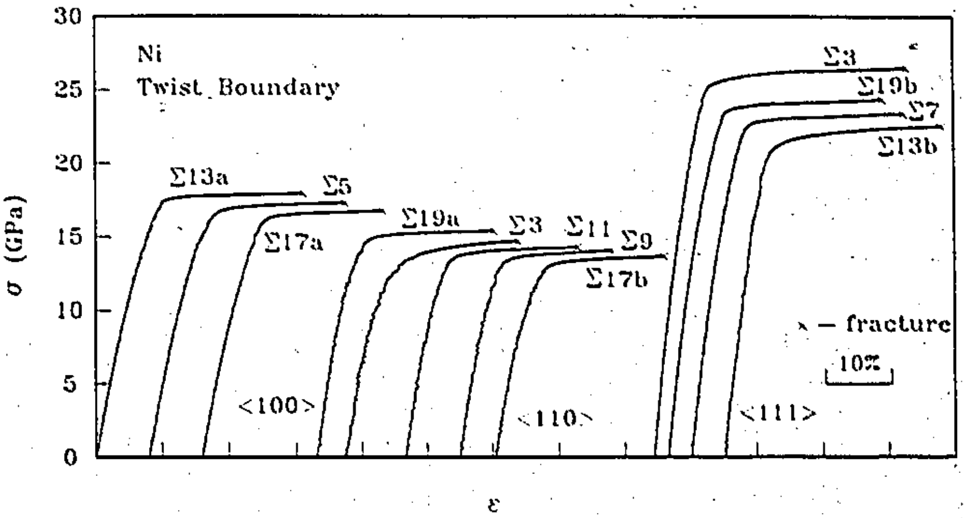

Figure 5.8(a) Stress-strain curves for various symmetric twist grain boundaries in Ni.

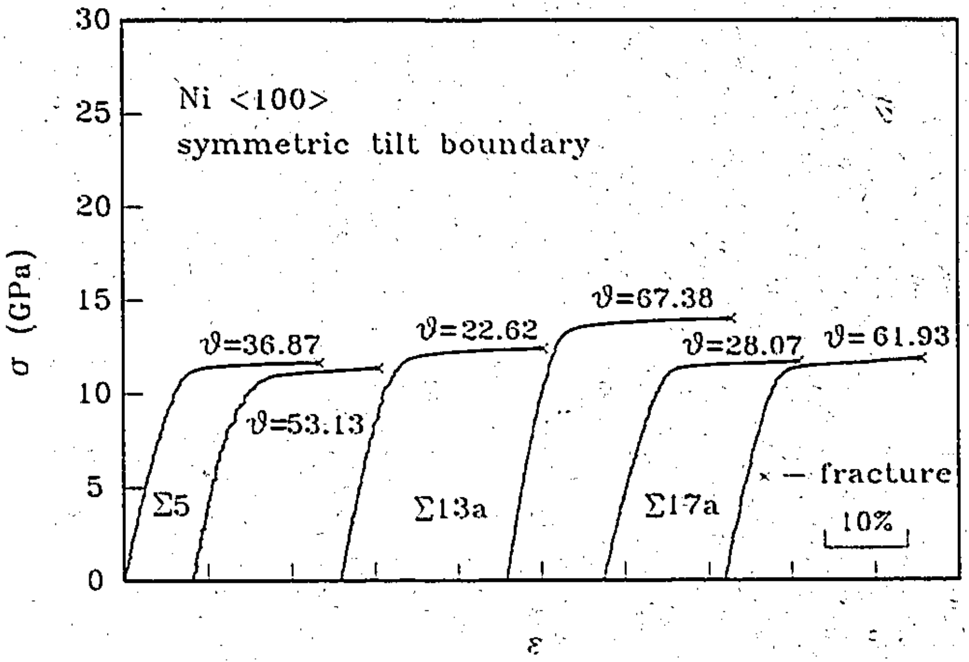

Figure 5.8(b) Stress-strain curves for various <100> symmetric tilt grain boundaries in Ni.

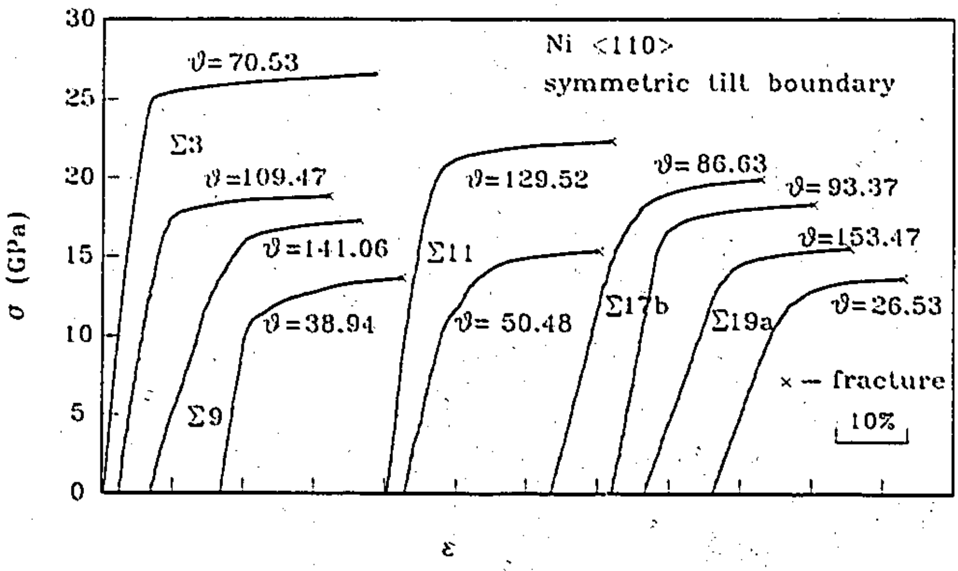

Figure 5.8(c) Stress-strain curves for various <110> symmetric tilt grain boundaries in Ni.

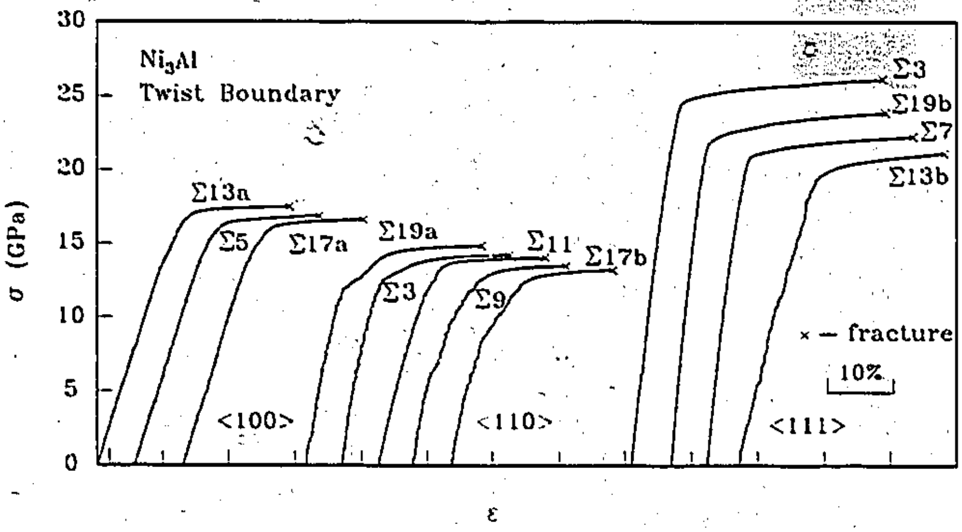

Figure 5.9(a) Stress-strain curves for various symmetric twist grain boundaries in Ni$_3$Al.

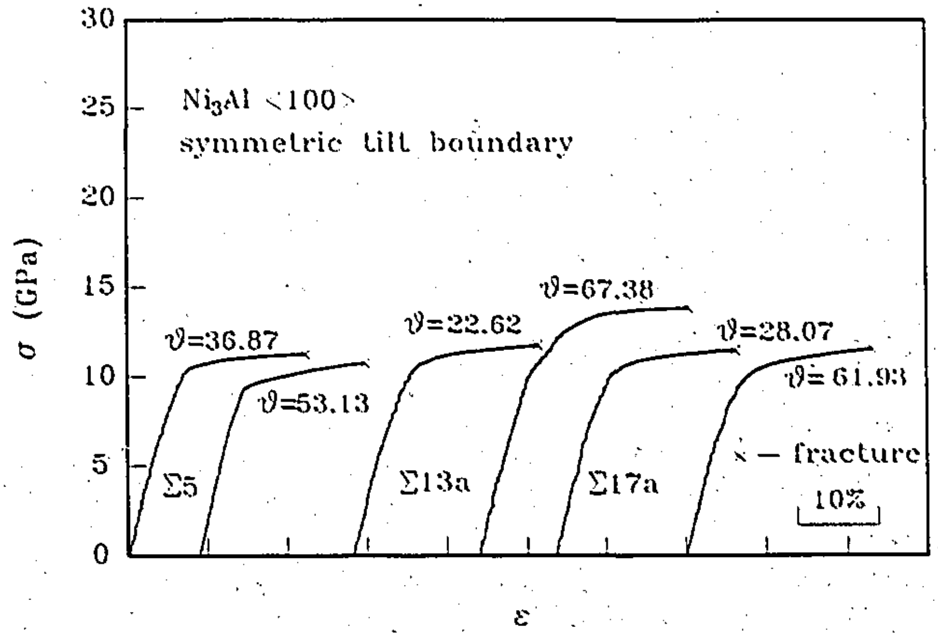

Figure 5.9(b) Stress-strain curves for various <100> symmetric tilt grain boundaries in Ni_3Al.

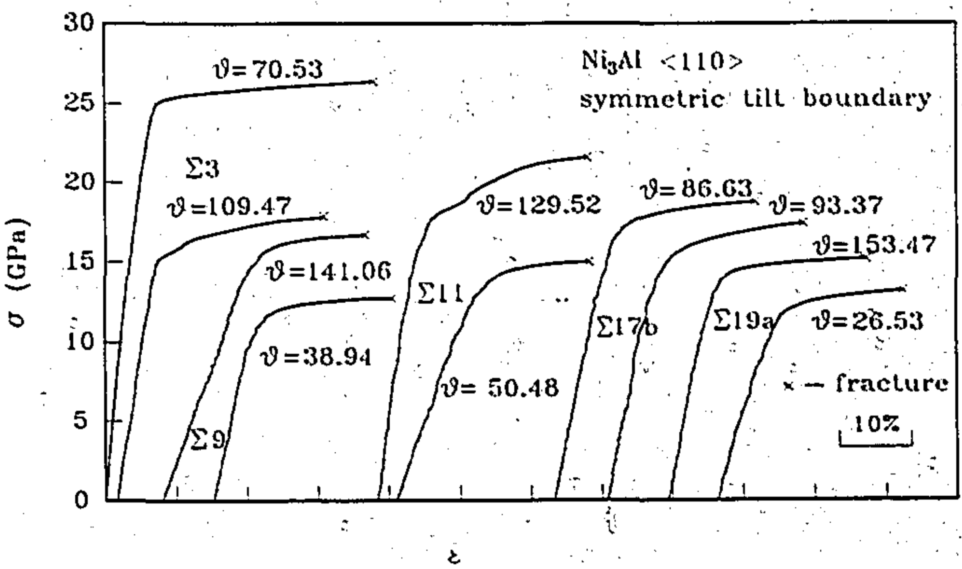

Figure 5.9(c) Stress-strain curves for various <110> symmetric tilt grain boundaries in Ni_3Al.

to the high energy boundaries.

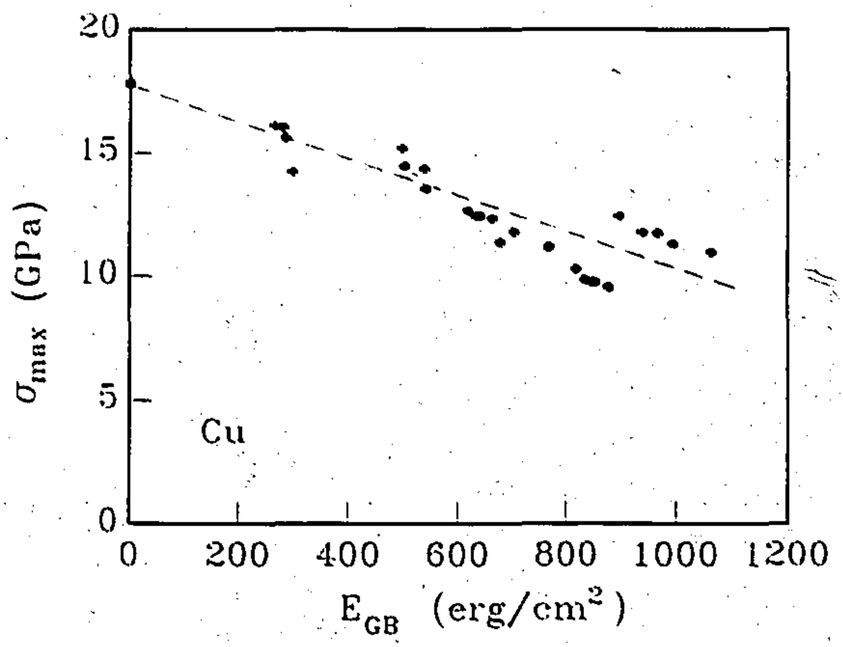

Figure 5.10(a) Relationship between fracture stress and grain boundary energy in Cu.

5.2.4. Anisotropic Fracture Behavior for Perfect Crystals

In order to see anisotropic fracture behavior, the tensile test has been simulated for perfect crystals (Σ1) at three principal axes in Cu, Ni and Ni_3Al. Table 5.5 shows the maximuma of tensile stress and strain at three principal axes in Cu, Ni and Ni_3Al. The results indicate that the fracture behavior in these materials is anisotropic, the <110> axis has the highest fracture resistance and the <111> axis has the lowest fracture stress. These results are supported by surface energy calculations.

5.2.5. Summary

The intergranular fracture behavior has been investigated at the atomistic level for various

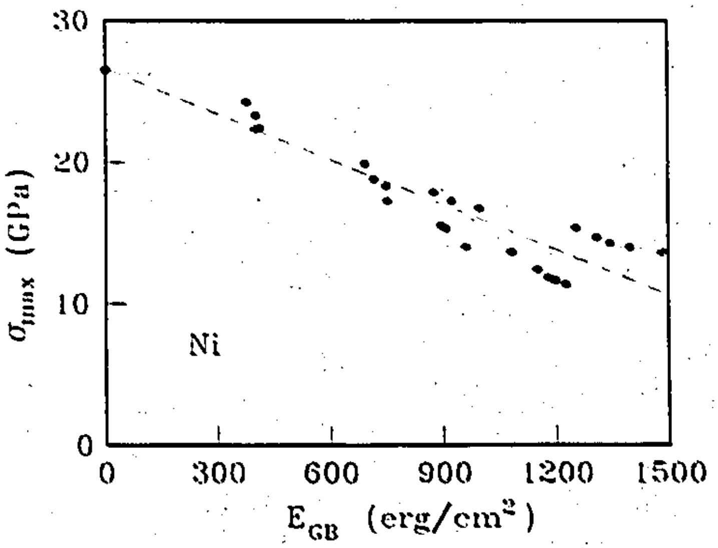

Figure 5.10(b) Relationship between fracture stress and grain boundary energy in Ni.

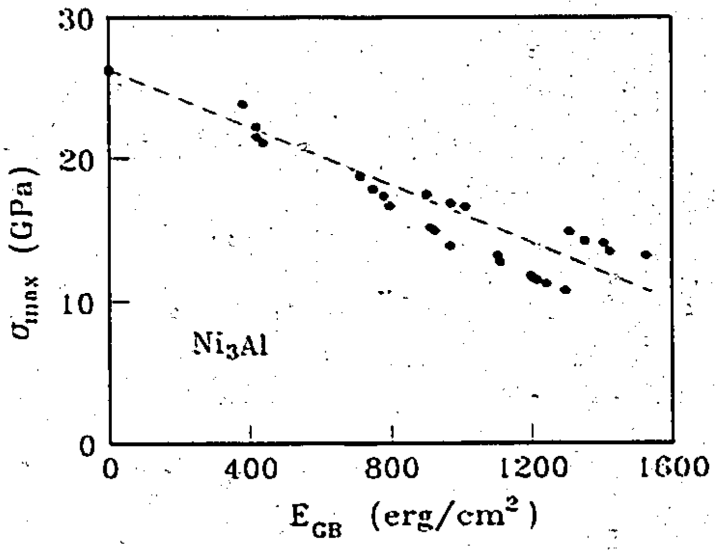

Figure 5.10(c) Relationship between fracture stress and grain boundary energy in Ni_3Al.

twist and tilt CSL grain boundaries in Cu, Ni and Ni_3Al, using the molecular dynamics method. The fracture resistance varies for different grain boundary structures. For the symmetric twist boundaries the fracture stress of boundaries at <111> plane is much higher than those at <100> and <110> planes. Among these high fracture stress boundaries the fracture stress of $\Sigma3$ twin boundary at <111> plane is the highest, while the fracture stress of $\Sigma3$ boundary at <110> plane is much lower. $\Sigma17b$ boundary at <110> plane has the lowest fracture stress of all calculated symmetric twist boundaries. A linear relationship between the fracture stress and grain boundary energy has been found. The results of stress-strain relationship and fracture stress indicate that the fracture behavior of various CSL grain boundaries in Ni_3Al alloy is not significantly different from that in pure Ni metal. This implies that the tendency to intergranular fracture in Ni_3Al alloy is not due merely to poor fracture resistance of the grain boundaries.

Table 5.5 Maximums of tensile stress and strain for perfect crystals at three principal axes for Cu, Ni and Ni_3Al.

	<100>		<110>		<111>	
	σ_{max} (GPa)	ϵ_{max} (%)	σ_{max} (GPa)	ϵ_{max} (%)	σ_{max} (GPa)	ϵ_{max} (%)
Cu	18.30	42.10	18.47	42.53	18.15	42.79
Ni	26.78	39.93	26.83	40.11	26.52	40.53
Ni_3Al	26.74	38.16	26.95	38.32	26.48	38.78

5.3. Comparison of Predictions with Bicrystal Experiments

The dependence of grain boundary structure on intergranular fracture has been studied by many researchers using bicrystals of normally brittle materials such as refractory metals and diamond cubic materials [Lim and Watanabe 1990]. Much careful experimental work on the effect of boundary type and misorientation on intergranular fracture stress has been performed in the last decade, using bicrystal specimens with well-characterized grain boundaries [Watanabe 1993]. For examples, Kurishita et al. [1989] measured the fracture stress of molybdenum bicrystals with <100>, <110> tilt and <110> twist boundaries, while Sato et al. [1989] studied silicon bicrystals containing a <111> twist boundary of different misorientations. For semi-brittle and normally ductile materials such as h.c.p. and f.c.c. metals, the dependence of boundary misorientation on fracture stress has also been studied using liquid metal embrittlement techniques. Notable studies in this respect include work on: $<10\bar{1}0>$ tilt and twist bicrystals of zinc embrittled by liquid gallium [Watanabe et al. 1984], <110> tilt aluminium bicrystals embrittled by liquid Sn-Zn [Otsuki and Mizuno 1986], and the work on the crack extension force for intergranular fracture of <110> tilt aluminium bicrystals embrittled by liquid Hg-Ga [Kargol and Albright 1977].

From these studies, Lim and Watanabe [1990] have made several conclusions. First, the fracture stress or crack extension force of coincidence boundaries (including $\Sigma 1$/low-angle boundaries) is about 2 - 18 times higher than that of high energy random boundary on bicrystals of metals and alloys in different environments. Second, even though the reported fracture stress is found to vary somewhat from one boundary type to another, it is interesting to note that the ratio of the fracture stress of coincidence boundaries to that of random ones (σ_Σ/σ_R) increases with decreasing Σ values, irrespective of test conditions and materials. Lower Σ coincidence boundaries have higher fracture stress. Third, the limited experimental data have indicated a lower σ_Σ/σ_R for twist than for tilt boundaries. This, however, could be attributed to a much higher σ_R for twist boundaries, as indicated by the results of Kurishita et al. [1983]. These results also indicated that the fracture stress for high purity molybdenum bicrystals is high at a misorientation angle smaller than 10° and that corresponding to $\Sigma 3$ coincidence orientation, but much lower than that for low purity bicrystals at a misorientation angle between 20° to 50°. The twist bicrystals showed more significant misorientation effect on the fracture stress, but material purity was observed to have little effect. The difference in misorientation effect, particularly concerning the effect of material purity may suggest that the effect of segregation of impurities on fracture stress may be significant only for the tilt boundaries, probably because they can accommodate impurities more effectively than twist boundaries, as already reported by Watanabe et al. [1980]. It is important to note that the intergranular fracture stress depends to a high degree on the type and misorientation of grain boundary, and that it can also be affected by material purity through the effect of grain boundary segregation. This may be one of the sources of extrinsic intergranular brittleness often observed. It should be noted that low energy boundaries such as low angle and low Σ coincidence boundaries are not good sites for segregation. These boundaries, therefore, are insensitive to material purity, irrespective of their type, i.e., tilt or twist. Polycrystal may contain different types of grain boundaries with different frequencies and geometrical configurations. Structure-dependent intergranular fracture in polycrystalline materials has been observed and well documented. High energy random boundaries are preferential sites for crack nucleation and propagation, but low energy boundaries such as Σ3 would not break even under maximum tensile stress condition.

Figure 5.11 shows the experimental results of crack extension force for symmetric <110> tilt boundaries in pure aluminum embrittled by Hg-3.at pct Ga [Kargol and Albright 1977]. It is noted that near the angles at which crack extension force peaks are found, there are high stability boundaries of 0° and 180° (low angle Σ1 boundaries), and 70° and 130° (corresponding to {111} Σ3 and {113} Σ11 twin boundaries, respectively). At these misorientations the grain boundary energy is also high [Hasson et al. 1972]. This indicates that grain boundary energy plays a role in determining the cracking susceptibility of grain boundaries. This figure verifies that intergranular fracture has a strong dependence on grain boundary type and misorientation.

Figure 5.12(a) and (b) show our calculations of fracture stress in Cu as a function of misorientation for symmetric twist <100>, <110> and <111> boundaries, and symmetric tilt <100> and <110> boundaries, respectively. For symmetric <111> twist boundaries, a high fracture resistance predicted theoretically was found at an angle near 60° which corresponds to

{111} Σ3 twin boundary. The grain boundary energy for this particular boundary is also much lower, shown in Table 5.1. However, there are no other boundaries with high fracture stress found among <100> and <110> twist boundaries, with the exception of low angle Σ1 boundaries. These results are also supported by grain boundary energy calculation, shown in Table 5.1.

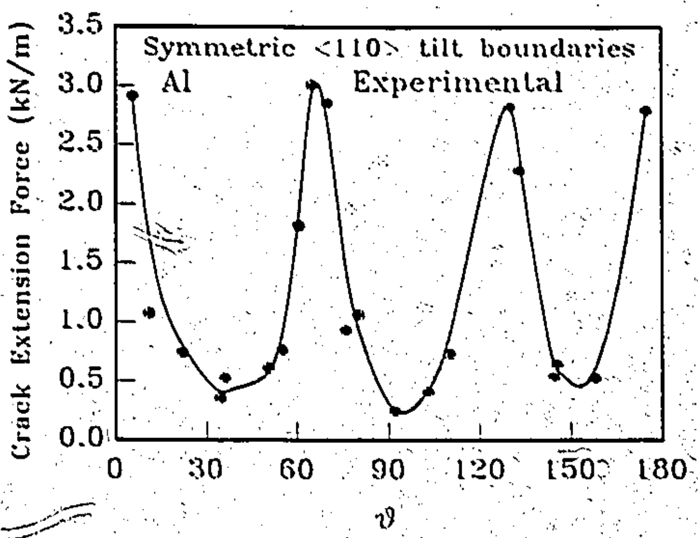

Figure 5.11 Crack extension force of symmetric <110> tilt boundaries for pure aluminum embrittled by Hg-3 at. pct Ga [Kargol and Albright 1977].

Compared to Figure 5.11 for symmetric <110> tilt boundaries, the high crack propagation resistance predicted theoretically was also found to persist experimentally over a wider range of tilt angles near these two (70° and 130° tilt angles) high resistance boundaries. At these misorientations the grain boundaries correspond to {111} Σ3 and {113} Σ11 twin boundaries, respectively. Because of the particularly high stability of boundaries with tilt angles of 70° and 130°, it may be that grain boundaries with orientations near these tilt angles adjust their structures from an ideally planar structure so that their grain boundary energies are lower. The

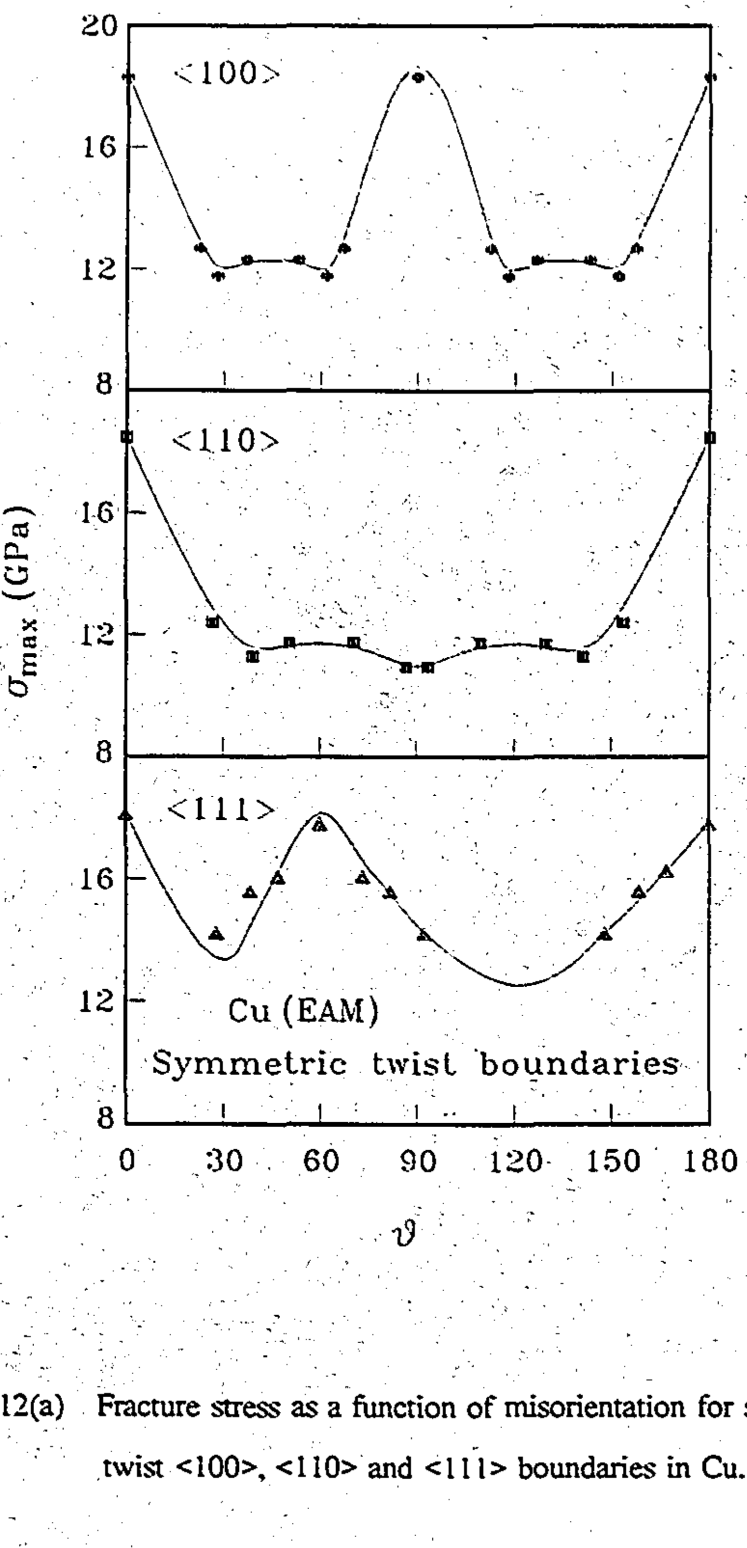

Figure 5.12(a) Fracture stress as a function of misorientation for symmetric twist <100>, <110> and <111> boundaries in Cu.

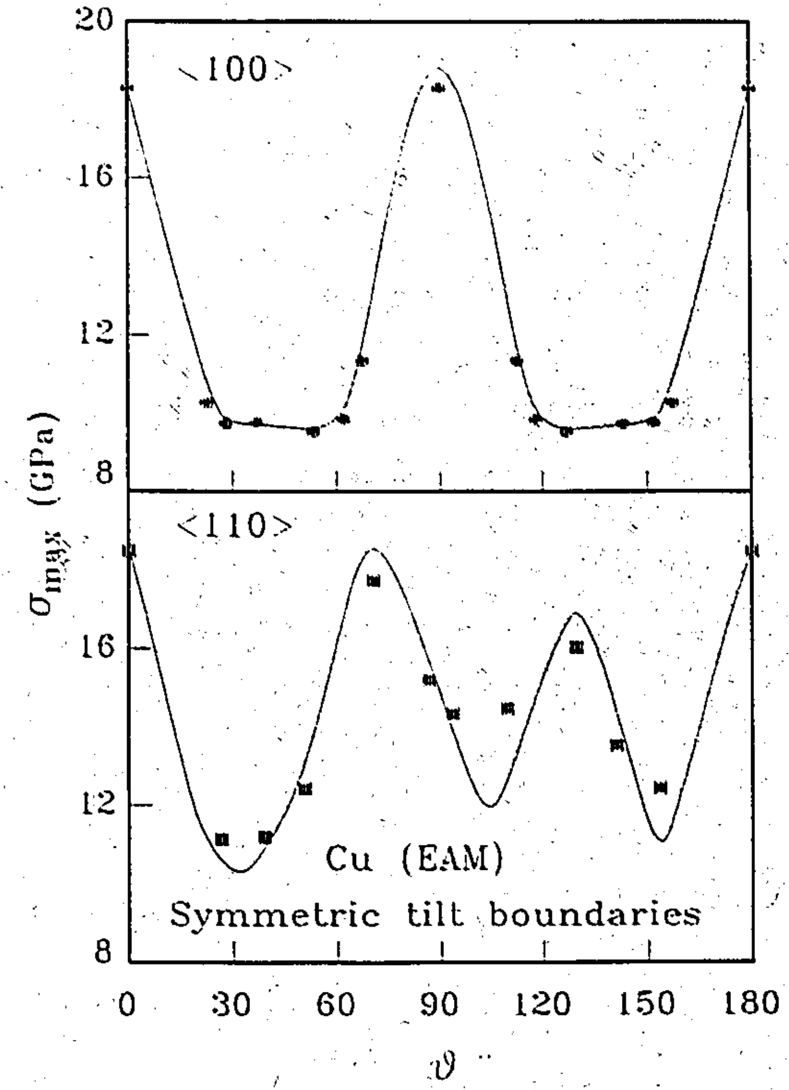

Figure 5.12(b) Fracture stress as a function of misorientation for symmetric tilt <100> and <110> boundaries in Cu.

suggestion of high boundary stability persistence is supported by our calculated variation in grain boundary energy with tilt misorientation angle, shown in Table 5.2. Our calculated results also indicate that the curve shape of our calculated variation in fracture stress for tilt <110> boundaries with a tilt angle is very similar to the experimental results, shown in Figure 5.11, even though different materials are used. There are also no other boundaries with high fracture stress found among tilt <100> boundaries except for low angle $\Sigma 1$ boundaries which are also supported by grain boundary energy calculation, shown in Table 5.2.

It was concluded form our calculations that the embrittlement susceptibility variations of the grain boundaries were controlled by grain boundary fracture stress variations. The crack propagation resistance of a grain boundary was shown to be related qualitatively (linearly) to its grain boundary energy.

Similar results were obtained for Ni metal and Ni_3Al alloy, as shown in Figure 5.13 and 5.14. Figures 5.13(a) and (b) show the calculated fracture stress in Ni as a function of misorientation for symmetric twist <100>, <110> and <111> boundaries, and symmetric tilt <100> and <110> boundaries, respectively. Figures 5.14(a) and (b) show calculated fracture stress in Ni_3Al as a function of misorientation for symmetric twist <100>, <110> and <111> boundaries, and symmetric tilt <100> and <110> boundaries, respectively. A grain boundary with high fracture resistance was found at a twist angle near 60° for symmetric twist <111> boundaries which corresponds to {111} $\Sigma 3$ twin boundary, and two other grain boundaries with high fracture stress were also found near 70° and 130° tilt angles which correspond to {111} $\Sigma 3$ and {113} $\Sigma 11$ twin boundaries, respectively. These results indicate that the fracture stress of grain boundaries in Ni_3Al alloy is not significantly different from that for pure Ni. Similar results and conclusions have been obtained from calculations performed by other researchers [Baskes et al. 1989, Chen et al. 1986]. The reasons may be that because Ni_3Al alloy has the same cubic structure (either intrinsically or through alloying) and a sufficient number of slip systems for generalized deformations as Cu and Ni metals. However. transgranular fracture in Ni_3Al

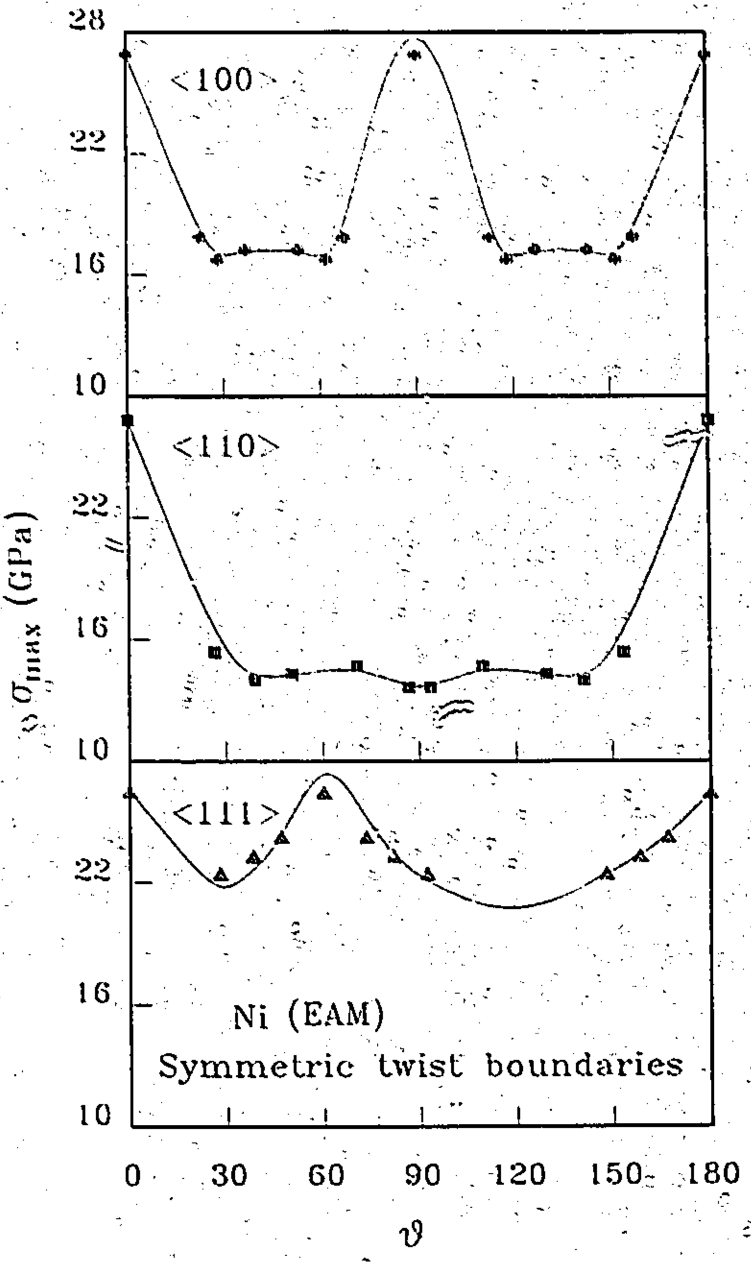

Figure 5.13(a) Fracture stress as a function of misorientation for symmetric twist <100>, <110> and <111> boundaries in Ni.

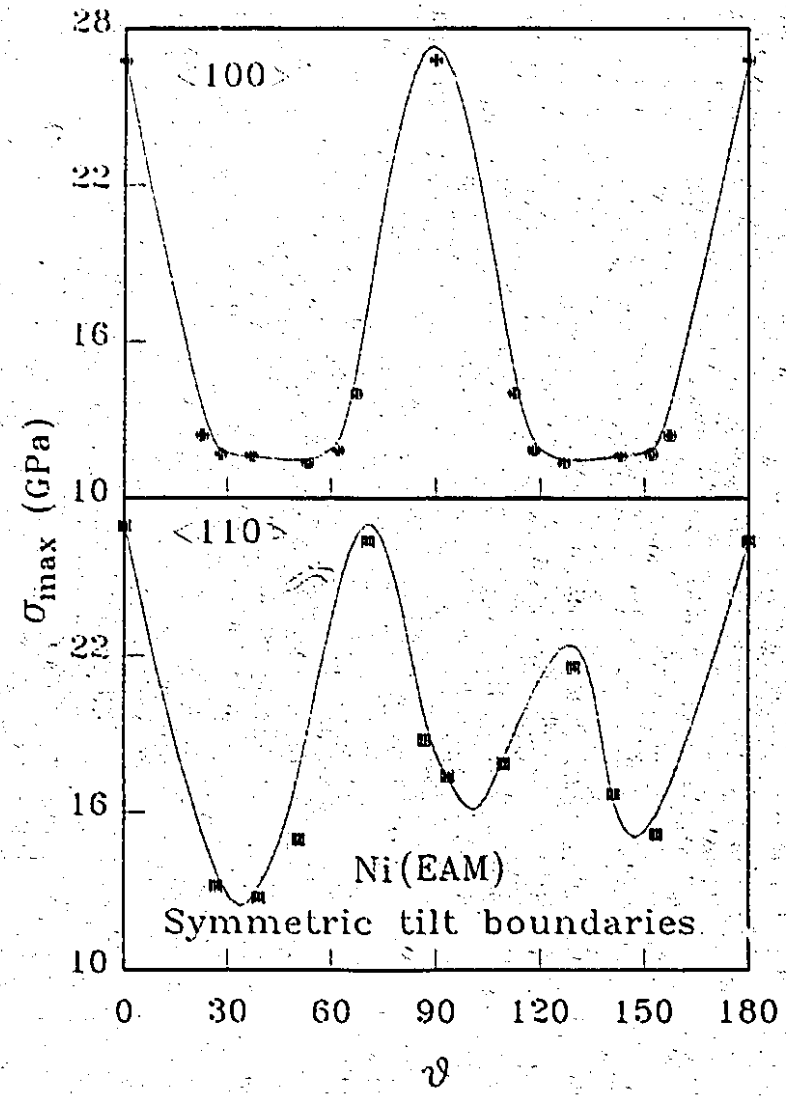

Figure 5.13(b) Fracture stress as a function of misorientation for symmetric tilt <100> and <110> boundaries in Ni.

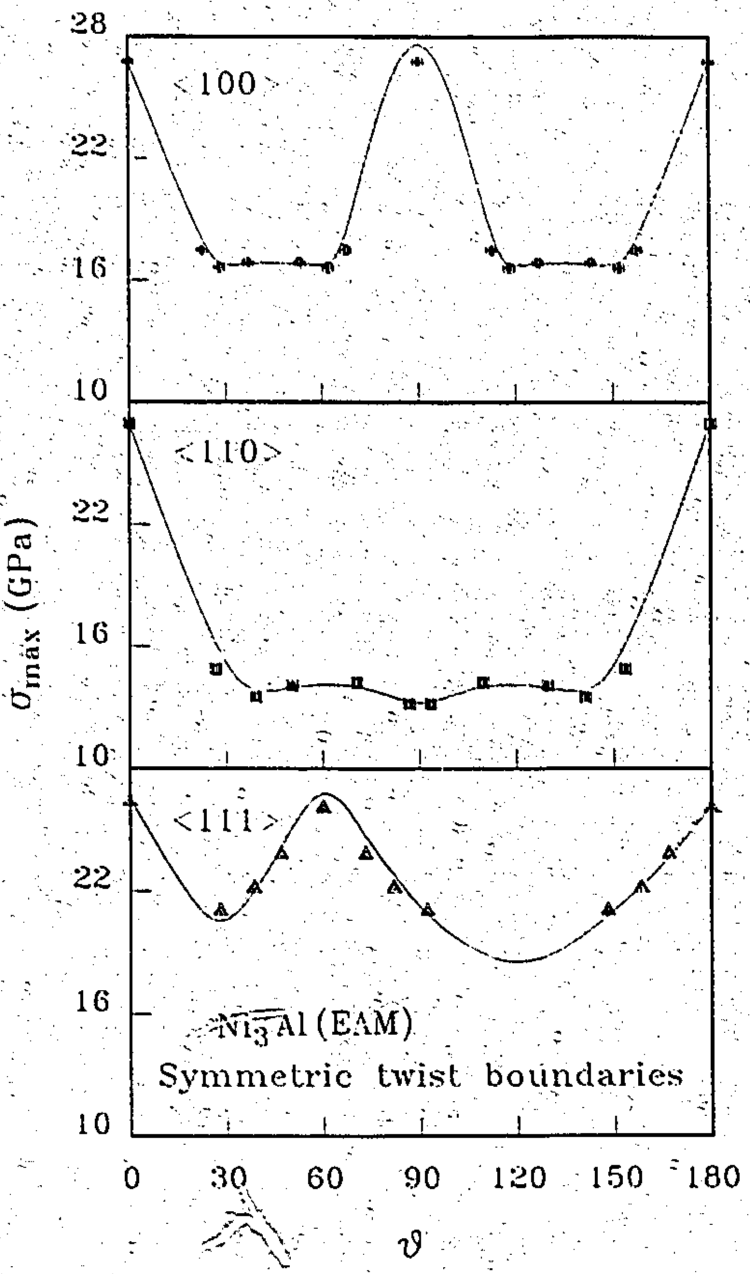

Figure 5.14(a) Fracture stress as a function of misorientation for symmetric twist <100>, <110> and <111> boundaries in Ni$_3$Al.

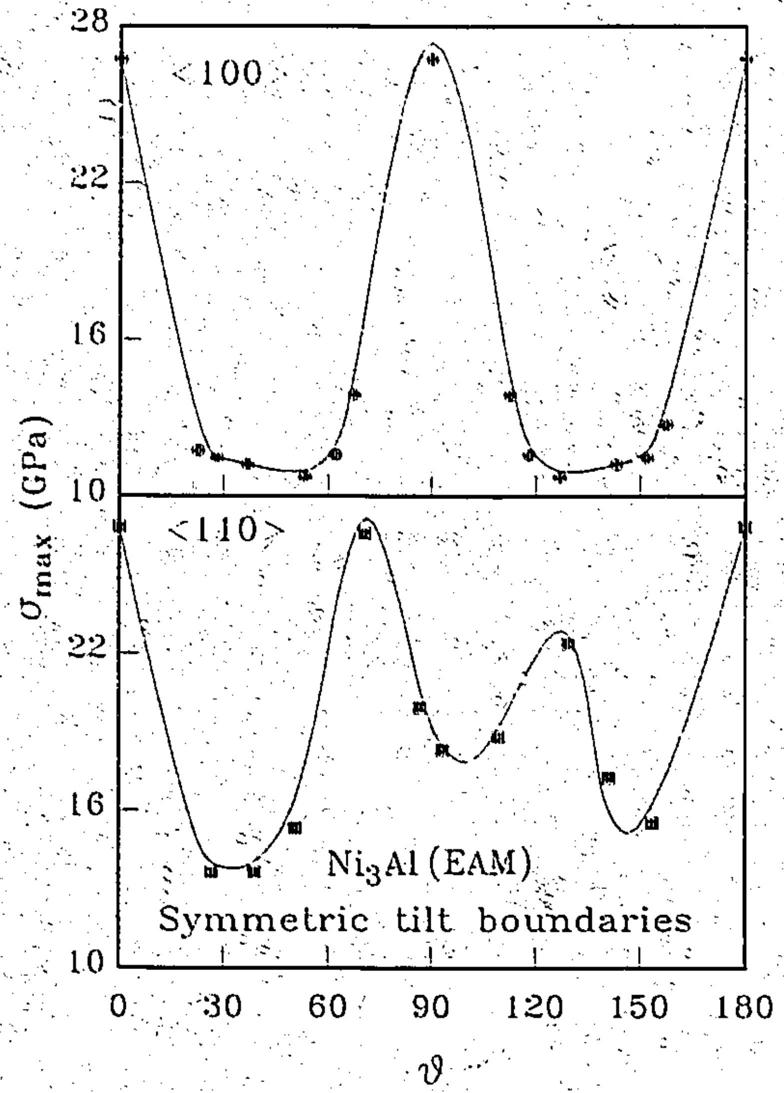

Figure 5.14(b) Fracture stress as a function of misorientation for symmetric tilt <100> and <110> boundaries in Ni_3Al.

polycrystalline materials is observed at very low strains. These results suggest that the tendency to intergranular fracture is not due merely to the poor fracture resistance of the grain boundaries. One must consider the overall grain boundary character distribution in polycrystals, because different grain boundaries may promote different transmissions of slip across grain boundaries by inducing the formation of a local region with different compositional disorder.

Using polycrystalline specimens with characterized grain boundaries, the effects of boundary Σ on intergranular fracture in metallic or ceramic materials and in Ni_3Al intermetallic compounds have been investigated by several researchers [Watanabe 1983, Hanada et al. 1986, Lin and Pope 1993]. It has been shown that low-angle boundaries and low-Σ coincidence boundaries are resistant to intergranular fracture while high-angle random boundaries easily fail, irrespective of materials, test conditions and environment. Further works [Lim and Raj 1984, Don and Majumdar 1986] have shown that the propensity of fracture decreases with decreasing Σ value for coincidence boundaries.

Summary

The above results confirm that similar structure effects on intergranular fracture as observed on bicrystals are also found in polycrystals, which strongly indicates that the structural effect on intergranular fracture is great enough not to be masked by the different stress conditions experienced by the various grain boundaries in the polycrystals. Even though there has been no theoretical prediction for the upper limit of Σ below which a coincidence boundary may not exhibit special mechanical behavior, judging from the experimental work reported in the literature, it is likely that the upper limit of Σ may take a value of approximately 29, although the actual value may depend on the material composition, microstructure, test conditions and environment.

As regards microstructural processes of fracture in polycrystalline materials, it has been shown that the occurrence of a fracture in a typically intergranular manner or a combined intergranular and transgranular manner depends, to a large degree, on the type of grain boundary in front of the propagating crack. When the main crack continues to propagate on weak random boundaries, a typical intergranular fracture occurs resulting in the loss of ductility and brittleness of the polycrystal. The effect of grain boundary character distribution on intergranular fracture of brittle polycrystalline materials will be discussed next in the microscopic model, using the information of fracture stress and grain boundary energy for various low Σ coincidence boundaries which have been shown in Tables 5.1 and 5.2.

5.4. Intergranular Fracture at the Microscopic Level

Intergranular fracture control in polycrystalline metals has involved the control of grain size in the μm range, grain shape and the formation of low-energy boundaries, for example, by obtaining a strong preferred grain orientation. In this section, crack path, crack arrest distance and fracture toughness in polycrystalline materials will be investigated for different fractions of low-energy grain boundaries, grain boundary fracture resistance, orientation of grain boundary plane and grain shape. As a result of studies of structure on intergranular fracture correlation, it has become possible to toughen brittle materials by grain boundary design and control.

5.4.1. Effect of Percentage of Low-energy Grain Boundaries on Intergranular Fracture

Examples of the propagation of a crack through a polycrystalline microstructure with different fractions of low-energy grain boundaries in a random orientation distribution of grain boundary planes are shown in Figure 5.15. In this case a small pre-crack was nucleated at the triple point in the bottom of the sample microstructure prior to straining the sample. This was necessary since prior to the development of the crack, the sample was elastically homogeneous. The crack begins by propagating along the low cohesion grain boundary network until it reaches a point where the grain boundary becomes too strong to be broken by the applied stress. At this point, the driving force for crack propagation along the grain boundary network is greatly

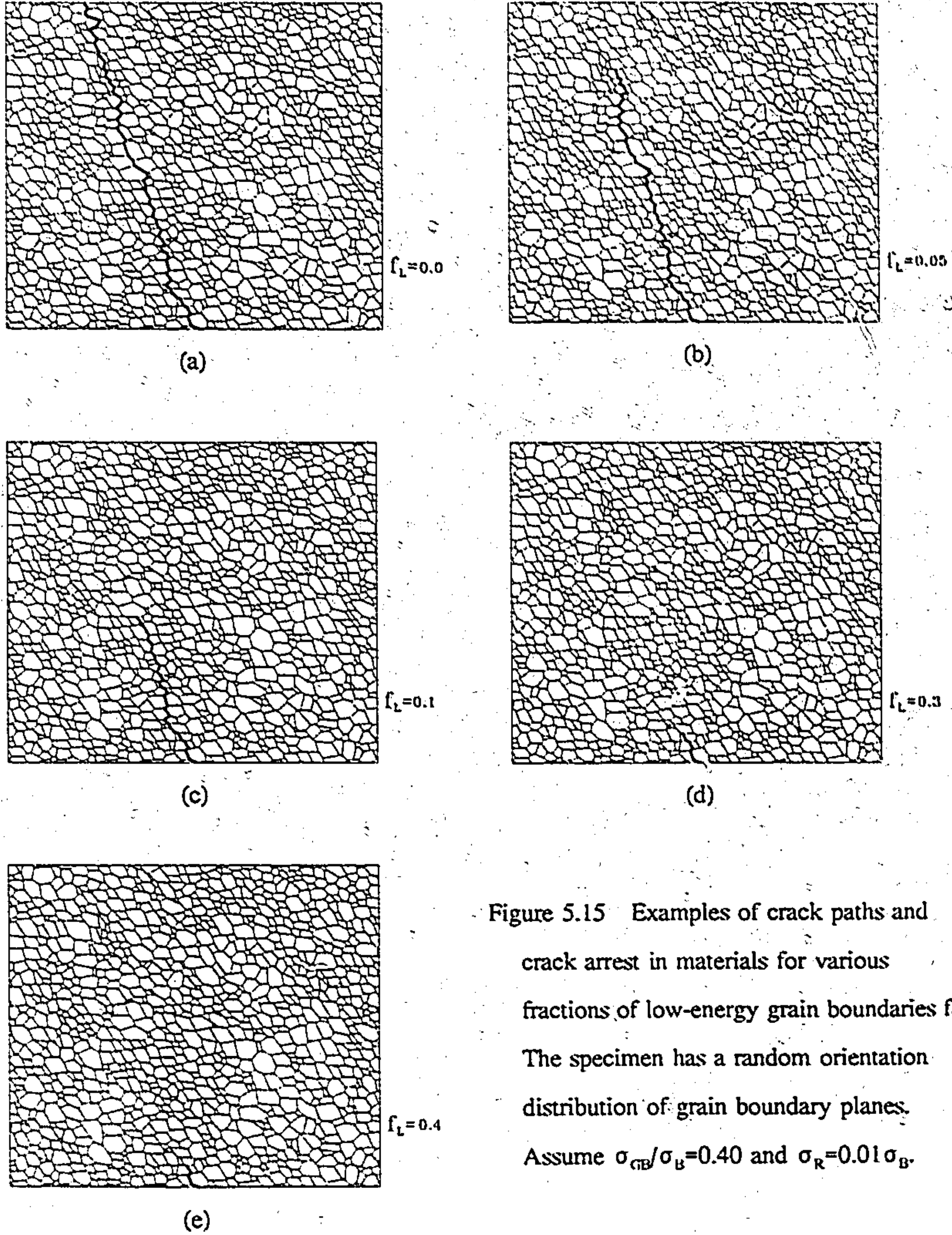

Figure 5.15 Examples of crack paths and crack arrest in materials for various fractions of low-energy grain boundaries f_L. The specimen has a random orientation distribution of grain boundary planes. Assume σ_{GB}/σ_B=0.40 and σ_R=0.01σ_B.

reduced, and the crack is arrested. Since grain boundaries are weak compared with the interior of the grain, the stress field of the crack nucleates a new crack at the site along the grain boundary. This figure demonstrates only one crack propagation until it is arrested.

The result also shows that the crack arrest distance decreases dramatically with an increase in the low-energy grain boundaries. Since the values of the crack arrest distance and other fracture parameters are highly dependent on the details of the microstructure in the vicinity of the pre-crack, they are calculated by using 80 different initial random seeds for the random orientation distribution of grain boundary planes. Figure 5.16 shows the normalized crack arrest distance required to blunt 99% of all propagating crack, as a function of the low-energy grain boundary fraction. As shown in this figure, by increasing the fraction of low-energy grain boundaries by only 10%, the crack length can be reduced considerably. The specimen has a random orientation distribution of grain boundary planes. The effect of the fracture resistance of a low-energy grain boundary can also be seen in Figure 5.16. Increasing the fracture resistance of this type of grain boundary can also reduce the crack arrest distance. The higher the fracture resistance of low-energy grain boundary, the less low-energy grain boundaries are required to arrest the crack propagating within a certain distance. For a low fracture resistance boundary, the crack propagation cannot be arrested within the critical distance even if there is a high percentage of these grain boundaries. This critical length defines a limit beyond which crack would continue to propagate to the point of component failure, even in the absence of either active grain boundary paths or a corrosive environment [Aust 1993, Palumbo et al. 1991]. In our case, if we define a distance of five grain diameters as the critical length and assume that more than 25% of grain boundaries are of low-energy with the highest fracture resistance, the cracks formed initially cannot propagate further that two grain diameters because of too few random boundaries and a high ductility of polycrystalline material. This result is in agreement with experimental and theoretical data presented by Watanabe [1993].

The influence of the low-energy grain boundary fraction, and the fracture resistance of a

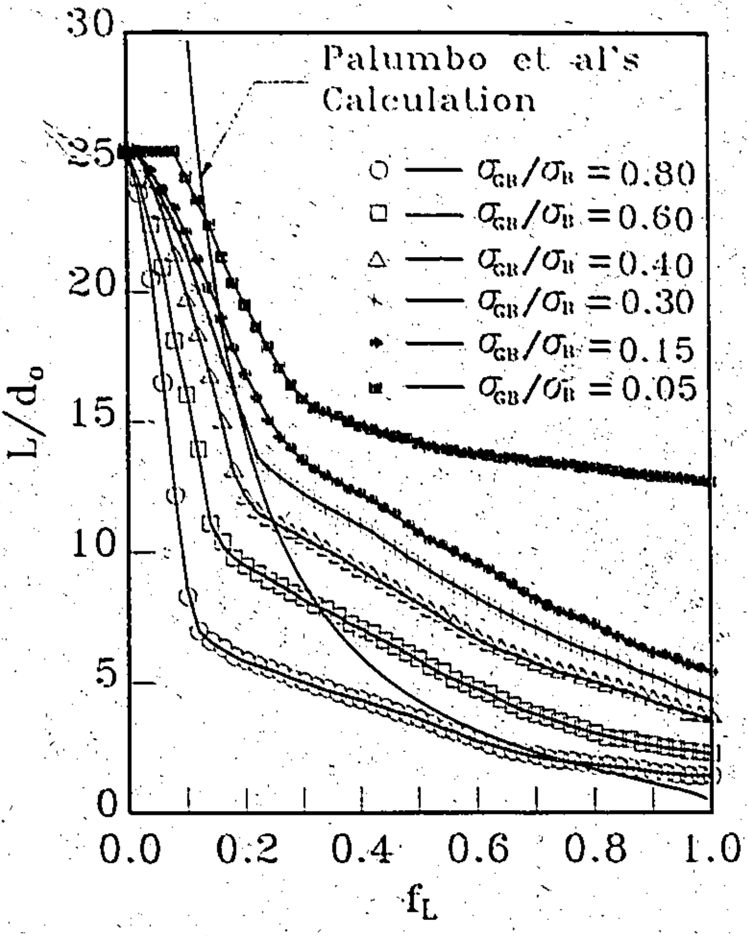

Figure 5.16 Normalized crack arrest distance (L/d_0) as a function of the fraction of low-energy grain boundaries f_L for different grain boundary fracture resistances σ_{GB}/σ_B. The specimen has a random orientation distribution of grain boundary planes. The random grain boundary fracture resistance is $\sigma_R=0.01\,\sigma_B$. Here σ_B is the fracture resistance of a perfect bulk crystal.

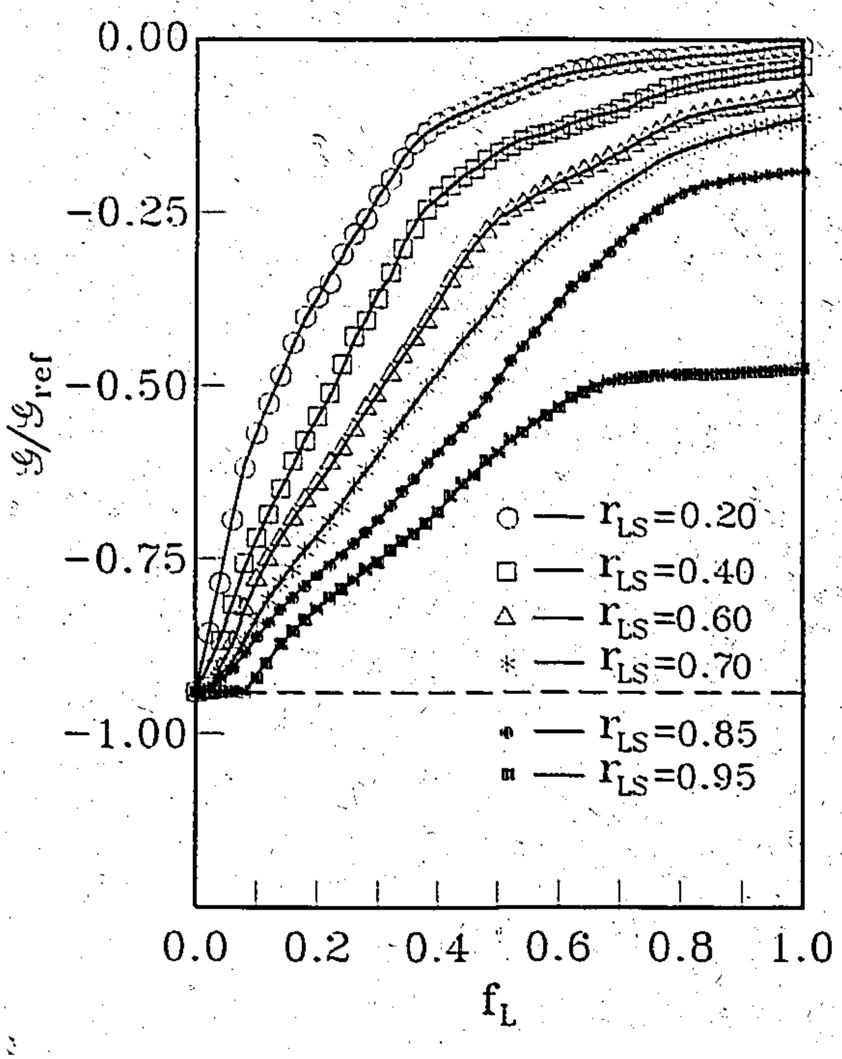

Figure 5.17 Fracture toughness $\mathcal{G}/\mathcal{G}_{ref}$ of the specimen as a function of the fraction of low-energy grain boundaries f_L for different grain boundary energies r_{LS} (=$0.5\gamma_{gb}/\gamma_s$). The specimen has a random orientation distribution of grain boundary planes. The random grain boundary energy is γ_R=0.99*2γ_s. Here γ_s is the average surface energy of an exposed grain boundary plane.

low-energy grain boundary on the fracture toughness of the specimen which has a random orientation distribution of grain boundary planes, is shown in Figure 5.17. Increasing the low-energy grain boundaries can increase the fracture toughness of brittle materials. The brittle materials can also be toughened by enhancing the fracture resistance of low-energy grain boundaries.

These results suggest the importance of grain boundary design and control through material processing, whereby a considerable decrease in intergranular crack propagation distance may be achieved through moderate increases of the fraction of low-energy grain boundaries with high fracture resistance in the grain boundary character distribution of brittle polycrystalline materials.

5.4.2. Effect of Orientation Distribution of Grain Boundary Planes on Intergranular Fracture

The orientation distribution of grain boundary planes also has an important role in controlling intergranular fracture of polycrystalline materials. Suppose there are 70% of low-energy grain boundaries and the grain boundary fracture resistance of the sample is $\sigma_{GB}/\sigma_{B}=0.40$. If these low-energy grain boundaries well aligned along the external stress direction, the crack path can easily propagate through the sample without being arrested, as shown in Figure 5.18(a). If they align perpendicularly to the external stress direction, however, the crack propagation will be arrested at a very early stage, as shown in Figure 5.18(d).

Figures 5.19 and 5.20 show the influence of the orientation distribution of grain boundary planes on crack arrest distance and fracture toughness. The results indicate that better design and control in the orientation distribution of grain boundary planes can reduce crack propagation distance and enhance the toughness of brittle polycrystalline materials according to the stress field in work environment.

However, the orientation distribution of grain boundary planes is very difficult to design and control during processing. There are no effective techniques, and therefore people usually try to increase the fraction of the low-energy grain boundary with high fracture resistance in order to

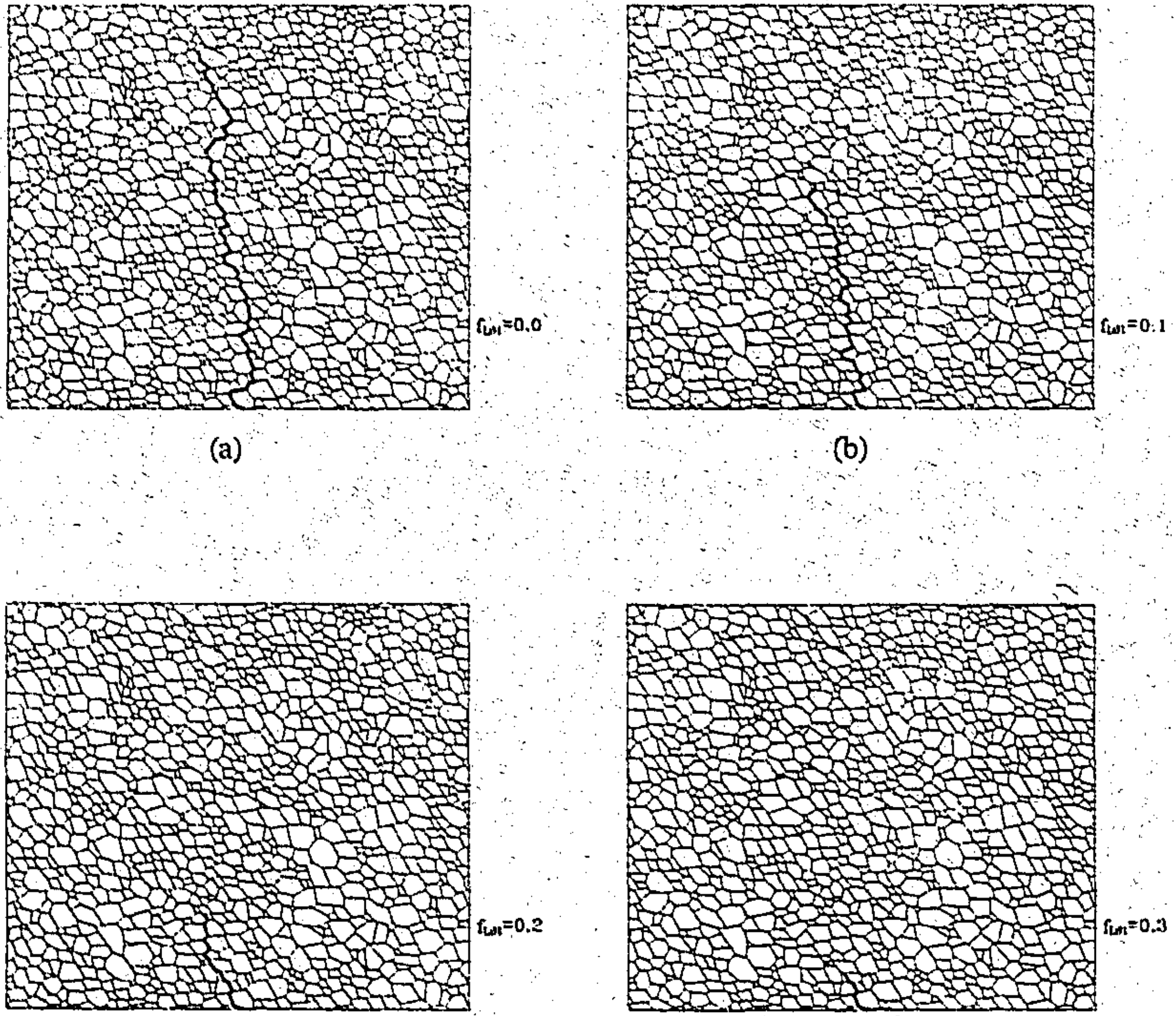

(a) (b)

(c) (d)

Figure 5.18 Examples of crack paths and crack arrest in materials for various fractions of low-energy grain boundaries $f_{L\theta I}$. The specimen has an orientation distribution of grain boundary planes. Assume f_L=0.7, σ_{GB}/σ_B=0.4, and σ_R=0.01σ_B.

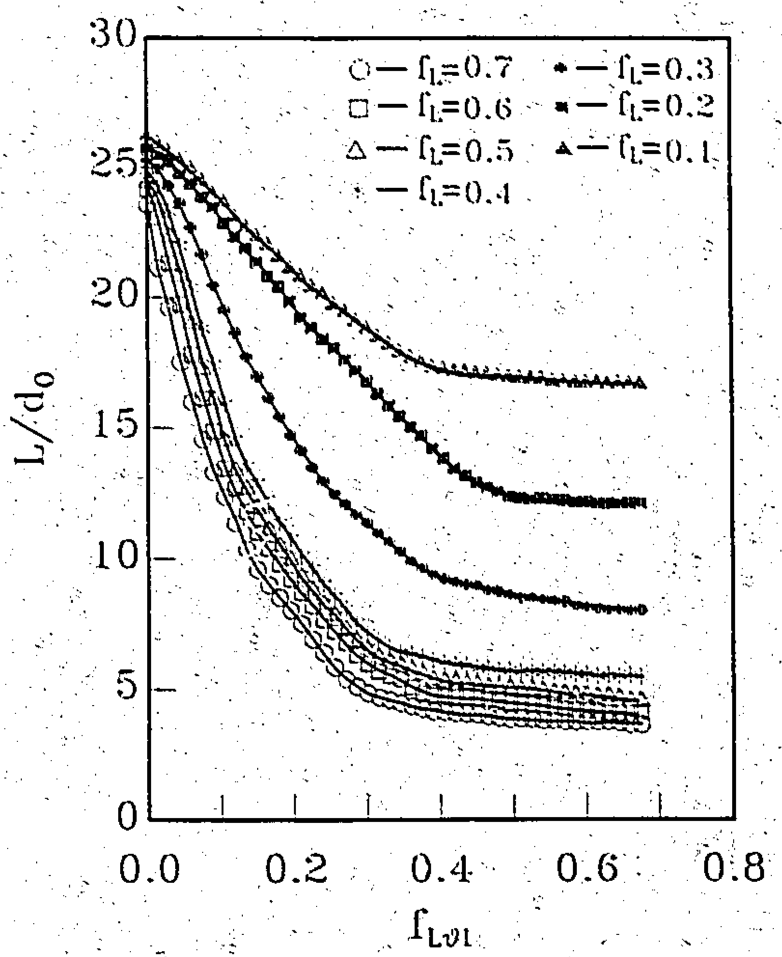

Figure 5.19 Normalized crack arrest distance (L/d_0) as a function of the fraction of low-energy grain boundaries $f_{L\theta 1}$ for various fractions of low-energy grain boundaries f_L. The specimen has an orientation distribution of grain boundary planes. The grain boundary fracture resistance is σ_{GB}/σ_B=0.40 and the random grain boundary fracture resistance is σ_R=0.01 σ_B. Here σ_B is the fracture resistance of a perfect bulk crystal.

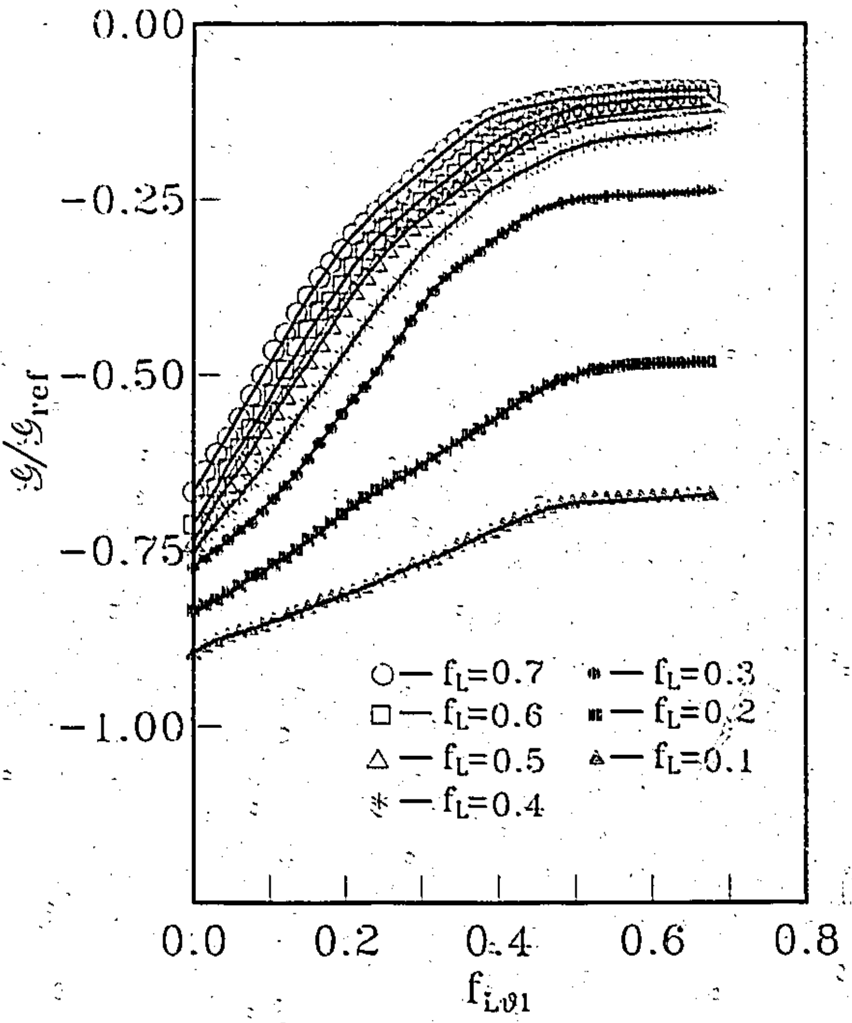

Figure 5.20 Fracture toughness $\mathscr{G}/\mathscr{G}_{ref}$ of the specimen as a function of the fraction of low-energy grain boundaries f_{L01} for various fractions of low-energy grain boundaries f_L. The specimen has an orientation distribution of grain boundary planes. The grain boundary energy is r_{LS} ($=0.5\gamma_{gb}/\gamma_s$)=0.40 and the random grain boundary energy is $\gamma_R=0.99*2\gamma_s$. Here γ_s is the average surface energy of an exposed grain boundary plane.

improve fracture toughness of brittle materials. The above results also show that there is no great difference between reducing the crack propagation distance and improving the toughness of brittle materials if the low-energy grain boundary fraction is more than 40%. This means that 40% of the average low-energy grain boundaries would be enough to obtain maximum improvement of intergranular fracture performance.

A discussion of the design and control of the orientation distribution of grain boundary planes may give us indications of how to use various new techniques of material processing to enhance the intergranular fracture performance of brittle polycrystalline materials.

5.4.3. Effect of Grain Shape on Intergranular Fracture

Grain shape is an important factor affecting the intergranular fracture behavior of brittle materials. Unidirectional solidification by zone-melting can be used to modify the grain shape and drastically improve the ductility of polycrystalline Ni_3Al without addition of boron or any other third element [Hirano 1990]. The observed improvement in ductility of Ni_3Al polycrystal is due to an increase of fraction of low-energy grain boundaries and the grain shape changes.

Figure 5.21 shows examples of crack paths and crack arrest in materials with various grain shape. The more grain boundaries are aligned along the external stress direction, the longer the crack propagation distance and tougher the sample. If more grain boundaries are aligned perpendicularly to the external stress, the sample becomes brittle and the crack path can easily propagate through the sample.

Figures 5.22 and 5.23 show the normalized crack arrest distance and fracture toughness of the specimen as a function of the grain shape factor. The results indicate that an increase of the grain shape factor increases the crack arrest distance and decreases the fracture toughness. For grain boundaries with low fracture resistance, the design and control of grain shape seems to be an effective way to decrease the crack propagation distance and to enhance the fracture toughness (as shown in Figure 5.23).

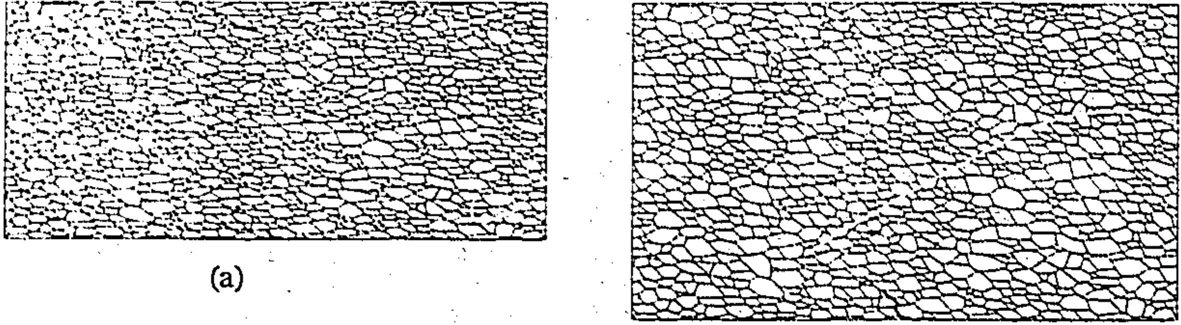

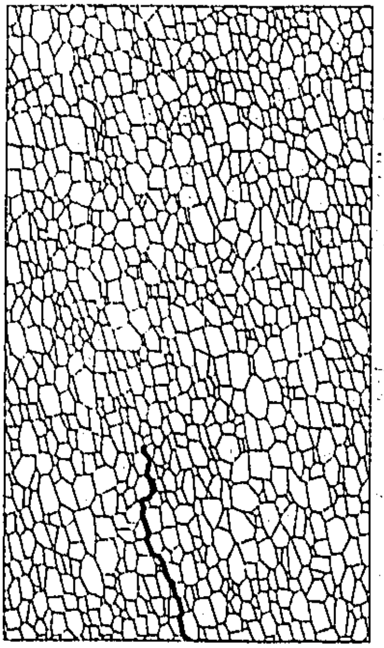

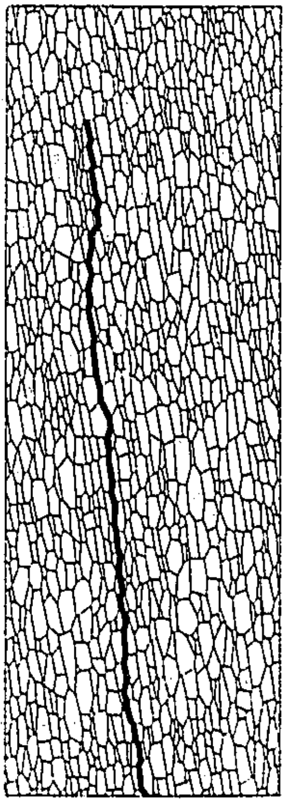

Figure 5.21 Examples of crack paths and crack arrest in materials for various grain shape factors f_{sp} (a-0.252, b-0.312, c-0.546, and d-0.635). The specimen has a random orientation distribution of grain boundary planes.

Assume f_L=0.4, σ_{GB}/σ_B=0.4, and σ_R=0.01σ_B.

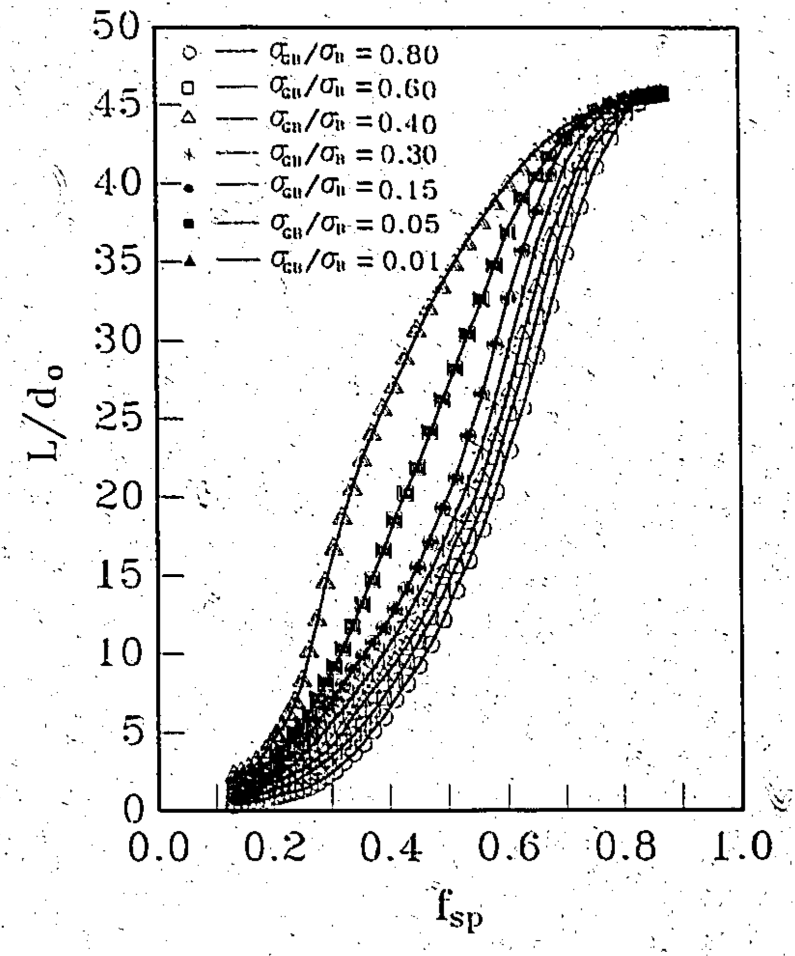

Figure 5.22 Normalized crack arrest distance (L/d_0) as a function of the grain shape factor f_{sp} for different grain boundary fracture resistances σ_{GB}/σ_B. The specimen has a random orientation distribution of grain boundary planes. The fraction of low-energy grain boundaries is f_L=0.40 and the random grain boundary fracture resistance is σ_R=0.01 σ_B. Here σ_B is the fracture resistance of a perfect bulk crystal.

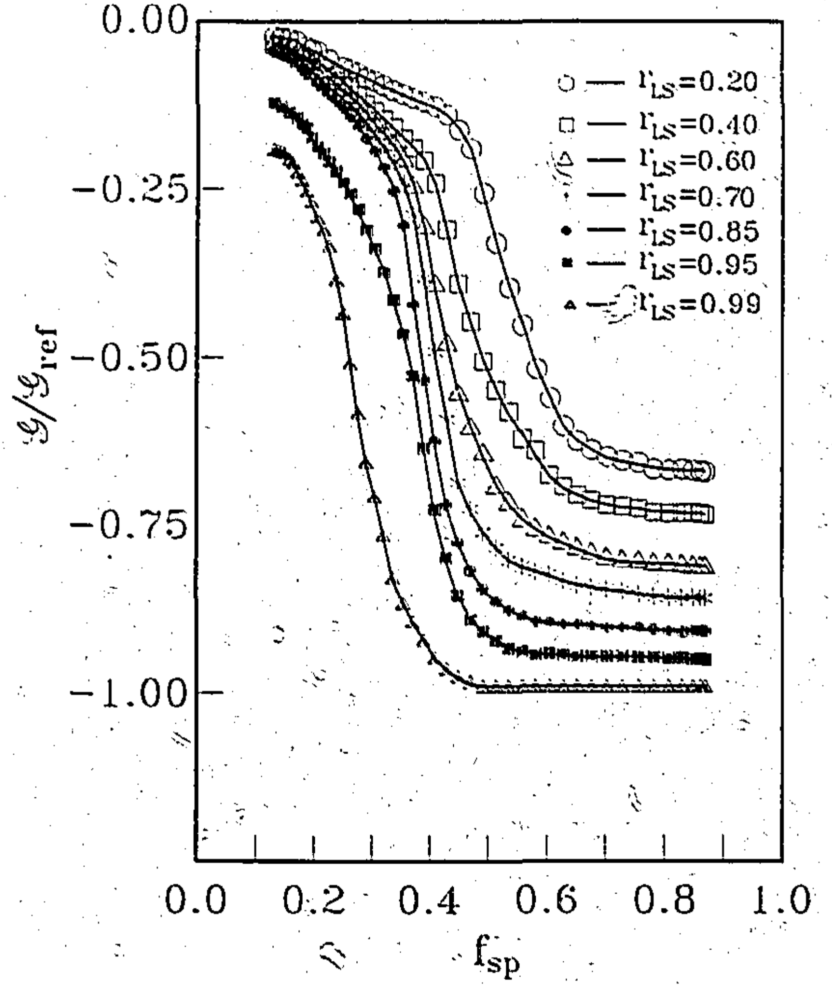

Figure 5.23 Fracture toughness $\mathcal{G}/\mathcal{G}_{ref}$ of the specimen as a function of the grain shape factor f_{sp}, for different grain boundary energies r_{LS} (=$0.5\gamma_{gb}/\gamma_s$). The specimen has a random orientation distribution of grain boundary planes. The fraction of low-energy grain boundaries is f_L=0.40 and the random grain boundary energy is γ_{gb}=0.99*2γ_s. Here γ_s is the average surface energy of an exposed grain boundary plane.

5.5. Integrated Approach to Intergranular Fracture

As we have already seen, all simulated intergranular fractures are, in general, controlled by the grain boundary character distribution which includes grain boundary structure and energy, orientation distribution of grain boundaries, microstructure of polycrystalline materials, and grain shape and size. This project concentrates on one simple case: intergranular fracture at low temperatures caused by the intrinsic weakness of grain boundaries. We thereby avoid complexities of segregation of forcing atoms at the grain boundaries and make it possible to reveal the purely structural relations. Since we have already simulated the intergranular fracture behavior at both the atomistic and microscopic levels in this section, we are now integrating the information at both levels to study the intergranular crack propagation in brittle Ni_3Al materials. For comparison with the experimental results, three material processes: annealing, strain annealing, and unidirectional solidification, are investigated so that the intergranular fracture in the brittle polycrystalline materials may be controlled by design the grain boundary character distribution.

5.5.1. Intergranular fracture in annealed Ni_3Al

The distribution of grain boundary types along intergranular cracks in annealed Ni_3Al was analyzed using Σ value and general grain boundary concepts, and compared to the grain boundary character distribution in the bulk, using statistically significant sample sizes [Lin and Pope 1993]. Melt-spun Ni_3Al ribbons (75.0 at.% Ni, 24.8 at.% al and 0.2 at.% Ta, about 15mm x 3mm x 20μm) were used as specimens. These ribbons were first annealed at 1200°C for 1h in a 10^{-6} torr vacuum to allow individual grains to grow through the thickness of the ribbons, thereby making the surface structure characteristic of that of the bulk. Both surfaces of the annealed ribbons were then mechanically polished to remove the alumina/spinel scale using standard metallographic polishing procedures. A second anneal was taken at the same conditions with a graphite oxygen-getter, which reveals grain boundaries through thermal etching. Bending tests were performed to examine the types of cracks boundaries. Calculations were made by our microstructural model using the grain boundary fracture resistance from the atomic-model, microstructure from the Monte Carlo simulation, grain boundary distribution from experimental data, with random orientation distribution of grain boundary planes and assuming equiaxial grain.

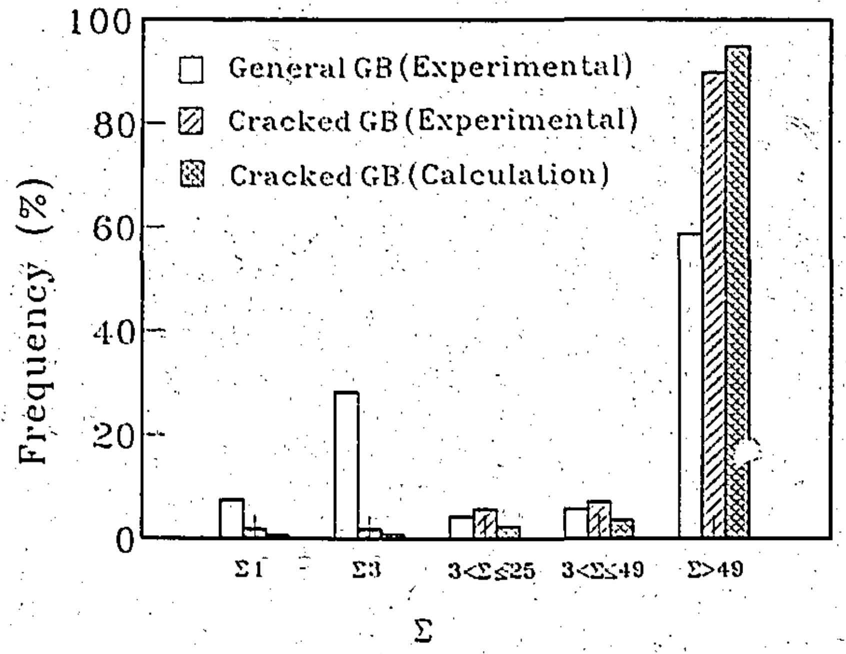

Figure 5.24 The distribution of grain boundary types by Σ values for cracked grain boundaries observed by experiment and calculated using our models compared with the general population of grain boundaries in Ni_3Al.

Figure 5.24 shows the distribution of grain boundary types by Σ values for cracked grain boundaries observed by experiment and calculated using our models compared with the general population of grain boundaries in Ni_3Al. This graph indicates that our calculation of intergranular crack propagation agrees very well with experimental results.

Both calculation and experimental results found that low angle $\Sigma 1$ boundaries and symmetrical $\Sigma 3$ twin boundaries are particularly strong; low Σ, high angle boundaries, are not so strong; high Σ, high angle boundaries (random boundaries) are weak. This means that the strength of a polycrystalline aggregate with weak grain boundaries can be increased by increasing the fraction of $\Sigma 1$ and symmetrical $\Sigma 3$ twin boundaries, and possibly other special boundaries such as symmetrical $\Sigma 11$ twin boundaries, which are not sufficiently numerous to be identified in the experimental study.

5.5.2. Intergranular fracture in strain annealed Ni_3Al

The grain boundary character distributions in cast, recrystallized and strain annealed Ni_3Al alloys with a composition of Ni-23Al were examined to clarify the relation between ductility and the grain boundary character distributions in Ni_3Al [Chiba et al. 1994]. A button ingot of Ni-23Al alloy was prepared by arc melting to attain chemical homogeneity on a water-cooled copper hearth in an argon gas atmosphere at a pressure of approximately 93kPa. The specimens were then cold-forged, encapsulated in a vacuum of 10^{-3}Pa with a sponge Zr getter, and annealed at 1323 K for 1728ks for homogenization and recrystallization. Strain annealing was repeatedly conducted three times in a vacuum of 10^{-3}Pa at 1323K for 864ks to change the occurrence of CSL boundaries in Ni_3Al specimens. Tensile tests were performed using an Instron-type machine at an initial strain rate of $5.2 \times 10^{-4} s^{-1}$. Calculations were conducted by our microstructural model using the grain boundary fracture resistance from atomic-model, microstructure from the Monte Carlo simulation, grain boundary distribution from experimental data, with random orientation distribution of grain boundary planes and equiaxial grain shape.

Table 5.6 shows the distribution of occurrence of CSL boundaries, and both experimental and calculated fracture parameters. Three types of specimen are examined; cast, recrystallized and strain annealed. The results also indicate that our calculation of fracture behavior agree with the experimental data for cast, recrystallized and strain annealed Ni_3Al alloy.

Table 5.6 Occurrence of CSL boundaries and fracture behavior in cast, recrystallized and strain annealed Ni_3Al alloys.

System investigated	Cast	Recrystallized	Strain annealed
Percentage of frequency of occurrence for			
$\Sigma 1$	0	2.21	7.69
$\Sigma 3$	4.46	8.63	21.5
$\Sigma 5$	4.46	4.2	2.56
$\Sigma 7$	0.89	3.54	3.21
$\Sigma 9$	0.89	2.88	3.85
$\Sigma 11$	0.89	2.65	1.28
$\Sigma 13$	4.46	3.32	0.64
$\Sigma 15$	1.79	3.76	2.56
$\Sigma 17$	1.79	0.44	3.85
$\Sigma 19$	0.89	1.77	2.56
$\Sigma 21$	1.79	3.54	1.92
$\Sigma 23$	2.68	2.65	2.56
$\Sigma 25$	1.79	1.33	1.92
$\Sigma 27$	0	1.33	0.64
$\Sigma 29$	0	0.88	2.56
$\Sigma 1+\Sigma 3$	4.46	10.8	29.2
Random	73.2	56.9	41.7
Fracture behavior (tensile tests) -- experimental			
Maximum tensile stress σ_{max} (MPa)	168.65	424.87	515.68
Maximum tensile strain ε_{max} (%)	8.89	13.03	47.87
Fracture behavior (tensile tests) -- calculation			
Crack arrest distance L/d_0	12.37	4.86	2.54
Fracture toughness $\mathcal{G}/\mathcal{G}_{ref}$	-0.58	-0.22	-0.06

The experimental results show that the sum of the percentage of $\Sigma 1$ and $\Sigma 3$ boundaries in strain annealed Ni_3Al alloys is significantly higher than that in cast and recrystallized Ni_3Al

alloys. The frequency of the occurrence of CSL boundaries can be enhanced by changing the microstructure formed during solidification. Strain annealing is very effective in enhancing the frequency of the occurrence of CSL boundary, especially for Σ1 and Σ3 boundaries. The experimental results also show that the maximum tensile stress of the strain annealed Ni_3Al alloy is three times greater than that of the cast alloy, the strain annealed alloy exhibits elongation of approximately 50% and the cast alloy exhibits less than 9%. The calculation results show that the crack arrest distance of the strain annealed alloy is almost five times less than that of the cast alloy, and the fracture toughness of the strain annealed alloy is almost 10 times higher than that of the cast alloy. Therefore, both calculation and experimental results indicate that the fracture toughness of Ni_3Al can be improved by increasing occurrence of the CSL boundaries, especially for Σ1 and/or Σ3 boundaries through strain annealing.

5.5.3. Intergranular fracture in Ni_3Al obtained by unidirectional solidification

Quite recently Hirano [Hirano et al, 1990, 1991, 1992, 1993] found that unidirectional solidification by zone-melting can drastically improve the ductility of polycrystalline Ni_3Al without boron. It is surprising that so-called inherently brittle Ni_3Al could be made ductile without the addition of boron or other third element. The alloy grown by unidirectional solidification has the columnar-grained structure of Ni_3Al and shows about 60% large tensile elongation at room temperature along the columnar structure. Of particular interest is that it also shows tensile elongation (about 15%) in the transverse direction. Cold rolling at room temperature was additionally found to be possible without the addition of ductility-enhancing elements.

The polycrystalline Ni_3Al was grown unidirectionally from stoichiometric Ni_3Al rod in a flowing argon atmosphere using a floating zone method [Hirano 1990]. The optimum growth rate was examined in the range of 2-24 mm/h. Tensile tests were carried out at room temperature parallel and perpendicular to the growth direction with an initial strain rate of $4.2 \times 10^{-3} s^{-1}$. The alloys show a columnar grain structure with weak <100>+<111> or <110>+<111> texture. More recently, Watanabe et al [Watanabe 1993] measured the frequency of coincidence boundaries (Figure 5.25). It has been found that the observed improvement in ductility of undoped Ni_3Al polycrystal is due to the introduction of a high frequency of low angle boundaries and low Σ (3, 9) coincidence boundaries. Calculations were conducted by our microstructural model using the grain boundary fracture resistance from the atomic-model, microstructure from the Monte Carlo simulation, grain boundary distribution from experimental data, with random orientation distribution of grain boundary planes and columnar structure of grains.

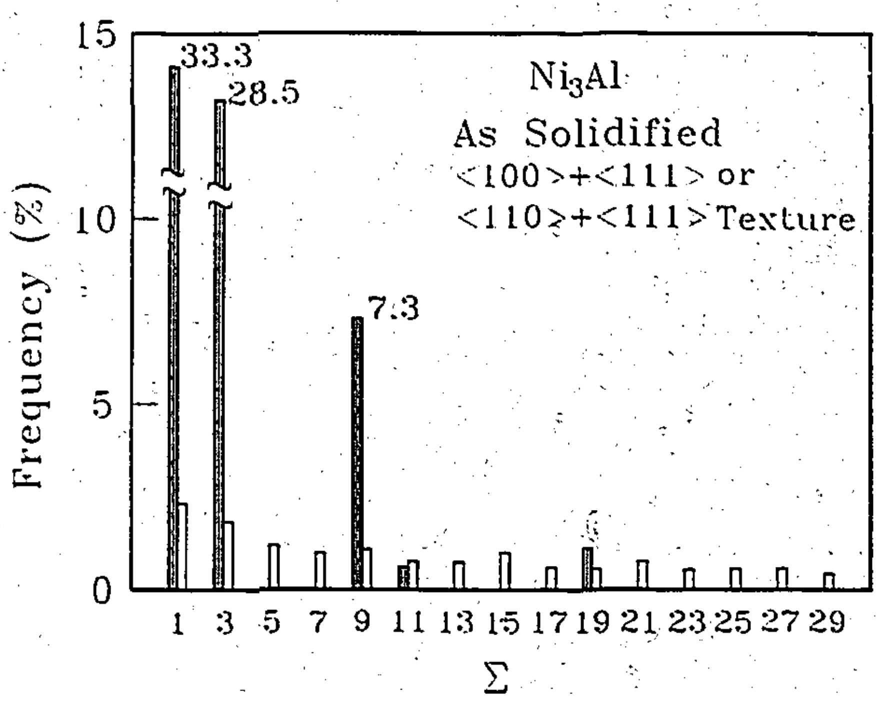

Figure 5.25 The frequency of coincidence grain boundaries as a function of Σ for as-solidified Ni_3Al polycrystal. The right column is for random specimen.

Figure 5.25 shows the frequency of coincidence boundaries as a function of Σ of an unidirectionaly solidified Ni_3Al alloy. Table 5.7 shows the experimental and calculated results of fracture behavior for this alloy. It can be easily seen that the calculated results of fracture behavior accord well with experimental data.

Table 5.7 Fracture behavior (both experimental and calculation) in Ni_3Al alloy obtained by unidirectional solidification.

	∥ GD	⊥ GD
Fracture behavior (tensile tests) -- experimental		
Maximum tensile stress σ_{max} (MPa)	440	446
Maximum tensile strain ε_{max} (%)	102	25
Fracture behavior (tensile tests) -- calculation		
Crack arrest distance L/d_0	0.31	2.87
Fracture toughness $\mathcal{G}/\mathcal{G}_{ref}$	-0.03	-0.08
Fracture behavior (tensile tests) -- calculation (random distribution)		
Crack arrest distance L/d_0	18.12	25.12
Fracture toughness $\mathcal{G}/\mathcal{G}_{ref}$	-0.53	-0.67

GD: Growth direction.

The frequency of low energy boundaries of an as-solidified sample is more than 70% with a high frequency of $\Sigma 1$, 3, 9 and 19. From our calculations and experimental data there is no doubt that the grain boundary character distribution is the key factor controlling the ductility and is very powerful in improving the fracture toughness of Ni_3Al. The result also suggests that conventional thermo-mechanical treatment of Ni_3Al will not necessarily bring about any toughness improvement of an Ni_3Al alloy produced by unidirectional solidification.

CHAPTER 6:
CONCLUSIONS

- An integrated computer simulation employing the Embedded-atom method (EAM), Molecular dynamics (MD), and Markov Chain Fracture models has been constructed and applied to study the intergranular fracture of brittle polycrystalline materials at both the atomistic and microscopic levels.

- At the atomistic level, the computer model is capable of treating bicrystals under the influence of external load and temperature with dynamic periodic boundary conditions along the grain boundary plane and dynamic boundary conditions perpendicular to the grain boundary plane.

- The verification of computer simulation models indicates that the agreement between the model's predictions and experimental results is quite good for both the ordered and disordered systems at both the low and high temperatures.

- The EAM functions have been calculated for Cu, Ni, Al and Ni_3Al and have been found to accurately reproduce several experimental results in Cu, Ni, Al and Ni_3Al systems.

- The EAM functions, where their calculations are based on the perfect fcc crystal with very simple defects at low temperature, can predict the properties of a very complex system, such as liquid and metallic glass, and their transformation, which are also found to agree with experimental quantities in Ni.

- The structure and energy of various Σ grain boundaries have been studied at the atomistic level for Cu, Ni, and Ni_3Al. A linear relationship between the grain boundary energy and volume expansion was observed, which is in agreement with other researchers' predictions. This linear relationship suggests that many grain boundary related properties can easily be correlated with the average volume expansions of grain boundaries constituting a polycrystal.

- The simulation has shown that both grain boundary energy and free volume depend strongly on the grain boundary structure. The energy of <001> boundaries is more than twice as great as that of <111> boundaries. Σ3 <111> twist and <110> 70.53° tilt coherent twin boundaries have the lowest grain boundary energy and free volume, which is also in agreement with the experimental results.

- The fracture behavior of many Σ grain boundaries has been investigated at the atomistic level for Cu, Ni, and Ni_3Al, and the fracture resistance of grain boundary was predicated. It has been found that symmetrical Σ3 twin boundaries and low angle Σ1 boundaries are particularly resistant to intergranular fracture, that some other low Σ boundaries are also strong, but that grain boundaries with high energies are not fracture resistant. Calculated correlation between fracture resistance and misorientation of grain boundaries agrees with the experimental data.

- Calculated fracture resistances of the grain boundaries for Ni_3Al alloy are not significantly different from for pure Ni. This suggests that the tendency to intergranular fracture is not due merely to the poor fracture resistance of the grain boundaries. One must consider the overall grain boundary character distribution.

- At the microscopic level, the computer model is capable of analyzing the samples under the influence of an external load for any microstructure described by the grain occurrence distribution and by the grain boundary character distribution.

- The crack path, crack arrest distance, and fracture toughness of intergranular fracture have been investigated at the microscopic level with varying fraction of the low-energy grain boundaries, grain boundary fracture resistance, orientation distribution of grain boundary planes, and grain shape factor to discover and analyze the role of grain boundary character distribution on the intergranular fracture in polycrystalline materials.

- The simulations have predicted that with an increase in the fraction of low energy grain boundaries, the fracture toughness increases while the crack arrest distance decreases. By increasing the number of low energy grain boundaries aligned parallel to the stress axis, one observes an increase of the fracture toughness and a decrease of the crack arrest distance. By increasing the grain shape factor, the fracture toughness decreases while the crack arrest distance increases.

- The intergranular crack formed initially cannot propagate further because of the presence of fewer random boundaries and because the polycrystalline materials will show high ductility if we define five grain diameters as the critical length and if more than 25% of grain boundaries are of low-energy with the highest fracture resistance, such as $\Sigma 3$ twin grain boundaries, etc.

- The improvement in fracture toughness of Ni_3Al brittle polycrystal is due to the introduction of a high frequency of low energy grain boundaries (up to 70% by experiment). Grain boundary design and control by manipulating the grain boundary character distribution (GBCD) are important to fracture toughness improvement of brittle polycrystalline materials.

The Original Contributions to New Knowledge

- A new, integrated atomistic and microscopic level model of the intergranular fracture process in brittle polycrystalline materials has been proposed, constructed and tested.

- At the atomistic level, the computer model is capable to analyze bicrystals under external load and different temperatures using EAM, dynamic periodic boundary conditions along the grain boundary plane and dynamic boundary conditions in the direction perpendicular to the grain boundary plane.

- At the microscopic level, the new computer model is capable to analyze the sample with microstructure defined by the grain boundary character distribution, having various grain shapes. For such sample which is deformed by an external load, the model predicts the path of intergranular crack propagation and proposes methods to improve fracture resistance.

- The new integrated model demonstrates that the intergranular crack cannot propagate further when the polycrystalline materials have sufficient number of fracture resistant grain boundaries and/or the grain boundary planes are oriented favorable with respect to the existing stress.

- The computational predictions proposed using this method are compared to experimental results obtained from Ni_3Al brittle polycrystal. It was demonstrated that by design and control of the grain boundary character distributions the fracture properties of Ni_3Al materials can be predicted.

Recommendations for Future Work

- Investigation of the effect of impurities on the fracture behavior of low energy grain boundaries should be carried out to confirm experimental results indicating that low energy boundaries are not good sites for segregation, and, therefore, their fracture resistances are insensitive to material purity irrespective the types of grain boundaries. In order to do this one must have a very good atomic potential for the impurities and their interactions with metals.

- A 3-dimensional microscopic model is expected to understand the intergranular fracture in practical world with 3-dimensional features about the grain boundary character distributions.

- A 3-dimensional macroscopic model using finite element analysis combined with texture and plastic deformation of materials can be integrated into our model in engineering stages. Zhou et al. [1991, 1992, 1994] have done research discussing the macroscopic level of plastic deformation in textured materials. There is a possibility to add limited plastic deformation into our models. The possibility of fracture control by controlling texture is practically important but has not yet been seriously taken into account from the view point of grain boundaries. Designing and controlling texture appears to be very promising for the control of intergranular fracture and toughening of polycrystalline materials.

- Direct experimental measurements of the fracture resistance for low-energy grain boundaries in certain pure metals and alloys are strong recommended, although they are difficult in practice. In particular, the relationships between fracture resistance and misorientation of grain boundaries need to be better understood and studied so that the integrated computer modeling of intergranular fracture can be further improved.

APPENDIX:

CALCULATION OF EAM FUNCTIONS

As described in Chapter 3, the techniques employed in the atomistic study required interatomic potentials which are obtained using the embedded atom method (EAM) [Daw and Baskes 1984]. The purpose of this appendix is to present a description of the EAM functions obtained with the method.

The ground-state properties of the solid can be calculated in a straightforward manner from Eq. (2.4). Although it is possible to pursue the evaluation of these properties from a first principals approach, a tact more viable in the EAM is to express each term as a parametric function and to fit the parameters to experimental quantities. During the calculation of the EAM functions, both the atomic electron density, $\rho_j(r)$, and the effective charges, $Z(r)$, are cut off at a distance R_c so that the interactions are of finite range. In both cases, the functions are zero for $r>R_c$, and for $r<R_c$, a constant shift is added so that the functions go to zero at R_c, i.e., $Z(r)$ is replaced by $Z(r)-Z(R_c)$ and similarly for $\rho_j(r)$ [Foiles 1992].

Information about the embedded function $F(\rho)$ for densities well away from equilibrium ρ_{eq} is obtained through the equation of the state of the expanded or compressed metals for which the electron density at each lattice site is substantially different from ρ_{eq} [Foiles et al. 1986]. Rose et al. [1984] have shown that the sublimation energy of most metals as a function of lattice constant can be scaled to a simple universal function:

$$E(a) = -E_{sub}(\ 1 + a^*\ )\, e^{-a^*} \tag{A1}$$

In this expression, E_{sub} is the absolute value of the sublimation energy at zero temperature and pressure. The density a^* is a measure of the deviation from the equilibrium lattice constant:

$$a^{*} = \frac{\frac{a}{a_0} - 1}{\left(\frac{E_{sub}}{9B\Omega}\right)^{\frac{1}{2}}} \tag{A2}$$

where B is the bulk modulus of the material, a is a length scale of the system that we will take to be the fcc lattice constant, a_0 is the equilibrium lattice constant, and Ω is the volume per atom at equilibrium. The embedding function is determined by requiring that the zero-temperature equation of state, E(a), is satisfied for all lattice constant a. However, if this is taken literally, as the lattice is expanded to the point where the nearest neighbor distance, R_{nn}, is equal to cutoff, R_c, the density and pair interaction will be zero but the total energy will not [Foiles 1992]. This means that the embedding function at zero density is non-zero and the functions will not reasonably manage the case of an atom moving away from the solid. To manage/control this, the equation of state was modified so that $E(a_{cut})=0$ where a_{cut} is the lattice constant such that the nearest neighbor distance equals R_c, i.e., $a_{cut}= 2^{1/2} R_c$ for a fcc lattice [Foiles 1992]. The modified equation of state is defined by the following equations:

$$E(a) = E_{sub}\frac{f(a^{*}) - e}{1 - e} \tag{A3}$$

where

$$f(a^{*}) = (1 + a^{*})\, e^{-a^{*}}, \tag{A4}$$

$$a^{*} = \frac{a - a_0}{\lambda a_0}. \tag{A5}$$

The quantities e and λ are defined by:

$$e = f\left(\frac{R_c - R_{nn}}{\lambda_0 R_{nn}}\right) \tag{A6}$$

$$\lambda_0 = \left(\frac{E_{sub}}{9B\Omega}\right)^{\frac{1}{2}} \tag{A7}$$

and

$$\lambda = \frac{\lambda_0}{(1 - e)^{\frac{1}{2}}} \tag{A8}$$

The net result of all these manipulations is that E(a) is not changed near $a=a_0$ (through second order in $(a-a_0)$) but that E(a) goes to zero near $a=a_{cut}$. Note that for the cutoffs used here, e is rather small.

In the calculation, the only input data needed are the equilibrium lattice constant, elastic constants, vacancy-formation energy, bulk modulus, and sublimation energy of a perfect, homonuclear crystal [Daw and Baskes 1984], which are generally readily available. Because all atoms are equivalent, $F=F_i$, $\phi=\phi_{ij}$, and $\rho=\rho_j$. We can define ρ_{eq} to be the density at equilibrium, so that $\rho_{eq}=\rho_{h,i}$ for every i and $\rho_{eq}=\Sigma_m\ \rho(a^m)$, where the a^m are the distances between neighbors and the sum is over neighbors. Also, we defined $\phi_{eq}=\Sigma_m\ \phi(a^m)$.

The lattice constant is given by the equilibrium condition:

$$A_{ij} + F'(\rho_{eq})\, V_{ij} = 0, \tag{A9}$$

where

$$A_{ij} = \frac{1}{2}\sum_{m} \frac{\phi'_m a_i^m a_j^m}{a^m}, \tag{A10}$$

$$V_{ij} = \frac{1}{2}\sum_{m} \frac{\rho'_m a_i^m a_j^m}{a^m}, \tag{A11}$$

and where a_j^m is the ith component of the position vector to the m neighbor, $\phi'_m=[d\phi(r)/dr]_{r=a^m}$, and $\rho'_m=[d\rho(r)/dr]_{r=a^m}$.

The elastic constants at equilibrium are given by:

$$C_{ijkl} = \frac{1}{\Omega_0}\left[\, B_{ijkl} + F'(\rho_{eq})\, W_{jikl} + F''(\rho_{eq})\, V_{ij} V_{kl} \,\right] \tag{A12}$$

where Ω_0 is the undeformed atomic volume, and

$$B_{ijkl} = \frac{1}{2}\sum_{m} \frac{\left(\phi''_m - \dfrac{\phi'_m}{a^m}\right) a_i^m a_j^m a_k^m a_l^m}{(a^m)^2}, \tag{A13}$$

$$W_{ijkl} = \sum_{m} \frac{\left(\rho''_m - \dfrac{\rho'_m}{a^m}\right) a_i^m a_j^m a_k^m a_l^m}{(a^m)^2}, \tag{A14}$$

where $\phi''_m=[d^2\phi(r)/dr^2]_{r=a^m}$, and $\rho''_m=[d^2\rho(r)/dr^2]_{r=a^m}$.

For cubic crystals, the three independent elastic constants are, in Voigt notation, as follows:

$$\begin{aligned} C_{11} &= [B_{11} + F'(\rho_{eq})\, W_{11} + F''(\rho_{eq})\,(V_{11})^2\,]/\Omega_0, \\ C_{12} &= [B_{12} + F'(\rho_{eq})\, W_{12} + F''(\rho_{eq})\,(V_{12})^2\,]/\Omega_0, \\ C_{44} &= [B_{12} + F'(\rho_{eq})\, W_{12}\ ]/\Omega_0. \end{aligned} \tag{A15}$$

The vacancy-formation energy is given by:

$$E_v^f = -\frac{1}{2}\,\phi_{eq} + \sum_m \left[\, F_{eq}(\rho_{eq} - \rho_m) - F(\rho_{eq})\,\right] + E_{relax}\,, \tag{A16}$$

where E_{relax} takes account of the lattice relaxation around the vacancy.

From Eqs. (A9) and (A15), we can see the interplay between the pair potential and the embedding energy. If the pair potential is removed, then Eq. (A9) establishes $F'(\rho)=0$, and Eq. (A15) then gives $C_{11}=C_{12}$ and $C_{44}=0$, which is obviously violated in real solids. If the embedding energy is neglected and we rely entirely on the pair potential, then the equilibrium condition gives $A_{ij}=0$, so that $C_{12}=C_{44}$ (the Cauchy relation), which is not, in general, also valid for the real solids. It is seen from Eqs. (A15) that the Cauchy discrepancy (C_{12}-C_{44}) is determined by the curvature of $F(\rho)$ at equilibrium.

In the pair potential, it was noted that without the volume-dependent term, there was no Cauchy discrepancy in conflict with experiment. It was then suggested that a volume-dependent energy be added to account for the compressibility of the electron gas [Fuchs 1936]. The pair potential provides the attraction between atoms while the volume-dependent term serves to expand the solid slightly and give the correct elastic constants. Conversely, in what follows, the embedding energy, which depends on the electron density, is dominant and provides cohesion while the short-range repulsive pair interaction keeps the solid at a slightly larger lattice constant. In this way, the traditional volume-dependent energy is replaced by a density-dependent one, the advantage being that electron density is always definable.

BIBLIOGRAPHY

Abrahamson A.A., *Repulsive interaction potentials between rare-gas atoms. Heteronuclear two-center systems*, Phys. Rev., A133, 990 (1964).

Abrahamson A.A., *Born-Mayer-Type interatomic potential for neutral ground-state atoms with Z=2 to Z=105*, Phys. Rev., A178, 76 (1966).

Adams B.L., Wright S.I. and Kunze K., *Orientation imaging: the emergence of a new microscopy*, Metall. Trans., 24A, 819 (1993).

Allen M.P. and Tildesley D.J., Computer Simulation of Liquids, Clarendon Press, Oxford(1991).

Andersen H.C., *Molecular dynamics simulations at constant pressure and/or temperature*, J. Chem. Phys., 72, 2384 (1980).

Anderson M.P., Srolovitz D.J., Grest G.S. and Sahni P.S., *Computer simulation of grain growth I. kinetics*, Acta Metall., 32, 783 (1984).

Ashcroft N.W. and Mermin N.D., Solid State Physics, Holt, Rinehart and Winston, New York, (1976).

Aust K.T., *Future trends in grain boundary engineering*, in Karl T. Aust International Symposium on Grain Boundary Engineering, U. Erb and G. Palumbo, eds., Kingston, Ontario, 197 (1993).

Aust K.T. and Chalmers B., *Energies and structure of grain boundaries*, in Metal Interfaces, ASM, Cleveland, 153 (1952).

Aust K.T. and Palumbo G., *Interface control in metals*, in Structure and Property Relationship for Interfaces, J.L. Walter, A.H. King and K. Tangr, eds., ASM, 3 (1991).

Aust K.T. and Rutter J.W., *Temperature dependence of grain migration in high-purity lead containing small additions of tin*, Trans. Met. Soc. AIME, 215, 119 (1959).

Balluffi R.W., *Vacancy defect mobilities and binding energies obtained from annealing studies*, J. Nucl. Mater., 69&70, 240 (1978).

Balluffi R.W., Kwok J., Bristowe P.D., Brokman A., Ho P.S. and Yip S., *Determination of vacancy mechanism for grain boundary self-diffusion by computer simulation*, Scripta Metall., 15, 951(1981).

Barker J.A., *Interatomic potentials for inert gases from experimental data*, in Rare Gas Solids, M.L. Klein and J. A. Venables, eds., Academic Press, New York, 1, 212 (1976).

Baskes M.I., Foiles S.M. and Daw M.S., *Application of the embedded atom method to interfaces in metals*, Mater. Scri. Forum, 46, 187 (1989).

Beeler J.Q., Jr., *Atomistic model computer experiments*, in Computer Simulation in Materials Science, R.J. Arsenault, R. Beeler, Jr., and D.M. Esterling, eds., ASM International, Metal Park, Ohio, 45 (1988).

Briant C.L., Metallurgical Aspects of Environmental Failures, Elsevier, Amsterdam (1985).

Brosse J.B., Fillit R. and Biscondi M., *Intrinsic intergranular brittleness of molybdenum*, Scripta Metall., 15, 619 (1981).

Brown A.C. and Mountain R.D., *Velocity correlations in supercooled and nucleated liquid rubidium*, J. Chem. Phys., 80, 1263 (1984).

Brown D. and Clarke J.H.R., *A comparison of constant energy, constant temperature and constant pressure ensembles in molecular dynamics simulations of atomic liquids*, Mol. Phys., 51, 1243 (1984).

Carlsson A.E., *Unified description of "constant-volume" and "bond-breaking" pair potentials in metals*, Phys. Rev., B32, 4866 (1985).

Chan S.W., Liu J.S. and Balluffi R.W., *Test for a possible "melting" transition in grain boundaries in aluminum near the melting point*, Scr. Metall., 19, 1251 (1985).

Chen S.P., LeSar R. and Rollett A.D., *Modeling of transformation toughening in brittle composites*, Scripta Metall. Mater., 28, 1393 (1993).

Chen S.P., Voter A.F. and Srolovitz D.J., *Computer simulation of grain boundaries in* Ni_3Al*: the effect of grain boundary composition*, Scripta Metall., 20, 1389 (1986).

Chiba A., Hanada S., Watanabe S., Abe. T and Obana T., *Relation between ductility and grain boundary character distributions in* Ni_3Al, Acta Metall. Mater., 42, 1733 (1994).

Ciccotti G., Frenkel D. and McDonald I.R., Simulation of Liquid and Solids, North Holland, (1987).

Clementi E. and Roetti C., *Roothaan-Hartree-Fock atomic wavefunctions. basic functions and their coefficients for ground and certain excited states of neutral and ionized atom, Z≤54*, At. Data Nucl. Data Tables, 14, 177 (1974).

Dagens L., *Effective interatomic potentials in strong-scattering open shell metals: application to bonding force in d-band metals*, J. Phys. F16, 1705 (1986).

Dagens L., Rasolt M. and Taylor R., *Charge densities and interionic potentials in simple metals: nonlinear effects. II*, Phys. Rev., B11, 2726 (1975).

Daw M.S., *Model of metallic cohesion: the embedded-atom method*, Phys. Rev., B39, 7441 (1989).

Daw M.S. and Baskes M.I., *Semi-empirical quantum mechanical calculation of hydrogen embrittlement in metals*, Phys. Rev. Lett., 50, 1285 (1983).

Daw M.S. and Baskes M.I., *Embedded-atom method: derivation and application to impurities, surfaces, and other defects in metals*, Phys. Rev., B29, 6443 (1984).

Daw M.S., Baskes M.I. and Foiles S.M., dynamics code, public available via anonymous ftp 146.246.250.1 pub/EAM, (1985&1986).

Deymier P., Taiwo A. and Kalonji G., *A grain boundary phase transition studied by molecular dynamics*, Acta Metall., 35, 2719 (1987).

Don J. and Majumdar S., *Creep cavitation and grain boundary structure in type 304 stainless steel*, Acta Metall., 34, 961 (1986).

Englert A., Tompa H. and Bullough R., Fundamental Aspects of Dislocation Theory, U.S. National Bureau of Standards, Washington, DC, (1970).

Esterling D.M. and Swaroop A., *Interatomic potentials from experimental phonon spectra*, Phys. Stat. Sol., B96, 401 (1979).

Evans D.J., *Computer "experiment" for nonlinear thermodynamics of coutte flow*, J. Chem. Phys., 78, 3297 (1983).

Finnis M.W. and Sinclair J.E., *A simple empirical N-body potential for transition metals*, Phil. Mag., A50, 45 (1984).

Foiles S.M., *Application of the embedded-atom method to liquid transition metals*, Phys. Rev., B32, 3409 (1985).

Foiles S.M., Private communication, 1992.

Foiles S.M., Baskes M.I. and Daw M.S., *Embedded-atom-method functions for the fcc metals Cu, Ag, Au, Ni, Pd, Pt, and their alloys*, Phys. Rev., B33, 7983 (1986).

Foiles S.M. and Daw M.S., *Application of the embedded atom method to Ni$_3$Al*, J. Mater. Res., 2, 5 (1987).

Fuchs K., *A quantum mechanical calculation of the elastic constants of monovalent metals*, Proc. R. Soc. London, Ser., A153, 622 (1936).

Fuchs K., *The elastic constants and specific heats of the alkali metals*, Proc. R. Soc. London, Ser., A157, 444 (1936).

George E.P., Liu C.T. and Padgett R.A., *Comparison of grain boundary compositions in B-doped and B-free Ni$_3$Al*, Script Metall., 23, 979 (1989).

Grest G.S., Anderson M.P. and Srolovitz D.J., *Computer simulation of normal grain growth in three dimensions*, Phil. Mag., B59, 293 (1988).

Grimmer H., Bollmann W. and Warrington D.H., *Coincidence-site lattices and complete pattern-shift lattices in cubic crystals*, Acta Crystall., A30, 197 (1974)

Hanada S., Ogura T., Watanabe S., Izumi O. and Masumoto T., *Application of the selected area channelling pattern method to the study of intergranular fracture in Ni$_3$Al*, Acta Metall., 34, 13 (1986).

Hansen J.P. and McDonald I.R., Theory of Simple Liquids, Academic, New York, (1976).

Hansen M., Constitution of Binary Alloys, McGraw-Hill, New York, (1958).

Hargreaves F. and Hills R.J., *Work-softening and a theory of intercrystalline cohesion*, J. Inst. Met., 41, 257 (1929).

Harrison W.A., Pseudopotentials in the Theory of Metals, Benjamin, New York (1966).

Hasegawa M. and Watabe M., *Theory of compressibility of simple liquid metals*, J. Phys. Soc. Jpn., 32, 14 (1972).

Hasson G., Boos J.Y., Herbeuval I., Biscondi M., and Goux C., *Theoretical and experimental determinations of grain boundary structures and energies: correlation with various experimental results*, Surf. Sci., 31, 115 (1972).

Heine V. and Weaire D., *Pseudopotential theory of cohesion and structure*, in Solid State Physics, 24, Academic Press, New York, 249 (1970).

Henderson J.R. and Van Swol F., *On the interface between a fluid and a planar wall: theory and simulations of a hard sphere fluid at a hard wall*, Mol. Phys. 51, 991 (1984).

Hirano T., *Improvement of room temperature ductility of stoichiometric* Ni_3Al *by unidirectional solidification*, Acta Metall. Mater., 38, 2667 (1990).

Hirano T., *Tensile ductility of stoichiometric* Ni_3Al *grown by unidirectional solidification*, Scripta Metall. Mater., 25, 1747 (1991).

Hirano T. and Mawari T., *Cold rolling of boron-free polycrystalline* Ni_3Al *grown by unidirectional solidification*, Scripta Metall. Mater., 26, 597 (1992).

Hirano T. and Mawari T., *Unidirectional solidification of* Ni_3Al *by a floating zone method*, Acta Metall. Mater., 41, 1783 (1993).

Honeycutt J.D. and Andersen H.C., *Molecular dynamics study of melting and freezing of small Lennard-Jones clusters*, J. Phys. Chem., 91, 4950 (1987).

Hoover W.G., Ladd A.J.C. and Moran B., *High-strain-rate plastic flow studied via nonequilibrium molecular dynamics*, Phys. Rev. Lett., 48, 1818 (1982).

Hsieh T.E. and Balluffi R.W., *Experimental study of grain boundary melting in aluminum*, Acta Metall., 37, 1637 (1989)

Hsu C.S. and Rahman A., *Interaction potentials and their effect on crystal nucleation and symmetry*, J. Chem. Phys. 71, 4974 (1979).

Hultgren R., Desai P.D., Hawkins D.T., Glesier M. and Kelly K.K., Selected Values of the Thermodynamic Properties of Binary Alloys, American Society for Metals, Metals Park, OH, (1973).

Johnson R.A., *Relationship between two-body interatomic potentials in a lattice model and elastic constants*, Phys. Rev., B6, 2094 (1972).

Johnson R.A., *Interatomic potential development in materials science*, in Computer Simulation in Materials Science, R.J. Arsenault, R. Beeler, Jr., and D.M. Esterling, eds., ASM International, Metal Park, Ohio, 29 (1988).

Kargol J.A. and Albright D.L., *The effect of relative crystal orientation on the liquid metal induced grain boundary fracture of aluminum bicrystal*, Metall. Trans., 8A, 27 (1977).

Kayser F.X. and Stassis C., *The elastic constants of* Ni_3Al *at 0 and 23.5° C*, Phys. Stat. Sol., A61, 335 (1981).

Kobylanski A., J. Levy and Goux C., *Critical recrystallization cold-working of oriented single crystals of Nb, Mo and W deformed by compression*, C.R. Acad. Sci. C., (Paris), 273, 128 (1971).

Koch C.C., Liu C.T. and Stoloff N.S., High-Temperature Ordered Intermetallic Alloys, MRS Symp. Proc., Vol. 39 (1984).

Kronberg M.L., and Wilson F.H., *Secondary recrystallization in copper*, Trans. AIME, 185, 501 (1949).

Kurishita H., Kuba S., Kubo H. and Yoshinaga H., *Misorientation dependence of grain boundary fracture in molybdenum bicrystals with various <110> twist boundaries*, Trans. Jpn. Inst. Met., 26, 332 (1985).

Kurishita H., Oishi A., Kubo H. and Yoshinaga H., *Grain boundary fracture in molybdenum bicrystals with various <110> symmetric tilt boundaries*, Trans. Jpn. Inst. Met., 26, 341 (1985).

Kurishita H. and Yoshinaga H., *Grain boundary fracture in molybdenum*, Mater. Forum, 13, 161 (1989).

Lam N.Q. and Dagens L., *Calculations of the properties of simple and multiple defects in nickel*, J. Phys. F16, 1373 (1986).

Lee J.K., Interatomic Potentials and Crystalline Defects, The Metallurgical Society of AIME, Warrendale, PA (1981).

Lennard-Jones J.E., *On the determination of molecular field. II. from the equation of state of a gas*, Proc. of the Royal Society, A106, 463 (1924).

Leung C.H., Stott M.J. and Young W.H., *Thermodynamics properties of solid alloys: application to* Mg_xCd_{1-x}, J. Phys. F6, 1039 (1976).

Li D.H., Li X.R. and Wang S., *Variational calculation of Helmboltz free energies with applications to the sp-type liquid metals*, J. Phys., F16, 309 (1986).

Lim L.C. and Raj R., *Effect of boundary structure on slip-induced cavitation in polycrystalline nickel*, Acta Metall., 32, 1183 (1984)

Lim L.C. and Watanabe T., *Grain boundary character distribution controlled toughness of polycrystals - a two-dimensional model*, Scripta Metall., 23, 489 (1989).

Lim L.C. and Watanabe T., *Fracture toughness and brittle-ductile transition controlled by grain boundary character distribution (GBCD) in polycrystals*, Acta Metall. Mater., 38, 2507 (1990).

Lin H. and Pope D.P., *The influence of grain boundary geometry on intergranular crack propagation in Ni_3Al*, Acta Metall. Mater., 41, 553 (1993).

Liu C.T., White C.L. and Horton J.A., *Effect of boron on grain boundaries in Ni_3Al*, Acta Metall., 33, 213 (1985).

Lu J. and Szpunar J.A., *Glass formation and crystallization of liquid and glass rubidium: a constant pressure molecular dynamics study*, J. Chem. Phys., 91, 1313 (1992).

Lu J. and Szpunar J.A., *Molecular-dynamics simulation of rapid solidification of aluminum*, Acta Metall., 41, 2291 (1993).

Lu J. and Szpunar J.A., *Applications of the embedded-atom method to glass formation and crystallization of liquid and glass transition metal Ni*, submitted to Phil. Mag. A., (1995).

Lu J. and Szpunar J.A., *Molecular dynamics simulation on crystallization of amorphous Al*, Scripta Metall. Mater., 32, 1957 (1995).

Lu J. and Szpunar J.A., *Molecular-dynamics simulation of the melting of a twist $\Sigma 5$ grain boundary*, Interface Science, 3, 143 (1995).

Lu J. and Szpunar J.A., *Atomistic modeling of grain boundary fracture*, in preparation, (1995).

Lu J. and Szpunar J.A., *Microstructural model of intergranular fracture in textured materials*, submitted to Scripta Metall. Mater., (1995).

Lutsko J.F., Wolf D., Phillpot S.R. and Yip S., *Molecular-dynamics study of lattice-defect-nucleated melting in metals using an embedded-atom-method potential*, Phys. Rev., B40, 2841 (1989).

Lutsko J.F., Wolf D., Yip S., Phillpot S.R. and Ngugen T., *Molecular-dynamics method for the simulation of bulk-solid interfaces at high temperatures*, Phys. Rev., B38, 11,572 (1988).

Lynch S.P., *Mechanisms of intergranular fracture*, Mater. Sci. Forum, 46, 1 (1989).

Mandell M.J., McTagne J.P. and Rahman A., *Crystal nucleation in a three-dimensional Lennard-Jones system. II. nucleation kinetics for 256 and 500 particles*, J. Chem. Phys., 66, 3070 (1977).

Mariarty J.A., *First-principles interatomic potentials in transition metals*, Phys. Rev. Lett., 55, 1502 (1985).

McLean A.D. and McLean R.S., *Roothaan-Hartree-Fock atomic wavefunctions, slater basis-set expansions for Z = 55 - 92*, At. Data Nucl. Data Tables, 26, 197 (1981).

Mountain R.D. and Basu P.K., *Molecular dynamics study of homogeneous nucleation for liquid rubidium*, J. Chem. Phys., 78, 7318 (1983).

Nguyen T., Ho P.S., Kwok T., Nitta C. and Yip S., *Grain-boundary melting transition in an atomistic simulation model*, Phys. Rev. Lett., 57, 1919 (1986).

Nosé S. and Yonezawa F., *Isothermal-isobaric computer simulations of melting and crystallization of a Lennard-Jones system*, J. Chem. Phys., 84, 1803 (1986).

Otsuki A. and Mizuno M., *Grain boundary energy and liquid metal embrittlement of aluminium*, Trans. Japan Inst. Metals Suppl., 27, 789 (1986).

Palumbo G. and Aust K.T., *Special properties of Σ grain boundaries*, in Materials Interfaces, S.Yip and D. Wolf, eds., Chapman and Hall, London, 190 (1992).

Palumbo G., King P.J., Aust K.T., Erb U. and Lichtenberger P.C., *Grain boundary design and control for intergranular stress-corrosion resistance*, Scripta Metall. Mater., 25, 1775 (1991).

Parrinello M. and Rahman A., *Polymorphic transitions in single crystals: a new molecular dynamics*, J. Appl. Phys., 52, 7182 (1981).

Pontikis V., *Grain boundary structure and phase transformations: a critical review of computer simulation studies and comparison with experiments*, J. Physique Colloque, 49, C5-327 (1988).

Puge S.F., An Introduction to Grain Boundary Fracture in Metals, The Institute of Metals, 1991.

Qi D.W., Lu J. and Wang S., *Crystallization properties of a supercooled metallic liquid*, J. Chem. Phys., 96 513 (1992).

Ray J.R. and Rahman A., *Statistical ensembles and molecular dynamics studies of anisotropic solids*, J. Chem. Phys., 80, 4423 (1984).

Rimmer D.E. and Cottrell A.H., *The solution of inert gas atoms in metals*, Phil. Mag., 2, 1345 (1957).

Ronchetti M. and Jacucci G., Simulation Approach to Solids, Kluwer Academic Publishers, London, (1991).

Rose J.H., Smith J.R., Guinea F. and Ferrante J., *Universal features of the equation of state of metals*, Phys. Rev., B29, 2963 (1984).

Sato K., Miyazaki H., Ikuhara Y., Kurishita H. and Yoshinaga H., *Structure and strength of grain boundaries in Si bicrystals with <111> twist misorientations*, J. Japan Inst. Metals, 53, 536 (1989).

Schvindlerman L.S. and Straumal B. B., *Regions of existence of special and non-special grain boundaries*, Acta Metall., 33, 1735 (1985).

Seah M.P., *Impurities, segregation and creep embrittlement*, Philos. Trans. R. Soc. A295, 265 (1980).

Simmons G. and Wang H., Single Crystal Elastic Constants and Calculated Aggregate Properties: A Handbook, MIT Press, Cambridge, (1971).

Simth C.J., Metal Reference Book, 5th ed., Butterworths, London, p.186, (1976).

Srolovitz D.J., Anderson M.P., Sahni P.S. and Grest G.S., *Computer simulation of grain growth II. grain size distribution, topology, and local dynamics*, Acta Metall., 32, 793 (1984).

Srolovitz D.J., Anderson M.P., Grest G.S. and Sahni P.S., *Grain growth in two dimensions*, Scripta Metall., 17, 241 (1983).

Srolovitz D.J., Yang W.H., Najafabadi R., Wang H.Y. and LeSar R., *Microstructural and segregation effects in the fracture of polycrystals*, in Materials Interfaces, S.Yip and D. Wolf, eds., Chapman and Hall, London, 691 (1992).

Stillinger F.H. and LaViolette R.A., *Local order in quenched state of simple atomic substances*, Phys. Rev., B34, 5136 (1986).

Stillinger F.H. and Weber T.A., *Hidden structure in liquids*, Phys. Rev., A25, 978 (1982).

Stoloff N.S., *Physical and mechanical metallurgy of Ni_3Al and its alloys*, Intern. Materials Reviews, 34, 153 (1989).

Stoloff N.S., Koch C.C., Liu C.T. and Izumi O., High-Temperature Ordered Intermetallic Alloys, MRS Symp. Proc., Vol. 39 (1984).

Swope W.C. and Andersen H.C., *10^6-particle molecular-dynamics study of homogeneous nucleation of crystals in a supercooled atomic liquid*, Phys. Rev., B41, 7042 (1990).

Szpunar J.A. and Hinz D., *Modelling of recrystallization textures*, in Karl T. Aust International Symposium on Grain Boundary Engineering, U. Erb and G. Palumbo, eds., Kingston, Ontario, 133 (1993).

Takeyama M. and Liu C.T., *Effects of grain size and test temperature on ductility and fracture behavior of a B-doped Ni_3Al alloy*, Acta Metall., 36, 1241 (1988).

Tyson W.R. and Miller W.A., *Surface free energies of solid metals: estimation from liquid surface tension measurements*, Surf. Sci., 62, 267 (1977).

Van Swol F. and Henderson J.R., *Wetting at a fluid-wall interface*, J. Chem. Soc., 82, 1685 (1984).

Wang S. and Lai S.K., *Structure and electrical resistivities of liquid binary alloys*, J. Phys., F10, 2717 (1980).

Wang T.-M., Shimotomai M. and Doyama M., *Study of vacancies in the intermetallic compound Ni_3Al by positron annihilation*, J. Phys., F14, 37 (1984).

Warrington D.H., Grain Boundary Structure and Kinetics, R.W. Balluffi ed., ASM, Metals Park, OH., p.1, (1979).

Waseda Y., The Structure of Non-crystalline Materials, McGraw-Hill, New York, (1980).

Watanabe M.S. and Tsumuraya K., *Crystallization and glass formation processes in liquid sodium: a molecular dynamics study*, J. Chem. Phys., 87, 4891 (1987).

Watanabe T., *Grain boundary sliding and stress concentration during creep*, Metall. Trans., 14A, 531 (1983).

Watanabe T., *An approach to grain boundary design for strong and ductile polycrystals*, Res Mechanica, 11, 47 (1984).

Watanabe T., *Structural effects on grain boundary segregation, hardening and fracture*, J. Physique, 46, C4-555 (1985).

Watanabe T., *Grain boundary design for new materials*, Trans. Japan Inst. Met., 27, 73(1986).

Watanabe T., *The potential for grain boundary design in materials development*, Mater. Forum, 11, 284 (1988).

Watanabe T., *Grain boundary design for the control of intergranular fracture*, Mater. Sci. Forum, 46, 25 (1989).

Watanabe T., *Toughening of brittle materials by grain boundary design and control*, Mater. Sci. Forum, 126-128, 295 (1993).

Watanabe T., *Toward grain boundary design and control for advanced materials*, in Karl T. Aust International Symposium on Grain Boundary Engineering , U. Erb and G. Palumbo, eds., Kingston, Ontario, 57 (1993).

Watanabe T., Kitamura S. and Kaarashima S., *Grain boundary hardening and segregation in alpha iron-tin alloy*, Acta Metall., 28, 455 (1980).

Watanabe T., Shima S. and Karashima S., Embrittlement by Liquid and Solids Metals, Mater. Soc. A.I.M.E., 161 (1984).

Wolf D., *Grain-Boundary Modelling*, in Computer Simulation in Materials Science, R.J. Arsenault, R. Beeler, Jr., and D.M. Esterling, eds., ASM International, Metal Park, Ohio, 111 (1988).

Wolf D., *Correlation between energy, surface tension and structure of free surfaces in fcc metals*, Surface Science, 226, 389 (1990).

Wolf D., *Atomic-level geometry of crystalline interfaces*, in Materials Interfaces, S.Yip and D. Wolf, eds., Chapman and Hall, London, 190 (1992).

Wolf D. and Merkle K.L., *Correlation between the structure and energy of grain boundaries in metals*, in Materials Interfaces, S.Yip and D. Wolf, eds., Chapman and Hall, London, 190 (1992).

Wood G.J., Stobbs W.M. and Smith D.J., *Methods for the measurement of rigid-body displacements at edge-on boundaries using high resolution electron microscopy*, Phil. Mag., A50, 375 (1986).

Wycisk W. and Feller-Kniepmeier M., *Quenching experiments in high purity Ni*, J. Nucl. Mater., 69&70, 616 (1978).

Yip S. and Wolf D., *Atomistic concepts for simulation of grain boundary fracture*, Mater. Sci. Forum, 46, 77 (1989).

Zhou Y., Neale K.W. and Tóth L.S., *Analytical solutions for the ideal orientations of F.C.C. rolling textures*, Acta Metall. Mater., 39, 2921 (1991).

Zhou Y., Tóth L.S. and Neale K.W., *On the stability of the ideal orientations of rolling textures for F.C.C. polycrystals*, Acta Metall. Mater., 40, 3179 (1992).

Zhou Y., Savoie J. and Jonas J.J., *Influence of initial texture on the development of deep drawing textures in fcc metals*, Mater. Sci. Forum, 157-162, 879 (1994).